CONTENTS

DE GRUYTER
OPEN

DOI 10.1515/ama-2017-0025

TEST METHOD FOR RHEOLOGICAL BEHAVIOR OF MORTAR FOR BUILDING WORK

Bogdan KOROBKO[*], **Ievgen VASYLIEV**[*]

[*]Electromechanic Faculty, Department of Construction Machinery and Equipment, Poltava National Technical Yuri Kondratyuk University,
Poltava, Pershotravnevyi Avenue 24, Ukraine

bogdan.korobko@ukr.net, vas.eugene@gmail.com

received 25 August 2016, revised 18 July 2017, accepted 7 August 2017

Abstract: This paper offers a test method for rheological behavior of mortars with different mobility and different composition, which are used for execution of construction work. This method is based on investigation of the interaction between the valve ball and the mortar under study and allows quick defining of experimental variables for any composition of building mortars. Certain rheological behavior will permit to calculate the design parameters of machines for specific conditions of work performance – mixing (pre-operation), pressure generation, pumping to the work site, workpiece surfacing.

Key words: Mortar Mixture, Rheology, Mobility Of Mortar, Pumping Over, Mixing

1. INTRODUCTION

Adoption of innovative mechanised technologies of finishing works execution broadens application of hauling equipment for mortar mixtures and tender mixes pipelining. For this purpose, the usage of highly productive short-duration pulse mortar pumps provides an opportunity to mechanize not only the supply of constructional materials to working places, but also to execute the main processing steps: mechanized plastering and decorative coating in the process of finishing the walls; laying mortar mixtures when sealing structural joints; mixture placing on the floor, damp-proofing.

Best practices in operating mortar pumps when phasing in mechanized technology points to further improvement of these machinery through their reliability growth and by reducing energy costs for repumping at the cost of flow fluctuation decrease and volumetric losses in the fluid end of the mortar pump (Korobko and Vasyliev, 2012).

User experience of mortar pumps lends credence to the fact, that the level of mortar mixtures' volumetric losses during repumping is pretty much conditioned upon the interaction between the operating environment and mortar pump's working members, that are defined by their elastic characteristics. However, the deficiency of quantitative characteristics of elastic characteristics of mortar mixtures with different composition and mobility adds complexity to the development of effective ways of improving volume efficiency of the created new-generation mortar pumps. That's why theoretical studies and field researches of mortar mixtures' elastic characteristics are sorely needed for the improvement of the ways of mortar mixtures' pipelining.

The major complications in the process of repumping mortar mixtures are caused by their rheological characteristics. The mortar mixture is structured thixotropic liquid, the main rheological characteristics of which are structured viscosity and critical shear stress. When lowering the mobility of the mortar to the technologically required magnitude (10…8 cm), these figures assume the values, where the advance of mortar mixture flow over the pipeline evokes rather strong resistance. Under such conditions the process of filling the processing chamber with mortar mixture is made difficult under the influence of pressure decrease from the level 0.1 MPa. Service conditions of valve operation also decline, what causes the delay of the valve closure and sometimes on-state "hanging" and dramatic reduction of pump volumetric efficiency (Korobko, 2016).

With allowance for this, taking into account the abovesaid peculiarities when developing and estimating service properties of hauling equipment is an important task.

Construction mix as a service which is piped through pipelines, has a set of features that must be taken into account in the design of mortar pumps, as well in their operation.

Mobility of construction mixtures can be increased by adding fluidifiers into them. Highly mobile mixtures with the mobility of 11-12 cm are used for spraying the first coat when plastering surfaces in order to increase the cohesive resistance of the plastering coat with the brick masonry. Mixtures with mobility of 8-9 cm are transferred through pipelines with difficulty; they are hardly sucked into the sucking working chamber of the mortar pump; valve balls may "hover" in them, what may cause failure in the operation of mortar pumps. However, these mixtures allow to lay on maximum-deep plaster layers during the minimum amount of passes; furthermore, they bring less moisture into building constructions.

The main processing characteristics of plasters:

- easy laying on, which is characterized by the mobility of construction mixture, in other words – by the ability to flow under the influence of its own weight or external forces;
- water fixation - the property to retain excess water in the process of suction, thereby there are no water losses when laying mortar mixture on the porous soil, as well as it unscrambles insignificantly during the transportation of mortars;
- compressive breaking strength of the mortar stone;

- freeze-thaw durability, which is determined by the ability of mortar mixture sample to withstand in a water-saturated state of a certain number of cycles of alternate freezing and thawing.

The slurry formulation comprises a significant number (up to 70% of volume) of dispersed hard phase. But such state of solution is not stable. If the size or the direction of speed changes due to the hard phase immiscibility or aggregation, there arise deposits of solid particles, which increase the resistance to flow advance and seal paravalvular blowholes. In addition, if the pump stops for extended lengths of time, except immiscibility, partial hardening of the pumped medium takes place, especially on hydraulic binding agents. Consequently, routine breaks in the work of pump require timeous flushing of cavities in the processing chamber and pipelines.

Density composition of solids drastically worsens operation conditions of friction couples in the fluid end of the mortar pump – seals, muff, piston and rod. Another disadvantage, that accelerates rubbing parts' wear, is the presence in the solution of water, which in combination with chemically-active cementing phases causes corrosive action, in other words, it conditions erosion corrosion and particulate erosion of the mortar pump's parts.

Against this background, an important task is to take into account the mentioned peculiarities in estimating and developing the service properties of hauling equipment.

When analyzing the influence of solution properties on the pumping process, it is necessary to use their flow factor, which is in the range of 5 ... 12 cm and characterizes the convenience of transportation and mortar laying on workpiece surfaces. However, this characteristic does not reveal the interaction between the solution and pump components and can describe this process only when building empirical statistic dependences.

In this regard, when developing new samples of mortar pumps, it seems essential and important today to analyze the method of scoring the properties of solutions in order to reveal the mechanism of manifestation of these properties in the process of conveyance by the mortar pump.

Rheological properties of solutions are determined by using the viscometres of rotatory operation. The principle of operation of these devices is based on the studying of relative rotational motion of cylinders, between which the test medium is situated. The usage of this method for building mortars is limited by the slot width between the cylinders and is efficient only for very workable plasters. The value of structured viscosity and shift voltage depend mainly on the flow rate (the intensity of structural links destruction). In different sources the represented data on the significance of the pointed out rheological properties have quite a broad band, as they were received in different velocity (kinematic) conditions. In this regard, when developing a machine with specific operating factors, it is necessary to do measuring operations on the used solution in order to correct real value of thresholds, which characterize rheological properties of the service (medium).

The required properties of the mortar are achieved by cement-aggregate compatibility, namely by the amount of material by weight or volume, which falls per 1 m3 of mortar mixture, or by the ratio of each mortar's component to the binder also by mass or volume, at that the binder discharge is taken as a unit (Chen et al., 2013; Kheradmand M. et al., 2014).

It should be noted that during pipeline transportation it is necessary to provide plasticity of mortar mixture and appropriate convenience of pumping under pressure. The latter is peculiar to such mixtures, that during transportation by the mortar pump do not form stagnation zones or sand seals in pressure hoses, and are pumped as a continuous flow. These showings are determined by the mobility of the mixture and they are provided by adjusting to the required condition in the mixer of the plastering machine (Kim K.H. et al., 2012).

Further improvement of the facilities for mortar mixture supply through pipelines and the development of rational parameters of the structural components in the fluid end of the mortar pump with minimal resistance to pumping under pressure require studying the interaction of the working body and the valve assemblies with the flow of the pumped medium. In order to get that done, again, it is necessary to define rheological characteristics of the pumped mortar mixture.

2. MEASURING TECHNIQUE FOR RHEOLOGICAL PROPERTIES OF MORTAR MIXTURES

Flow behavior of mortar mixtures, which belong to structural fluids (Almeida and Sichieri, 2007; Binici et al., 2012; González-Fonteboa and Martínez-Abella, 2008), can be characterized to the fullest extent possible by the formula of Shvedov-Bingham

$$\tau = \tau_0 + \eta \cdot \frac{dV}{dn}, \tag{1}$$

where: τ – is the shear stress, Pa; τ_0- is the critical shear stress, after the achievement of which the liquid comes into motion, Pa; η – is the absolute viscosity coefficient Pa·s; $\frac{\mathrm{dV}}{\mathrm{dn}}$ – is the velocity gradient in the cross flow direction.

The critical shear stress τ_0 and the absolute viscosity coefficient η are the main rheological properties of the service under consideration and determine the nature of the interaction between mortar mixture flow with the elements of the fluid end of the mortar pump.

The value of the indicated parameters varies over the residence time of the static fluid (at zero speed) and depends on a number of factors (Cuia et al., 2015). This is, in particular, the ratio of the mortar mixture ingredients, the quantity of water, which is comprised into the mortar mixture, the flow rate of speed. In addition, rheological characteristics depend on specific measurement conditions (Perrot et al., 2013).

This explains the wide disagreement in the values of the mentioned parameters τ_0 and η, given in different literature sources (Assaad and Daou, 2014; Reis et al., 2011). Therefore, in the process of pumping the mortar mixture, it is necessary to define the indicated parameters for mortar mixtures with fixed composition and specified mobility.

In view of this, the usage of traditional viscosity measurement devices is obstructed, as far as in order to carry out measurements within the broad range of flow and different slurry formulation every time it is necessary to readjust the equipment with the objective of ensuring proper measuring conditions.

In addition, these devices perform the viscosity measurement at a certain speed of medium motion, so the obtained results can be considered adequate only under certain conditions.

Volarovich viscosimeter is the most appropriate for the evaluation of rheological parameters of sand-lime mortars with different mobility (Kockal, 2016). But it has a rather complex structure and requires high accuracy of manufacturing and assembling of its components.

Having regard to the above, we have proposed a test method for determining the rheological properties of mortar mixtures with different mobility, which is the study of the interaction between a metal ball and the test solution.

An example of a study of the interation between a spherical body and the liquid is the Stokes problem of a slow static flowing round the ball, in which the main influence is created by pressure and friction forces, and inertial components are not taken into account. A real example, closest to such a movement, is a slow drop of the ball in very viscous liquid (Korobko B and Vasyliev, 2014), to which sand-lime mortar can also be relevant.

The solving of the Stokes problem, when the ball is flowed round by structural liquid, the rheological behavior of which is determined by Shvedov-Bingham's law (1), takes the following form:

– the normal stress pattern on the ball surface of radius r at static relative motion of a ball and of the liquid at the velocity of $\mathrm{V_0}$ is as follows

$$p = -\frac{3}{2} \cdot \frac{V_0 \cdot \eta}{r} \cdot cos\varphi, \tag{2}$$

where: φ – is the central angle between the direction of the velocity vector $\vec{V}_0$ of flow and the normal to the concerned element of the spherical surface of the ball;

– shear stresses, caused only by viscosity and velocity gradients in the boundary layer, are spread on the surface of the ball in this way:

$$\tau_\eta = \frac{3}{2} \cdot \frac{V_0 \cdot \eta}{r} \cdot sin\varphi, \tag{3}$$

and with a glance to the critical shear stress of the environment τ_0 (1)

$$\tau_\eta = \tau_0 + \frac{3}{2} \cdot \frac{V_0 \cdot \eta}{r} \cdot sin\varphi. \tag{4}$$

The forcing, which is a measure of the interaction between a ball and structural liquid, consists of two components

$$F = F' + F''. \tag{5}$$

The components of the force F are defined as the sum of projections of elementary efforts, caused by the availability of normal p and shear τ stresses on the surface of the ball (Fig. 1):

$$F' = \int_S \tau{\cdot}cos[90° - (180° - \varphi)]dS,$$

$$F'' = \int_S p \cdot \cos(180° - \varphi)\, dS.$$

Formula (5) after the conversion of expressions for F' and F'' will be of the following form

$$F = \int_S \tau{\cdot}sin\varphi dS - \int_S p{\cdot}cos\varphi dS, \tag{6}$$

where: dS – is the area of the ball's surface element,
$dS = 2{\cdot}\pi{\cdot}r^2{\cdot}sin\varphi d\varphi$.

Having inserted the relations (2) and (4) into (6), we will get the formula for determining the resistance force F, which occurs when a ball of radius r moves with respect to the mortar mix at a speed of V_0:

$$F = \int_0^\pi \left(\tau_0 + \frac{3}{2} \cdot \frac{V_0 \cdot \eta}{r} {\cdot} sin\varphi\right) {\cdot} sin\varphi {\cdot} 2 {\cdot} \pi {\cdot} r^2 {\cdot} sin\varphi d\varphi -$$
$$- \int_0^\pi \left(-\frac{3}{2} \cdot \frac{V_0 \cdot \eta}{r} {\cdot} cos\varphi\right) {\cdot} cos\varphi {\cdot} 2 {\cdot} \pi {\cdot} r^2 {\cdot} sin\varphi d\varphi,$$
$$F = \pi^2 {\cdot} r^2 {\cdot} \tau_0 + 6 {\cdot} \pi {\cdot} V_0 {\cdot} r {\cdot} \eta. \tag{7}$$

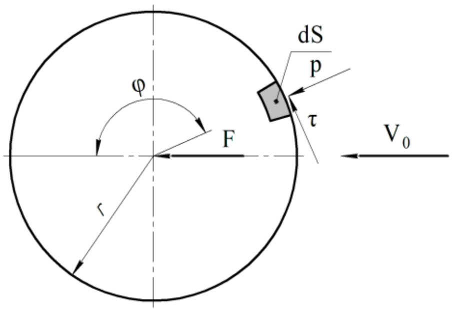

Fig. 1. The scheme of interaction between the ball and the flow of mortar mix

The first summand of the expression (7) is independent of the structural solution viscosity η and the speed of ball's movement. It defines the component of the total force, which is necessary for shifting the ball towards the mortar mix, which creates static resistance to its motion, caused by the presence of τ_0 stress. The second summand is determined by the traverse speed of the ball $\mathrm{V_0}$ relative to the mortar mix.

Analyzing the expression (7), we can come to the conclusion, that the determination of rheological parameters τ_0 and η of the mortar mix should be carried out in two stages.

At first it is necessary to define the force, at which there occurs the shift of the ball of radius r, which is in the mortar mix. This allows you to calculate the value of τ_0, provided that at the beginning of the shift of the ball its speed through mortar mix becomes zero. Then the expression (7) will be as follows $\mathrm{F_\tau = \pi^2{\cdot}r^2{\cdot}\tau_0}$, from which

$$\tau_0 = \frac{F_\tau}{\pi^2 {\cdot} r^2}. \tag{8}$$

The value $\mathrm{F_\tau}$ is defined as the difference between the external force $\mathrm{F_0}$, at which the ball shear occurs, and the buoyancy force $\mathrm{F_A}$.

Then there are measured the speed $\mathrm{V_0}$ and the nature of ball's motion in the mortar mix under the action of constant external force F. After determination of the velocity $\mathrm{V_0}$ and the stress τ_0 on the basis of the expression (7) there is calculated the value of the plastic solution viscosity η

$$\eta = \frac{F - \pi^2 {\cdot} r^2 {\cdot} \tau_0}{6 {\cdot} \pi {\cdot} V_0 {\cdot} r}. \tag{9}$$

With allowance for the buoyancy force, the calculating formulae (8) and (9) ultimately will be of the following form:

$$\tau_0 = \frac{F_0 - \frac{4}{3} {\cdot} \pi {\cdot} r^3 {\cdot} g {\cdot} \rho}{\pi^2 {\cdot} r^2}, \tag{10}$$

$$\eta = \frac{\mathrm{F} - \frac{4}{3} {\cdot} \pi {\cdot} r^3 {\cdot} g {\cdot} \rho - \pi^2 {\cdot} r^2 {\cdot} \tau_0}{6 {\cdot} \pi {\cdot} V_0 {\cdot} r}, \tag{11}$$

where: ρ – is the density of the test solution, kg/m3, g – is the gravitational acceleration, m/s2.

In order to study the interaction between the ball and the test solution, we have used the apparatus (see Fig. 2), which consists of a steel ball 1, rigidly connected with the steel rod 2. At the rod there was located bearing plate 3 for the load of balance weights. At determining the initial shift of the ball, on the end of the rod there is placed a pointer against the corresponding scale mark, situated on the bracket 4, which is connected to the blending hopper. When investigating the ball's motion pattern in the mortar mix on the bracket 4, there is set a displacement pickup of inductive type 5.

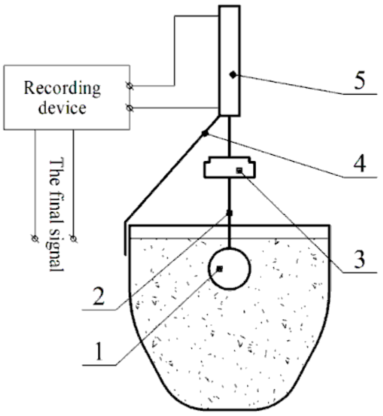

Fig. 2. The device for measuring rheological characteristics of the mortar mix

Measurements are performed in such a way. The ball 1 is submerged into the freshly-mixed sand-lime mortar with the proportion of ingredients 1: 3 in such a way, so that it would be completely covered with the mortar. Balance weights are consistently set on the bearing plate 3 in such a way, so that the difference in load between them would be no more than 5 g. Keeping watch over the pointer, we fix the shear couple of the ball. The magnitude of applied force F_0, which corresponds to the beginning of shift, is defined as the sum of fare weight of a ball with a rod and the weight of balance weights, established on the bottom. The density of the mortar mix is determined by weighing the fixed volume of the mortar. Then the critical shear stress τ_0 for the test solution is determined from the formula (10). The mobility of the mortar mix is measured by using the slump cone "StroyTsNIL". When measuring the ball's rate of descent in the test solution, the load weighing 2.5 ... 3 times larger than F_0 is set on the bearing plate (this is necessary to ensure the sinking of the ball in the mortar mix). The mortar mix is stirred in the slurry blender. Immediately after the shut-down of the stirring the ball 1 is sunk in such a way, so that it would be completely covered by the mortar mix, and it is held in this position. The self-recording instrument is switched on and the ball is released.

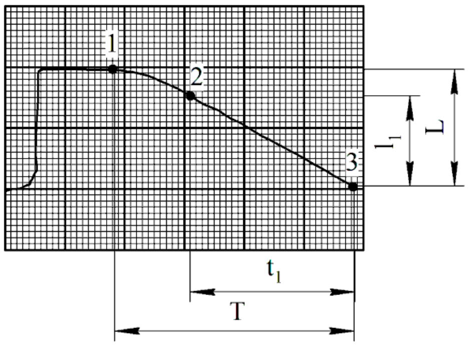

Fig. 3. The displacement diagram, showing the movement of the ball 60 mm in diameter in the sand-lime mortar with the composition 1:3 and with the medium workability of 8 cm

In Fig. 3 there is given a displacement diagram, showing the movement of the ball 60 mm in diameter in the sand-lime mortar with the composition 1: 3 and with the medium workability of 8 cm.

The chart shows that at a certain period of time the ball is moving at a constant speed (points 2-3), that is, the interaction process is stationary in nature. One cell of the diagram in the horizontal direction corresponds to 0.01 s. The analysis of the diagram testifies that the full time of the ball's release T is equal to 0.39 (segment T = 39 mm), and the ball's stationary motion t_1 = 0.27 s (segment t_1= 27 mm). The ball's depth of immersion is determined based on the results of the movement sensor calibration (in the diagram L = 323 mm, l_1, = 255 mm).

The study of the received diagram allows to determine the velocity of the ball in the mortar mix at the steady motion area according to the formula $\mathrm{V}_0=\frac{\mathrm{l}_1}{\mathrm{t}_1}$ and, using the relationship (11), to calculate the value of the plastic viscosity of the test solution η.

The criterion which determines the process of hydrodynamic interaction between a valve ball and the flow of mortar is Reynolds criterion, which characterizes the effect of medium viscosity forces while flowing round the ball. In estimating flow motion of viscous medium in cylindrical space Reynolds criterion is as follows:

$$Re=\frac{V_0\cdot 2\cdot r}{\eta}\cdot\rho. \tag{12}$$

When investigating the medium motion, which has got structured viscosity, the generalized parameter of Reynolds ought to be determined in the following way:

$$Re^*=Re\frac{6\cdot\eta\cdot V_0}{6\cdot\eta\cdot V_0+\tau_0\cdot 2\cdot r}. \tag{13}$$

Using the above mentioned methods, we have carried out measurements by applying the sand-lime mortar with the composition 1:3 and with the medium mobility ranging from 8 to 12 cm. The results of measurement are using a 40, 50 and 60 mm diameter steel ball are given in the Tab. 1.

Tab 1. The measuring results of rheological characteristics of sand-lime mortar mixes with different mobility

Mobility, [cm]	Density ρ, [kg/m^3]	d, [mm]	F_0, [N]	τ_0, [Pa]	F, [N]	V_0, [m/s]	η, [Pa·s]	Re^*
8	2100	60	7.75	610.22	24.07	0.94	30.53	3.21
		50	5.10	608.43	15.30	0.74	29.20	2.14
		40	3.14	607.92	8.40	0.45	31.22	0.93
10	2000	60	6.42	473.60	17.85	1.21	16.71	7.03
		50	4.21	475.70	11.75	1.06	15.07	5.65
		40	2.55	479.56	8.40	0.93	16.69	3.72
12	1900	60	4.80	303.86	11.43	0.98	12.00	7.40
		50	3.09	303.21	7.86	0.89	11.41	5.93
		40	1.81	301.51	5.25	0.81	11.27	4.47

For checking the proper use of analytic consistent patterns, the authors have sized up the actual magnitude of Reynolds parameter, which is the criterion of the process' temporal homogeneity. The calculation data of Re^* according to the formula (13) for every dimension are listed in the table 1. This parameter value in all dimensions does not exceed $Re^*=10$, what offers an opportunity to draw a conclusion about the accuracy of the developed methodology.

3. CONCLUSIONS

The analysis of the obtained measured data and calculation data points out that in case of reduction in diameter of the ball, its zero-time shift in the mortar of certain mobility requires less efforts. When increasing the mobility of the mortar, the effort of zero-time shift of the ball of certain diameter decreases either.

Calculation data for each ball testify that the values of boundary traction of the shift and the coefficient of structured viscosity of the mortar of certain mobility are in narrow interval, that does not exceed systematic inaccuracy of measurements. That is why for the mortar of target slump these dimensional characteristics can be determined as arithmetical average of measured data for each ball. Moreover, in case of increase of mobility of the analyzed mortar, the values of boundary traction of the shift and the coefficient of structured viscosity decrease substantially. It makes it possible to confirm that rheological properties of building mortars depend only on their consistence.

The proposed method makes it possible to quickly determine the rheological properties of mortar mixes and other structural liquids, which follow Shvedov-Bingham's law, immediately prior to their conveyance by the mortar pump.

It will allow to predict energy costs during the work of equipment set for plastering: expenditures for mixing in the mixer tap, injection of grout by the mortar pump and transportation of mortars by pipeline. The design extent of power consumption will help to determine the necessary propulsive output as part of equipment set.

REFERENCES

1. **Almeida Alessandra E. F. de S., Sichieri Eduvaldo P.** (2007), Experimental study on polymer-modified mortars with silica fume applied to fix porcelain tile, *Building and Environment,* 42(7), 2645–2650.
2. **Assaad Joseph J., Daou Yehia.** (2014), Cementitious grouts with adapted rheological properties for injection by vacuum techniques, *Cement and Concrete Research*, 59, 43–54.
3. **Binici Hanifi, Gemci Remzi, Kaplan Hasan.** (2012), Physical and mechanical properties of mortars without cement, *Construction and Building Materials*, 28(1), 357–361.
4. **Chen X., Wu S., Zhou J., Chen Y., Qin A.** (2013), Effect of testing method and strain rate on stress-strain behavior of concrete, *Journal of Materials in Civil Engineering*, 25(11), 1752–1761.
5. **Cuia Hongzhi, Liaoa Wenyu, Mia Xuming, Lob Tommy Y., Chenc Dazhu.** (2015), Study on functional and mechanical properties of cement mortar with graphite-modified microencapsulated phase-change materials, *Energy and Buildings,* 105, 273–284.
6. **González-Fonteboa B., Martínez-Abella F.** (2008), Concretes with aggregates from demolition waste and silica fume. Materials and mechanical properties, *Building and Environment*, 43(4), 429–437.
7. **Kheradmand Mohammad, Azenha Miguel, Aguiar Jose L.B. de, Krakowiak Konrad J.** (2014), Thermal behavior of cement based plastering mortar containing hybrid microencapsulated phase change materials, *Energy and Buildings*, 84, 526–536.
8. **Kim Kwan Ho, Cho Hee Chan, Ahn Ji Whan**. (2012), Breakage of waste concrete for liberation using autogenous mill, *Minerals Engineering*, 35, 43–45.
9. **Kockal Niyazi Ugur.** (2016), Investigation about the effect of different fine aggregates on physical, mechanical and thermal properties of mortars, *Construction and Building Materials*, 124, 816–825.
10. **Korobko B.O.** (2016) Investigation of energy consumption in the course of plastering machine's work, *Eastern-European Journal of Enterprise Technologies (Energy-saving technologies and equipment)*, 4, 8 (82), 4–11.
11. **Korobko B.O., Vasyliev I.A. (2012)** Laboratory test stand for the mortar pump loading (in Ukrainian), *Collected works (branch of engineering, construction), Poltava, PoltNTU*, 1 (31), 82–86.
12. **Korobko B.O., Vasyliev I.A.** (2014), Mortar ball valve efficiency research according to the law of the piston (in Ukrainian), *Collected works (branch of engineering, construction), Poltava, PoltNTU*, 1(40), 14–19.
13. **Perrot A., Rangeard D., Picandet V., Mélinge Y.** (2013), Hydro-mechanical properties of fresh cement pastes containing polycarboxylate superplasticizer, *Cement and Concrete Research*, 53, 221–228.
14. **Reis J.M.L., Moreira D.C., Nunes L.C.S., Sphaier L.A.** (2011), Experimental investigation of the mechanical properties of polymer mortars with nanoparticles, *Materials science and engineering A-Structural materials properties microstructure and processing,* 528(18), 6083–6085.

DOI 10.1515/ama-2017-0026

FLEXIBLE STRUCTURE CONTROL SCHEME OF A UAVS FORMATION TO IMPROVE THE FORMATION STABILITY DURING MANEUVERS

Cezary KOWNACKI*, Leszek AMBROZIAK*

*Faculty of Mechanical Engineering, Department of Automatics and Robotics, Bialystok University of Technology,
ul. Wiejska45C, 15-351 Bialystok, Poland

c.kownacki@pb.edu.pl, l.ambroziak@pb.edu.pl

received 10 October 2016, revised 18 July 2017, accepted 7 August 2017

Abstract: One of the issues related to formation flights, which requires to be still discussed, is the stability of formation flight in turns, where the aerodynamic conditions can be substantially different for outer vehicles due to varying bank angles. Therefore, this paper proposes a decentralized control algorithm based on a leader as the reference point for followers, i.e. other UAVs and two flocking behaviors responsible for local position control, i.e. cohesion and repulsion. But opposite to other research in this area, the structure of the formation becomes flexible (structure is being reshaped and bent according to actual turn radius of the leader. During turns the structure is bent basing on concentred circles with different radiuses corresponding to relative locations of vehicles in the structure. Simultaneously, UAVs' airspeeds must be modified according to the length of turn radius to achieve the stability of the structure. The effectiveness of the algorithm is verified by the results of simulated flights of five UAVs.

Key words: Unmanned Aerial Vehicles, UAVs Formation, Rigid Formations, Flexible Formations

1. INTRODUCTION

The problem of UAVs formations flights has been intensively studied for many years in many research centers all over the world. Most of the research in this field is focused on three different approaches, i.e. formation flights based on a rigid virtual structure (Norman and Hugh, 2008; Ren and Beard, 2004; J. Shan and Liu, 2005; Cai et al., 2012; Seo et al., 2009; Askari et al., 2015) or a flexible virtual structure (Low and Ng, 2011), swarms using biologically inspired flocking behaviors (Quintero et al., 2013; Kownacki and Ołdziej, 2015; 2016; Virágh et al., 2014) and relations based on the model of leader – follower (Xingping et al., 2003; Yun et. al., 2008; Ambroziak and Gosiewski, 2014). In the first approach, UAVs create a rigid structure, where relative distances between UAVs should be constant during a flight as much as it is possible (Norman and Hugh, 2008). Achieving this becomes a challenge because it requires not only precision control but also real-time motion synchronization. Therefore, in Low and Ng, (2011) a model of flexible virtual structure is proposed, where relative distances can be slightly varied during turns. But proposed structure of control is centralized and it does not consider a collision risk inside the formation as it relies on local generation of reference trajectory for each UAV on basis of the reference trajectory of the leader. The second approach applies behaviors which are inspired by the flocking behaviors of birds. Also, in this case, local flight control depends on information sharing at least between the nearest neighbors of the vehicle (Kownacki and Ołdziej, 2015; 2016). Otherwise, the vehicle cannot determine its own behaviors, especially repulsion or cohesion. The last approach, based on the leader-follower relation, is relatively the simplest one, but as it was proved it requires control switching between position control and the course control to achieve the effective flight (Ambroziak and Gosiewski, 2014).

Despite some progress in the field of multi-UAV systems, a control algorithm, which would offer the effective flight control in real applications for fixed-wing UAVs, has not been thoroughly developed yet. This fact is especially related to the issue of the stability of the formation flight in turns, where each vehicle makes a turn under different aerodynamic conditions as the result of different speeds and different bank angles. Problems with finding an appropriate solution arise from the limitations of available technology and the nature of small fixed-wing UAVs being nonholonomic robots, whose high dynamics combined with small time constants make them sensitive to any external disturbances. Therefore, a position control in a formation requires a real-time processing of navigational data acquired from others UAVs, and it should involve especially a problem of synchronization of flight parameters and their actual errors (Norman and Hugh, 2008). In turn, this requires a lot of bytes to be transmitted smoothly through a wireless communication network inside the formation, what in most cases becomes another technological problem.

To avoid these issues, in contrast to the model in Low and Ng, (2011), we propose a decentralized control algorithm based on a leader as the reference point for other UAVs and two flocking behaviors responsible for local position control, i.e. cohesion and repulsion. The flow of navigational data is organized on the model of cascade, in which transmission is initialized by the leader, whose data is sequentially forwarded by next follower in the structure. This simplifies the structure of wireless network inside the formation. But opposite to our previous research (Kownacki and Ołdziej, 2015; 2016), the structure of the formation becomes flexible (the structure is being reshaped and bent according to actual turn radius of the leader. During turns, the structure is bent basing on concentered circles with different radiuses corresponding to relative locations of vehicles in the structure. Simultaneously, UAVs' airspeeds must be modified according to length of turn radius to achieve the stability of the structure.

2. FORMATION FLIGHT WITH ALGORITHM OF FLEXIBLE STRUCTURE

Regardless to the applied control algorithm, a typical formation flight assumes that relative distances between vehicles must be constant as much as possible. Therefore, UAVs formation usually uses structures, which define reference positions of each UAV in relation to a chosen reference point. The most convenient way, from the practical point of view, is to use a leader of a formation as the reference point to determine desired positions of other UAVs, which will play the role of followers. According to this, the leader must broadcast its actual position and orientation angles to allow the followers to calculate their reference positions in the structure, which become set-points for the local control of UAV. In the proposed approach, local low level control is based on two flocking behaviors, i.e. cohesion and repulsion (Kownacki and Ołdziej, 2015; 2016). The shape of the formation structure may be any as long as the distances between vehicles are exactly defined in a local coordinates frame associated with the formation. In the presented studies, a shape of reversed letter 'V' is used to create a simulated formation of five UAVs. This kind of structure will allow determining clearly noticeable differences between trajectories of the followers flying on opposite sides of the formation structure. A simulated structure of UAVs formation with local coordinate system for reference positions is presented on Fig. 1.

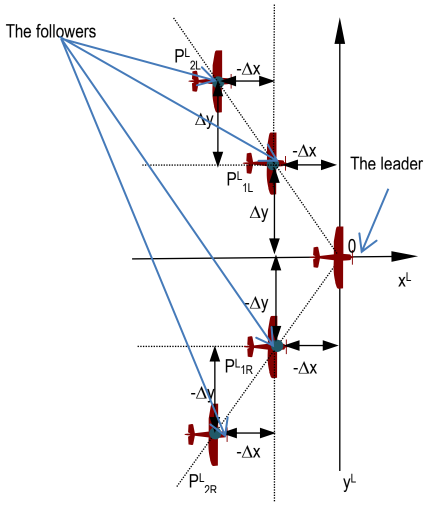

Fig. 1. A structure of the formation of five UAVs based on the shape of reversed letter 'V'

According to the formation structure presented in Fig. 1, reference positions of UAVs can be determined by predefined points located in a local coordinate frame L, whose origin is placed at the gravity centre of the leader, and its axes are parallel to the axes of the leader's body. Therefore, coordinates of these points can be expressed by equation (1). In the equation, index i in the subscripts refers to the order of UAVs placed behind and in reference to the leader, identically on its both sides. While index j refers respectively to the left ($j=L$) and to the right ($j=R$) side of the leader.

$$P_{ij}^L = \begin{bmatrix} x_{ij}^L \\ y_{ij}^L \\ z_{ij}^L \end{bmatrix} = \begin{cases} \begin{bmatrix} -i\cdot\Delta x \\ i\cdot\Delta y \\ 0 \end{bmatrix} & j=R \\ \begin{bmatrix} -i\cdot\Delta x \\ -i\cdot\Delta y \\ 0 \end{bmatrix} & j=L \end{cases} \qquad (1)$$

where: *i* – the order of UAVs in chain on the left side (*j*=*L*) or on the right side (*j*=*R*) in reference to the leader, $\Delta x, \Delta y$ – spacings between UAVs, respectively in x^L and y^L axis.

If the formation structure is rigid, the coordinates of those points P_{ij}^L in the global frame *G*, which is related to local horizon and the north, will be determined by a transformation, which combines a shift of coordinates by the leader's coordinates given in the frame *G* and a rotation around the leader's gravity centre about its orientation angles i.e. roll, pitch and heading. The transformation can be defined by a following equation:

$$P_{ij}^G = P_{LD}^G + D_G^L(\phi_{LD}, \theta_{LD}, \psi_{LD}) \cdot P_{ij}^L \qquad (2)$$

where: D_G^L – a rotation matrix defining elementary rotations between the formation frame *L* and the inertial frame *G*, P_{LD}^G – the position of the leader in the inertial frame *G*, P_{ij}^G – the reference position of the i-th UAV flying on the right (*j*=*R*) or left side (*j*=*L*) of the leader given in the inertial frame *G*, P_{ij}^L – the reference position of the i-th UAV on the right (*j*=*R*) or left side (*j*=*L*) of the leader given in the local frame *L*, ψ_{LD} – a heading angle of the leader, ϕ_{LD} – a roll angle of the leader, θ_{LD} – a pitch angle of the leader.

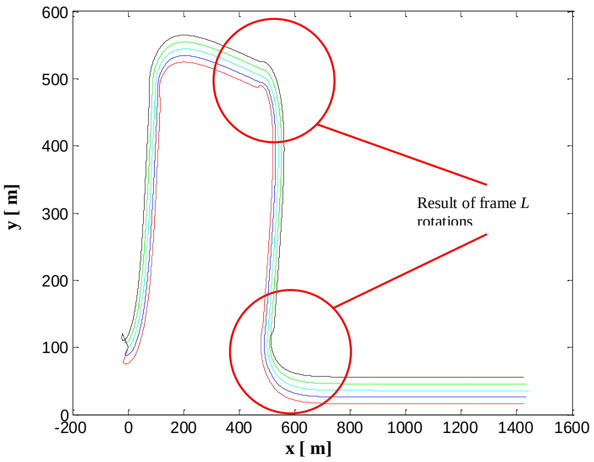

Fig. 2. Ground projections of trajectories of reference UAVs positions for a formation flight based on a rigid structure

Unfortunately, the approach based on the rigid structure can result in deformations of reference trajectories, which are evolutions of points P_{ij}^G in time, especially while the formation makes a turn maneuver. Rotations of the local frame *L* around the leader's gravity centre make turn radiuses of the followers greater than it is in the case of the leader and finally the formation structure is disturbed as it is shown in Fig. 2.

The deformations of UAVs trajectories in Fig. 2 are a strong argument against the use of the approach of the rigid structure. Therefore, a new approach, which will use a flexible structure should be proposed. In the approach of the flexible structure, the formation structure will be constantly modified according to actual turn radius of the leader. This means also that the reference positions of the followers will be modified in relation to the reference point, and relative distances between UAVs will not be constant. In the flexible structure, reference positions of the followers during turns can be defined by finding points of intersections between concentric circles, whose radiuses are determined by a sum of turn radius of the leader (*R*) and coordinates of UAVs reference positions in *y*-axis of the frame *L* (Δy), and lines passing through the center of these circles. The lines will create arcs on the trajectory of the leader, which start in the position of the leader, and whose widths are equal to *i*·Δ*x*, coordinate of reference position in *x*-axis of frame *L* for the i-th UAV. The idea of the flexible structure of a UAVs formation is presented in Fig. 3.

The main rule of the flexible structure in Fig. 3 can be defined briefly as the change of expression of reference positions of UAVs in the local frame *L* from Cartesian coordinates to polar coordinates only when the leader's roll angle is different from zero. In both coordinates systems, relative coordinates of UAVs positions in reference to the leader, i.e. positive and negative multiplications of *Δx* and *Δy* (eq. 1), remain the same, but in the case of polar coordinates system, they are given as widths of arcs and differences in lengths of turn radiuses. Moreover, the origin of polar coordinates system is located at the center of a circle being a part of the leader's trajectory. To determine reference positions of UAVs in the frame *G*, it is necessary to identify a Cartesian representation of relative distances *Δx* and *Δy* expressed as polar coordinates. Let's start with a definition of concentric circles in the frame *L*, which is as follows:

$$\begin{cases} x_{ij}^2 + \left(y_{ij} - R\right)^2 = \left(R - y_{ij}^L\right)^2, & \phi < 0, \\ x_{ij}^2 + \left(y_{ij} + R\right)^2 = \left(-R - y_{ij}^L\right)^2, & \phi \geq 0. \end{cases} \tag{3}$$

where: *R* – turn radius of the leader, x_{ij}, y_{ij} – coordinates of points forming trajectory of the i-th UAV flying on the right (*j*=*R*) or on the left side (*j*=*L*) of the leader, given in the frame *L*, y_{ij}^L –coordinate of the reference position in *y*-axis of the frame *L* for the i-th UAV, which is flying on the right (*j*=*R*) or on the left side (*j*=*L*) of the leader, ϕ - actual roll angle of the leader.

In the next step, equations of lines should be defined. These lines intersect the leader's trajectory. Intersection points together with y-axis specify arcs widths equal to x_{ij}^L –coordinates of the reference positions of UAVs in x-axis of the *L* frame. Angles between those lines and y-axis of the *L* frame are given by equation (4).

$$\alpha_{ij} = \frac{\left|x_{ij}^L\right|}{|R|}. \tag{4}$$

where: *R* – turn radius of the leader, x_{ij}^L – coordinate of reference position in *x*-axis of the frame *L* for the i-th UAV flying on the right (*j*=*R*) or on the left (*j*=*L)* side of the leader.

Therefore, equations of those lines can be formulated as follows:

$$\begin{cases} y_{ij} - R = x_{ij} \cdot tg\left(\frac{\pi}{2} - \alpha_{ij}\right), & \phi < 0, \\ y_{ij} + R = -x_{ij} \cdot tg\left(\frac{\pi}{2} - \alpha_{ij}\right), & \phi \geq 0. \end{cases} \tag{5}$$

If we take right sides of equations (5) and put them respectively into corresponding expressions on the left sides of equations (3), we will obtain x_{ij}^{LF} - coordinate of reference position of UAV in *x*-axis of the frame *L*. Because the followers are always placed behind the leader, i.e. on the left side of *y*-axis of the frame *L*, the sign in the front of square root is negative.

If we take right sides of equations (5) and put them respectively into corresponding expressions on the left sides of equations (3), we will obtain x_{ij}^{LF} - coordinate of reference position of UAV in *x*-axis of the frame *L*. Because the followers are always placed behind the leader, i.e. on the left side of *y*-axis of the frame *L*, the sign in the front of square root is negative.

$$\begin{cases} x_{ij}^{LF} = -\sqrt{\frac{\left(R - y_{ij}^L\right)^2}{1 + tg^2\left(\frac{\pi}{2} - \alpha_{ij}\right)}}, & \phi < 0, \\ x_{ij}^{LF} = -\sqrt{\frac{\left(-R - y_{ij}^L\right)^2}{1 + tg^2\left(\frac{\pi}{2} - \alpha_{ij}\right)}}, & \phi \geq 0. \end{cases} \tag{6}$$

To determine coordinates of UAVs reference positions in *y*-axis of the frame *L*, right sides of equations (6) should be substituted in the place of x_{ij} in equations (5). The equation for coordinate y_{ij}^{LF}, is given as follows:

$$\begin{cases} y_{ij}^{LF} = -tg\left(\frac{\pi}{2} - \alpha_{ij}\right) \cdot \sqrt{\frac{\left(R - y_{ij}^L\right)^2}{1 + tg^2\left(\frac{\pi}{2} - \alpha_{ij}\right)}} + R, & \phi < 0, \\ y_{ij}^{LF} = tg\left(\frac{\pi}{2} - \alpha_{ij}\right) \cdot \sqrt{\frac{\left(-R - y_{ij}^L\right)^2}{1 + tg^2\left(\frac{\pi}{2} - \alpha_{ij}\right)}} - R, & \phi \geq 0. \end{cases} \tag{7}$$

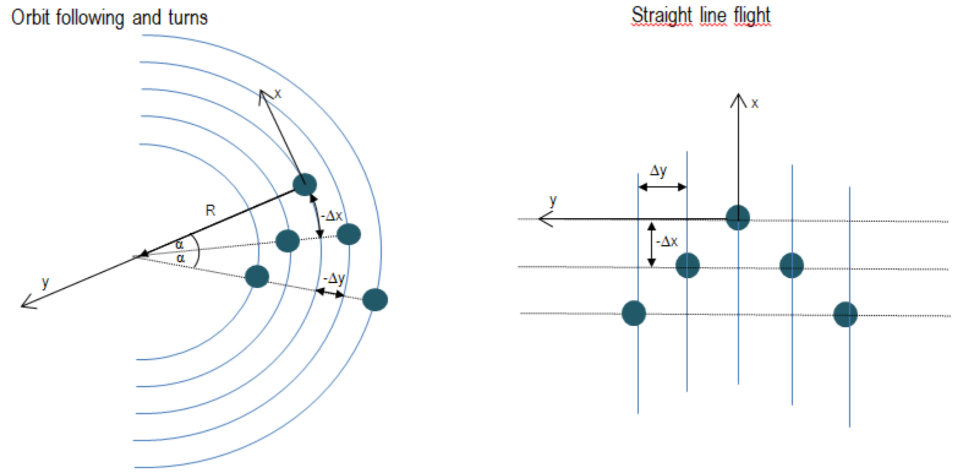

Fig. 3. The idea of the flexible structure of a UAVs formation. On the left side, there is the formation structure, which is modified according to the leader's turn radius *R*, and on the right side, there is the initial structure for a straight line flight

Both equations (6) and (7) define together coordinates of reference positions of UAVs in the flexible structure in the frame *L*, in situation when the formation makes a turn or starts an orbit-following flight scheme. Coordinates in *z*-axis remain constant and they are equal to zero. To implement local controls based on the rules of birds flocking, each UAV must know its reference position given in the global frame *G*. But in contrast to the rigid structure approach, reference positions in the local frame *L* should be rotated around the leader only about its heading angle. Hence, the transformation from the frame *L* to the frame *G* is given by equation (8), which splits the problem into separate cases, i.e. when an absolute value of the leader's roll angle is below and above value of $\boldsymbol{\phi_m}$, at which formation control switches to the flexible structure mode.

$$P_{ij}^{G} = \begin{cases} P_{LD}^{G} + D_{G}^{L}(\psi_{LD}) \cdot \begin{bmatrix} x_{ij}^{LF} \\ y_{ij}^{LF} \\ 0 \end{bmatrix} & |\phi| > \phi_m, \\ P_{LD}^{G} + D_{G}^{L}(\psi_{LD}) \cdot \begin{bmatrix} x_{ij}^{L} \\ y_{ij}^{L} \\ 0 \end{bmatrix} & |\phi| < \phi_m. \end{cases} \tag{8}$$

where: D_g^L – rotation matrix defining a rotation between the frame *L* and the inertial frame *G*, P_{LD}^G – the position of the leader in the inertial frame *G*, P_{ij}^G – the reference position for the *i*-th UAV, flying on the right (*j*=*R*) or left side (*j*=*L*) of the leader, given in the inertial frame *G*, x_{ij}^{LF}, y_{ij}^{LF} – coordinates of the reference position of the i-th UAV flying on the right (*j*=*R*) or left side (*j*=*L*) of the leader, given in the local frame *L*, ψ_{LD} – a heading angle of the leader, ϕ_m – the roll angle of the leader at which the formation control switches to the flexible structure mode.

Reference positions P_{ij}^G in the frame *G* are used to calculate local controls of UAV, whose main purpose is to minimize errors of position tracking. This means that the algorithm of the flexible structure becomes a high level of control, providing coordinates of reference positions as input for a middle level of controls i.e. a control of position tracking. In turn, the control of position tracking together with a necessary control of collision avoidance between UAVs generates set-points for a low-level controls which manages deflections of control surfaces of UAV. In this way, the overall control of UAV is organized in a form of three-stage cascade control, which is presented in Fig. 4.

As the base for both controls of position tracking and collision avoidance, flocking behaviors of birds, in particular, behaviors of cohesion and repulsion can be successfully applied, what was proved in the previous research ((Kownacki C. and Ołdziej D., 2015; Kownacki C. and Ołdziej D., 2016)). However here, the meaning of cohesion and repulsion behaviors should be adapted to the approach of formation flights. Therefore, the behavior of cohesion is used to move UAV towards its reference position instead of a gravity centre of a flock, and airspeed of UAV should be proportional to tracking errors or calculated with PID terms with a dead zone applied around the reference position. In turn, the behavior of repulsion secures UAV against collisions with another UAV, which is a preceding in the structure. The idea of applying behaviors of cohesion and repulsion in a formation flight is shown in Fig. 5.

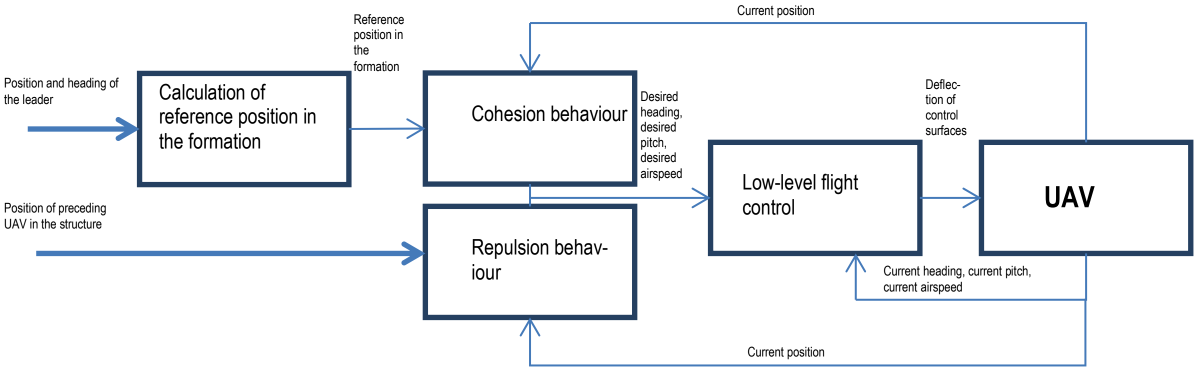

Fig. 4. The structure of the local control of UAV, which is organized in the form of tree-stage cascade control: the first stage – the algorithm of flexible structure, the second stage – flocking behaviors (cohesion and repulsion), the third stage – low level control of flight parameters, roll, pitch, heading and airspeed

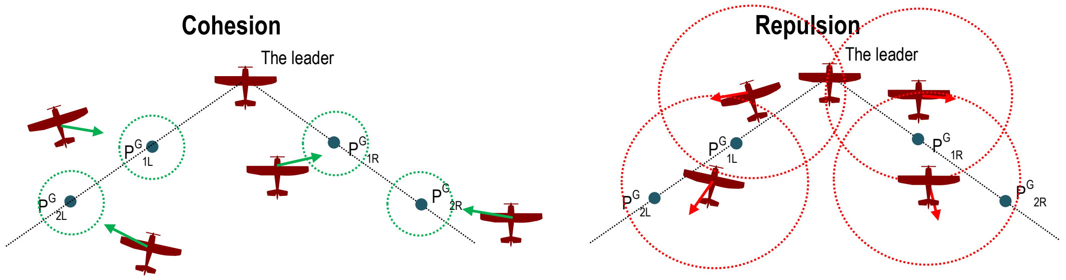

Fig. 5. The idea of using behaviors of cohesion and repulsion in the flight of formation based on the flexible structure. Green dotted circles represent dead zones around reference position, where there is no cohesion and airspeed is the same as the leader's, Red dotted circles represents zones of repulsion around each UAV with except of the leader.

As it was mentioned, cohesion behavior moves UAV towards assigned reference position in the formation structure with an airspeed, which is proportional to a distance between an actual position of UAV and its reference position, and this distance has a meaning of a tracking error. Cohesion behavior is acting only when this tracking error is greater than specified maximal distance, which is a radius D_C of dead zones around reference positions (green dotted circles in Fig. 5). Dead zones are required because they prevent from the instability of flight when the tracking error is nearby zero. Then even a small change of UAV position in relation to the assigned reference position can produce a rapid step change in control signals generated by cohesion behavior. Therefore, UAV should track its reference position keeping a specified distance and inside the dead zone its airspeed should be the same as the leader's. A direction of flight towards reference position determined by cohesion behavior is expressed as a vector defined by the equation below.

$$\overrightarrow{K^{C}{}_{\imath\jmath}} = \frac{1}{\left|\overrightarrow{AP_{\imath\jmath}^{G}}\right|} \cdot \overrightarrow{AP_{\imath\jmath}^{G}} \quad \overrightarrow{AP_{\imath\jmath}^{G}} = \overrightarrow{P_{\imath\jmath}^{G}} - \overrightarrow{P_{UAV_{\imath\jmath}}^{G}}. \tag{9}$$

where: $\overrightarrow{AP_{\imath\jmath}^{G}}$ – a vector which is defined as a difference between the coordinates ($\overrightarrow{P_{UAV_{\imath\jmath}}^{G}}$) of the i-th UAV flying on the right (*j*=*R*) or left side (*j*=*L*) of the leader, given in the inertial frame *G* and the coordinates $\overrightarrow{P_{\imath\jmath}^{G}}$ of assigned reference position in the virtual structure , $\left|\overrightarrow{AP_{\imath\jmath}^{G}}\right|$ - is a distance between the i-th UAV and the reference position in the structure. This is also position tracking error.

As it was mentioned, the airspeed of UAV should be proportionally adjusted to the tracking error and it should be constant or at least reduced to the half of the leader's speed when the tracking error is smaller than the radius D_C. Reducing the airspeeds of the followers allows decreasing their turn radiuses in reference to the leader's. Hence, a relation between airspeed and the tracking error is defined by equation (10):

$$S_{ij}^{d} = \begin{cases} K_p \cdot \cos(\phi) \cdot \left[\left|\overrightarrow{AP_{\imath\jmath}^{G}}\right| + K_I \cdot \int_0^t \left|\overrightarrow{AP_{\imath\jmath}^{G}}\right| d\tau + K_D \cdot \frac{d\left|\overrightarrow{AP_{\imath\jmath}^{G}}\right|}{dt}\right], & \left|\overrightarrow{AP_{\imath\jmath}^{G}}\right| \geq D_c, \\ \beta \cdot S_i \,, & \left|\overrightarrow{AP_{\imath\jmath}^{G}}\right| < D_c. \end{cases} \tag{10}$$

where: K_P, K_D, K_I – gains of PID terms, $\left|\overrightarrow{AP_{\imath\jmath}^{G}}\right|$ – the distance between the i-th UAV and its assigned reference position in the structure (the tracking error), S_{ij}^{d} – the desired airspeed of the i-th UAV, S_i – the leader's airspeed, D_C – a radius of dead zones around the nodes in the virtual structure, ϕ - the leader's current roll angle, β - scaling factor to reduce speed when tracking error is lower than D_C.

The role of repulsion behavior is to secure the formation from collisions between UAVs. It repulses a UAV from another UAV which is a preceding in reference to the leader's position, only when distance between both UAVs is smaller than a safe distance D_R. Therefore, each UAV must know only the position of its precedor. This simplifies information sharing in the formation. A vector, which represents the direction of repulsion is as follows:

$$\overrightarrow{K_{\imath,\imath-1}^{R}} = \begin{cases} \frac{1}{\left|\overrightarrow{P_{\imath\jmath}^{G} P_{\imath-1,\jmath}^{G}}\right|} \cdot \overrightarrow{P_{\imath\jmath}^{G} P_{\imath-1,\jmath}^{G}} & \left|\overrightarrow{P_{\imath\jmath}^{G} P_{\imath-1,\jmath}^{G}}\right| \leq D_R \,, \\ 0 & \left|\overrightarrow{P_{\imath\jmath}^{G} P_{\imath-1,\jmath}^{G}}\right| > D_R, \end{cases} \tag{11}$$

$$\overrightarrow{P_{\imath\jmath}^{G} P_{\imath-1,\jmath}^{G}} = \overrightarrow{P_{\imath\jmath}^{G}} - \overrightarrow{P_{\imath-1,\jmath}^{G}}. \tag{12}$$

where: $\overrightarrow{P_{\imath\jmath}^{G}}, \overrightarrow{P_{\imath-1,\jmath}^{G}}$ – positions respectively of the i-th and the (i–1)-th vehicle flying on the left (*j*=*L*) or the right (*j*=*R*) side of the leader, $\left|\overrightarrow{P_{\imath\jmath}^{G} P_{\imath-1,\jmath}^{G}}\right|$ – a distance between UAVs, D_R – the minimum permissible distance between two UAVs.

The current direction of UAV flight will be dependent on a combination of all behaviours - cohesion and repulsion, which is simply defined as a sum of vectors $\overrightarrow{K_{\imath,\imath-1}^{R}}$ and $\overrightarrow{K^{C}{}_{\imath\jmath}}$. Vector $\overrightarrow{K_{\imath\jmath}}$, being a sum of vectors $\overrightarrow{K_{\imath,\imath-1}^{R}}$ and $\overrightarrow{K^{C}{}_{\imath\jmath}}$, is used to calculate set-point for low-level flight control, i.e. desired pitch and desired heading.

$$\overrightarrow{K_{\imath\jmath}} = \overrightarrow{K_{\imath,\imath-1}^{R}} + \overrightarrow{K^{C}{}_{\imath\jmath}}. \tag{13}$$

These set-points are defined by following equations.

$$\overrightarrow{K_{\imath\jmath}} = \begin{bmatrix} x_{ij} \\ y_{ij} \\ z_{ij} \end{bmatrix}, \tag{14}$$

$$\Psi_{ij}^{d} = atan2\left(\frac{x_{ij}}{y_{ij}}\right), \tag{15}$$

$$\Theta_{ij}^{d} = atan2\left(\frac{z_j}{\sqrt{{x_{ij}}^2 + {y_{ij}}^2}}\right). \tag{16}$$

where: $\overrightarrow{K_{\imath\jmath}}$ – a vector which defines the resultant direction of flight, Ψ_{ij}^{d} – the desired heading angle, Θ_{ij}^{d} – the desired pitch angle.

The control vector, which is the input for low-level of flight control, can be finally defined as:

$$\overrightarrow{u_{\imath\jmath}} = \begin{bmatrix} \Psi_{ij}^{d} \\ \Theta_{ij}^{d} \\ S_{ij}^{d} \end{bmatrix}. \tag{17}$$

To show the differences between the presented approach of flexible structure and virtual rigid structure a series of simulations were made in Matlab – Simulink. In the simulations, a formation of five UAVs flew through different sequences of three waypoints, each time it made at least one turn of about 90 degrees. Results of flights simulation making a comparison between rigid and flexible structure approaches are presented in next section.

3. RESULTS

To identify the main differences in both approaches to formation structures, the same sequence of waypoints and the same flight parameters were used to simulate flights, once based on the rigid structure algorithm and once on the proposed algorithm of the flexible structure. Making a comparison between trajectories of reference positions and UAVs for both approaches allows assessing how much the flexible structure improves the parallelism of UAVs trajectories, what is the main aim of the research. In simulation PD regulators are used to control airspeeds (eq. 10) and actual headings (low-level control) of the followers. Following parameters were also applied: the leader's airspeed 10 m/s, range of repulsion D_R=1 meter, the radius of dead-zones around reference positions in the structure D_C=5 meters, maximum roll angle for each UAV about 30^0, initial headings 90^0, initial positions of UAVs are placed in accordance to location in the structure of the formation. Fig. 6 presents trajectories of UAVs and trajectories of their reference positions for the case of the flexible structure approach on the left and for the case of the rigid structure approach on the right. In Fig. 7, it can be noticed that in the case of rigid structure, headings of outer UAVs in the structure differ from others, i.e. they oscillate in moments when they are flying on the inner sides of turns. But those differences do not correlate with the shape of reference trajectories what reflects in the fact that trajectories of the UAVs turn in opposite direction. Therefore, the most probable reason for the deformations in trajectories of the formation based on the rigid structure approach are overshoots in the roll angle control, which occur at the time of rapid changes of reference positions. And this happens only in the case of rigid structure, what can be proved by plots of roll angles in Fig. 8 and plots of reference heading in Fig. 9.

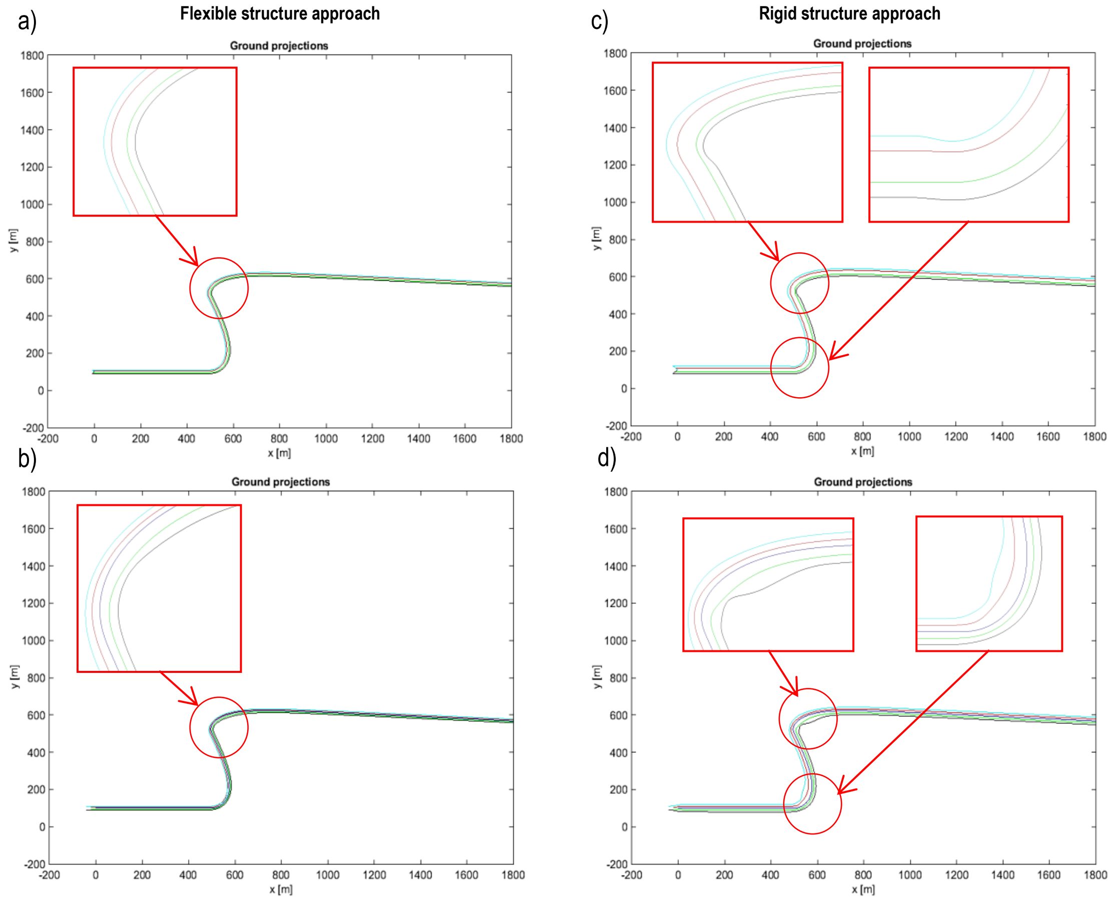

Fig. 6. Trajectories of reference positions and UAVs, respectively for the flexible structure approach: (a) – trajectories of reference positions, (b) – trajectories of UAVs, and the rigid structure approach: (c) – trajectories of reference positions, and (d) - trajectories of UAVs

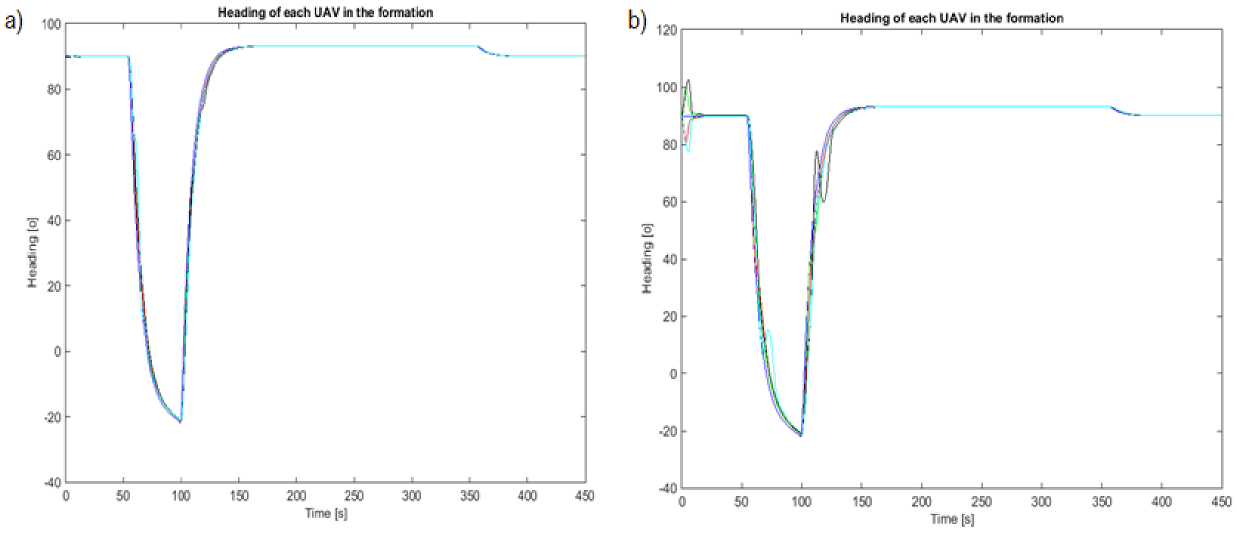

Fig. 7. Headings of UAVs, respectively for the flexible structure approach (a) and the rigid structure approach (b)

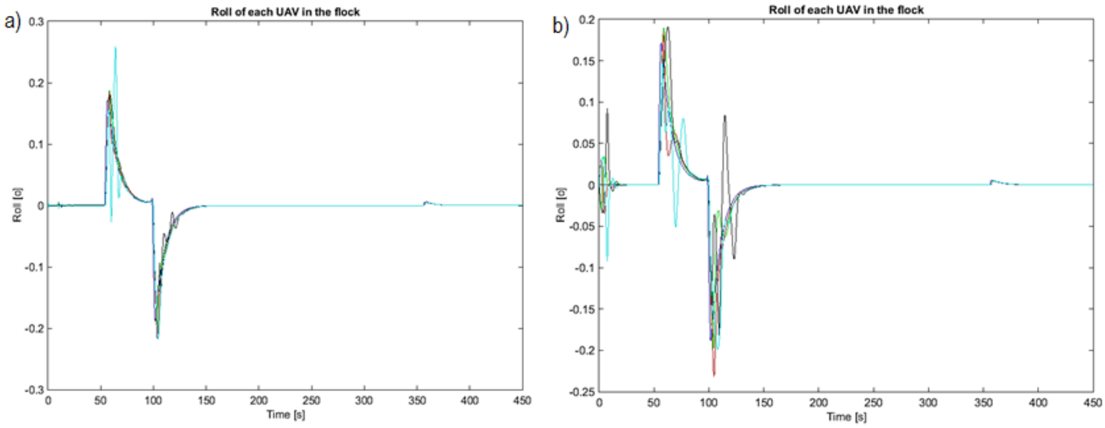

Fig. 8. Roll angles of each UAV in the formation, respectively for the flexible structure approach (a) and the rigid structure approach (b)

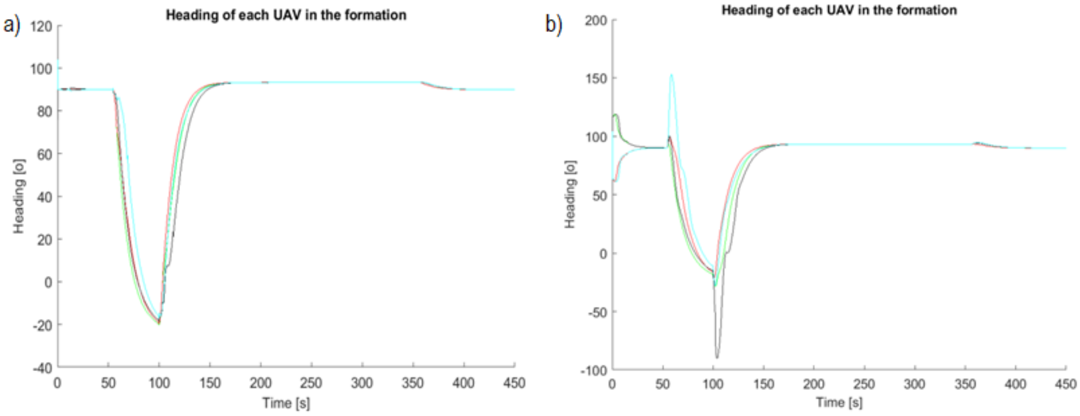

Fig. 9. Reference heading angles of followers in the formation, respectively for the flexible structure approach (a) and the rigid structure approach (b)

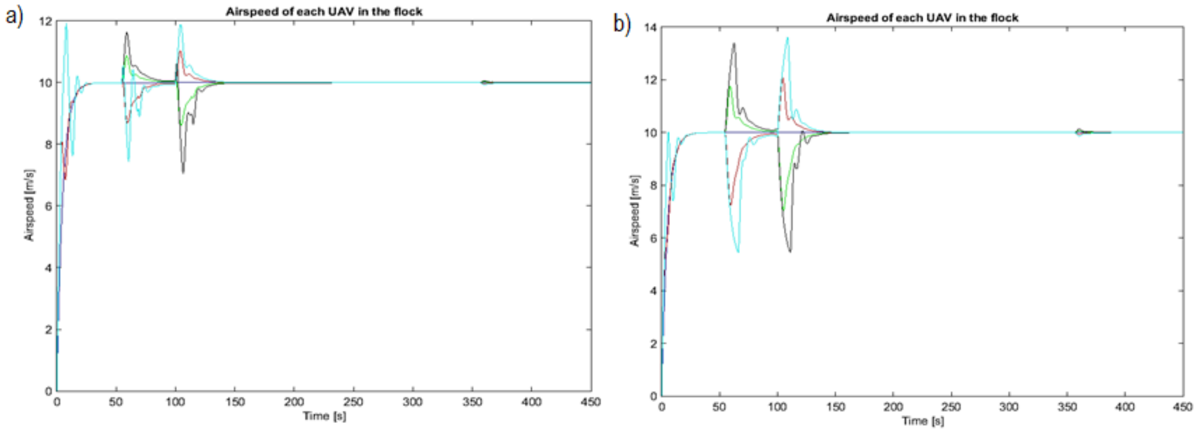

Fig. 10. Airspeeds of each UAV in the formation, respectively for the flexible structure approach (a) and the rigid structure approach (b)

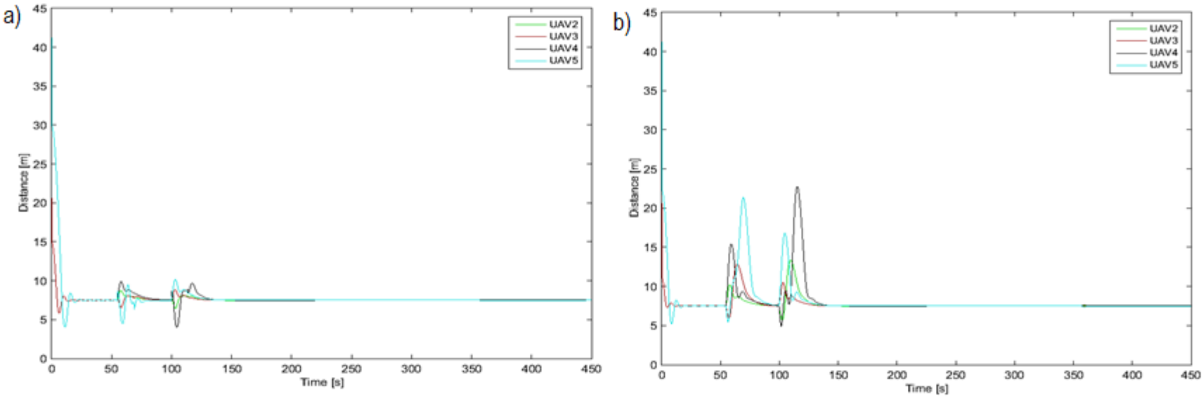

Fig. 11. Tracking error of each UAV in the formation, respectively for the flexible structure approach (a) and the rigid structure approach (b)

Differences between plots of reference headings in Fig. 9 explain higher oscillations of roll angles in the case of the rigid structure approach, which next destabilize the structure of the formation. Therefore, trajectories of UAVs flying on the inner side of turn cease to be parallel to others. Applying the flexible structure instead of the rigid structure decreases these oscillations as the result of generating smoother reference trajectories for the followers. This situation is also confirmed by the position tracking error and airspeeds signals presented in Figs. 10 and 11. Tracking errors are significantly lower during formation flight with flexible structure what also impacts on the control of airspeed as a function of them. Airspeed increases with the growth of tracking error and decreases if it is getting smaller.

4. CONCLUSIONS

The main purpose of the research on algorithms of formation flight designed to UAVs is achieving collective, synchronized and autonomous flight of several UAVs like it could be done by pilots. This still is difficult due to applied technology, which limits possibilities of real-time synchronization between UAVs. Therefore, the most of research is focused on approaches of leader-follower or virtual rigid structure, where the positions of UAVs are related to the leader's position by using predefined geometrical relations. This simplifies the exchange of navigation data between UAVs in the formation, but achieving constant geometrical relations, like it is in rigid structures. becomes more difficult in the case of non-holonomic robots, to which fixed-wing UAVs belong. Applying rigid structures to non-holonomic robots can result in structure rotations which deform trajectories of reference positions causing overshoots in angles of roll and heading.

In the research, the proposition of the new algorithm, which applies a flexible structure to organize formation flights is discussed. The main difference between the proposed algorithm and the approach based on virtual rigid structure is reshaping of the structure in accordance with the turn radius of the leader. Simulations results present that applying the flexible structure approach allows minimizing the impact of structure rotations when the leader changes its heading. Thus, coordinates of reference position do not change rapidly in relation to the UAV, what minimizes heading angle error and reduces oscillations of roll angle. In turn, a stable flight results in better parallelism of trajectories. Applied behaviors of cohesion and repulsion, together with dedicated airspeed control are enough to minimize positions tracking errors effectively. However, tracking errors cannot be smaller than the radius of the dead zone required to stabilize the flight when even a small position displacement can result in a step change of heading error. This issue can be eliminated by heading synchronization what will be the next step of the research.

REFERENCES

1. **Ambroziak L., Gosiewski Z.** (2014), Two stage switching control for autonomous formation flight of Unmanned Aerial Vehicles, *Aerospace Science and Technology*, 46, 221-226.
2. **Askari A.; Mortazavi M.; Talebi H.A.** (2015), UAV Formation Control via Virtual Structure Approach, *Journal of Aerospace Engineering*, 28(1), Article number: 04014047 (online).
3. **Cai D., Sun J., Wu S.** (2012), UAVs Formation Flight Control Based on Behavior and Virtual Structure, *Communications in Computer and Information Science*, 325, 429-438.
4. **Kownacki C., Ołdziej D.** (2015), Flocking Algorithm for Fixed-Wing Unmanned Aerial Vehicles, Advances in Aerospace Guidance, Navigation and Control, Springer, 415-431.
   Kownacki C., Ołdziej D. (2016), Fixed-wing UAVs Flock Control through Cohesion and Repulsion Behaviours Combined with a Leadership, *International Journal of Advanced Robotic Systems*, Article number 36 (online),
5. **Low Ch. B., Ng Q.S.** (2011), A flexible virtual structure formation keeping control for fixed-wing UAVs, *9th IEEE International Conference on Control and Automation*, 19-21 Decemeber, Santiago, 621-626.
6. **Norman H. M. Li, Hugh H.T. Liu** (2008), Formation UAV Flight Control using Virtual Structure and Motion Synchronization, *American Control Conference*, June 11-13, Seattle, USA, 1782-1787.
7. **Quintero S.A.P.,, Collins G.E., Hespanha J.P.** (2013), Flocking with Fixed-Wing UAVs for Distributed Sensing: A Stochastic Optimal Control Approach, *Conference: American Control Conference*, 17-19 June, Washington DC, 2025-2031.
8. **Ren W., Beard R. W.** (2004), Decentralized scheme for spacecraft formation flying via the virtual structure approach, *Journal of Guidance, Control and Dynamics*, 27(1), 73–82.
9. **Reynolds, C.W.** (1987), Flocks, herds and schools: a distributed behavioral model. In ACM SIGGRAPH Computer Graphics, *Proceedings of ACM SIGGRAPH '87*, Anaheim, USA, 27-31 July, ACM Press: New York, USA, 25-34.
10. **Seo J., Ahn Ch., Kim Y.** (2009), Controller Design for UAV Formation Flight Using Consensus based Decentralized Approach, *AIAA Infotech@Aerospace Conference Unmanned, Unlimited Conference*, 6-9 April, 248-259.
11. **Shan J., Liu H.T.** (2005), Close-formation flight control with motion synchronization, *Journal of Guidance, Control and Dynamics*, 28(6), 1316–1320.
12. **Shao Z., Zhu X., Zhou Z., Wang Y.** (2014), A Nonlinear Control of 2-D UAVs Formation Keeping via Virtual Structures, Intelligent Robotics and Applications, *Lecture Notes in Computer Science*, 8917, 420-431.
13. **Virágh Cs., Vásárhelyi G., Tarcai N., Szörényi T., Somorjai G., Nepusz, T., Vicsek, T.** (2014), Flocking algorithm for autonomous flying robots, *Bioinspiration & Biomimetics*, 9(2), Article number 025012 (online).
14. **Xingping Ch., Serrani A., Ozbay H.** (2003), Control of leader-follower formations of terrestrial UAVs, *Proceedings. 42nd IEEE Conference on Decision and Control*, 9-12 December, 498-503.
15. **Yun B., Chen B.M., Lum K.Y., Lee T.H.** (2008), A leader-follower formation flight control scheme for UAV helicopters, *IEEE International Conference on Automation and Logistics*, 1-3 Septemeber, 39-44.

The research was realized within the project No S/WM/1/2017 and funded by Polish Ministry of Science and Higher Education.

DOI 10.1515/ama-2017-0027

LABORATORY TESTING OF VELOCITY SENSING IN A MAGNETORHEOLOGICAL DAMPER WITH POWER GENERATION

Bogdan SAPIŃSKI

Department of Process Control, AGH University of Science and Technology, aleja Mickiewicza 30, 30-059 Cracow, Poland

deep@agh.edu.pl

received 15 February 2017, revised 18 July 2017, accepted 7 August 2017

Abstract: The study summarises the results of experimental examination of velocity sensing capability in a prototype of a magnetorheological damper with power generation (MRD). The device has two main components: an electromagnetic power generator and an MR damper. The study outlines the structure of the device with the main focus on the generator part, and provides results of tests performed under the idle run. The discussion of demonstrates the potentials of MRD action as a velocity-sign sensor and presents key issues which need to be addressed to enable its real life applications.

Key words: MR Damper, Power Generator, Voltage, Velocity, Sensing

1. INTRODUCTION

Recent years have witnessed a major advances in self-powered MR dampers which are able to recover energy from external excitations and to adjust themselves to excitations by varying damping characteristics. It has also been established that information about relative velocity across such MR dampers can be extracted on voltage generated by the generator giving the devices the self-sensing capability i.e. can act as a velocity sensors. An increasing number of research reports on this subject have appeared in the last decade. For example, (Jung et al., 2009) investigated experimentally the sensing capability of the generator incorporated in the MR damper-based vibration control system and demonstrated that the device may be considered as a velocity-sign sensor. Also, (Jung et al., 2010) studying a sensing capability of such system showed that the generator could act as a velocity sensor for common control methods in MR damper-based systems. (Wang et al., 2010) proposed an integrated relative displacement self-sensing MR damper to realize the integrated relative displacement sensing and controllable damping. Based on the extension of the presented idea, the prototype of such MR damper was designed, fabricated and tested by (Wang and Bai, 2013). (Chen and Liao, 2010) reported that it is possible to engineer an MR damper with the power generation feature which integrates energy harvesting, dynamic sensing and MR damping technologies in a single device. Also, (Chen and Liao, 2012) performed theoretical and experimental studies of an MR damper prototype which had both self-powered and self-sensing capability. (Zhu et al., 2012) presented self-powered and sensor-based MR damper systems since such systems could be particularly useful in large-scale civil constructions where the power supply is impractical. (Li et al., 2013a, 2013b) presented an innovative concept of a mechanical motion rectifier which converts bidirectional motion into unidirectional motion.

This paper deals with velocity sensing of the MRD prototype and recalls three former works of the author (Sapiński, 2011, 2014, Sapiński et al., 2016)). The study is organized as follows. Section 2 describes the structure of the device with the main focus on the power generator part. Section 3 provides results of tests performed under idle run to demonstrate the self-sensing potentials. The conclusions are given in Section 4.

2. STRUCTURE OF THE DEVICE

The sectional view of the MRD with numeric symbols (1-17) indicating its crucial components is shown in Fig. 1. Two main components are the electromagnetic power generator (harvester) and the MR damper. The generator is axially symmetrical and complete with three systems of permanent magnets (three magnets in each), two inner spacers (height 9 mm) and two outer spacers (height 6.5 mm), and the coil (height 18.5 mm, inside diameter 31 mm, outside diameter 77 mm, distance between coil sections 5 mm) with two winding sections incorporating 273 turns each, wound on a carcass (height 20.5 mm, wall thickness 1 mm) with copper foil with one-sided insulation (foil thickness – 0.05 mm, insulation thickness – 0.03 mm). The magnets made of NdFeB grade N35, are ring-shaped (inside diameter 12 mm, outside diameter 30 mm, height 5 mm) and display axial magnetisation with direction indicated by arrows. The magnets and spacers are mounted on a non-magnetic stainless steel shaft. Coil winding sections, placed inside a housing (height 50 mm, wall thickness 3 mm), are connected such that as the moving part moves with surrounding vibration, they experience a change in flux linkage and thus induced voltages should sum up. The coil housing and spacers are made of ferromagnetic steel SAE 1215. The generator components are placed inside the housing, locked with the lower and upper covers. Sleeves provided in the cover ensure the axial movements of the piston rod. The fixture to hold the generator is attached to the lower cover. The height of an air slit between the carcass and the magnet systems is 0.5 mm.

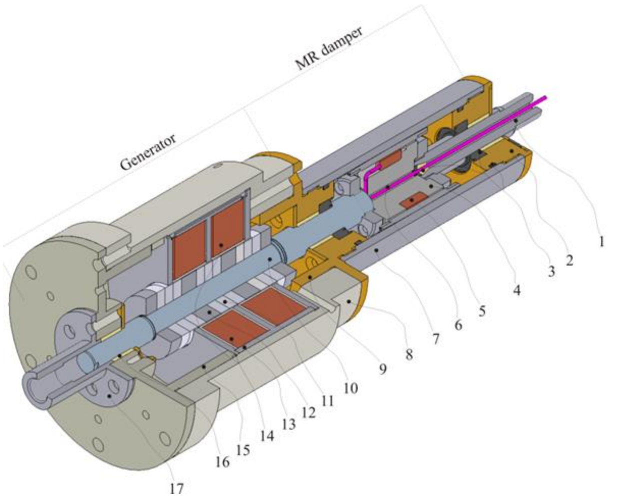

Fig. 1. Sectional view of the MRD: 1 – piston rod, 2 – brass lid, 3 – rubber seals, 4 – piston, 5 – control coil, 6 – wire, 7 – damper housing, 8 – device housing, 9 – brass connector, 10 – rod, 11 – neodymium magnets, 12 – spacers, 13 – housing, 14 – coils, 15 – lid, 16 – slip sleeves, 17 – holder

The damper is an axially-symmetrical single-tube damper with a circumferential slit. The piston rod made of non-magnetic austenite stainless steel is attached to the piston via ferromagnetic kidney plates and sealed with rings. The rings together with the sleeves are placed in two co-axial guides to guide the piston rod. The damper coil is made of copper wire 0.4 mm in diameter wound on the carcass, forming 306 windings. The coil is placed on the core made of ferromagnetic steel SAE 1215. The lead power-supplying the control coil is let out via a hole in the piston rod. The damper housing, made of ferromagnetic steel SAE 1025, is locked on both ends by covers made of austenitic stainless steel. The damper contains 36.5 ml of the MR fluid. The resistance of the generator coils is 141 mH and the resistance is 2.45 Ω. The geometric parameters of the device are summarised in (Sapiński, 2014).

3. TESTS, RESULTS AND DISCUSSION

The MRD was tested in the test rig (see Fig. 2) that incorporates the MTS test machine (www.mts.com), the data acquisition system comprising a portable computer, I/O board DAQPad-6052E of National Instruments and the supporting software LabView. The MTS machine was programmed to generate sine and triangular excitations with an amplitude of 0.01 m and a frequency of 1 Hz and 6 Hz. Tests were carried out during the idle run of the MRD generator part. The measurements of output voltage (electromotive force) u were taken and position x was duly registered. The values of u and x were recorded in 10 cycles of the piston motion. The sampling frequency for each channel was 1 kHz per cycle. The piston velocity $\dot{x}$ was obtained by differentiating the position x.

The results revealed the velocity sensing capability of the MRD, demonstrated by exemplary plots shown in Figs 3−4 showing the time histories (relative time $t{\cdot}f$) of piston velocity $\dot{x}$ and voltage u induced in the generator under sine excitations with amplitude of 0.01 m and frequency of 1, 3 and 6 Hz. It is apparent that plots in Fig. 4 agree with the plots in Fig. 3, though there are certain discrepancies. Plots of velocity $\dot{x}$ plots follow the sine wave patterns whilst of voltage u are shaped like deformed sine lines. These deformations are related to configuration of the magnetic circuit in the generator (the system of magnets) and the associated flux density distribution. Plots reveal characteristic peaks, resulting from the changes of the piston velocity sign. It appears that velocity plots are not smooth, which is caused by the fact the velocity signal is obtained via numerical differentiation of the registered position signal x, which involves noise. This issue can be illustrated by comparing the graphs in Fig. 5, plotting the differentiated signal of an ideal sine wave and that produced by the test machine, registered as a sine wave (excitation) x and then differentiated. It is worthwhile to mention that velocity and voltage plots pass through the zero point at the identical time instants.

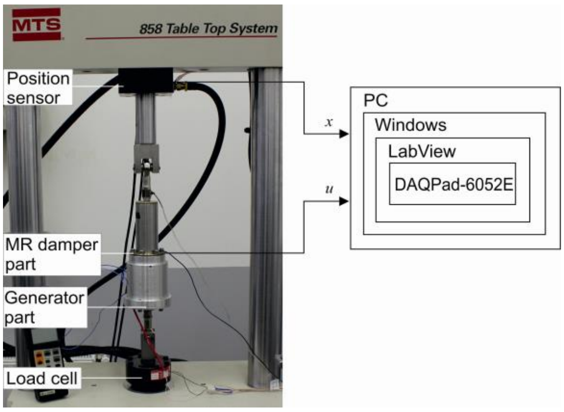

Fig. 2. Schematic diagram of the test rig

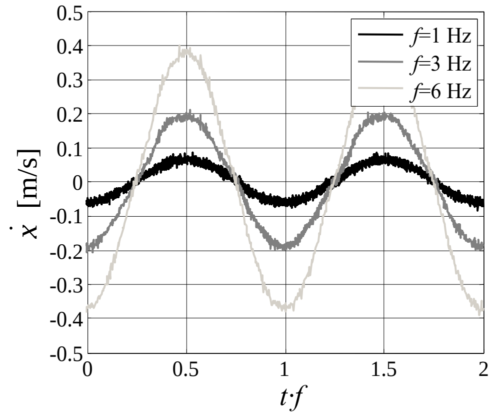

Fig. 3. Time histories of velocity $\dot{x}$; sine excitation, amplitude 0.01 mm

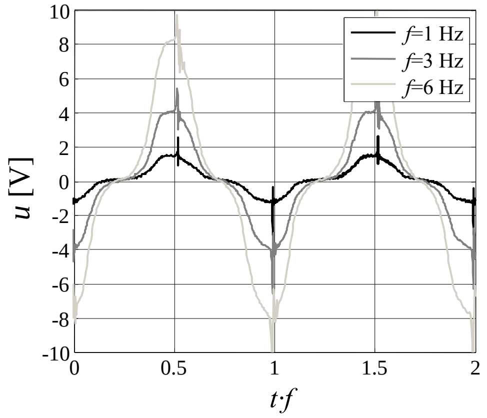

Fig. 4. Time histories of voltage u; sine excitation, amplitude 0.01 mm

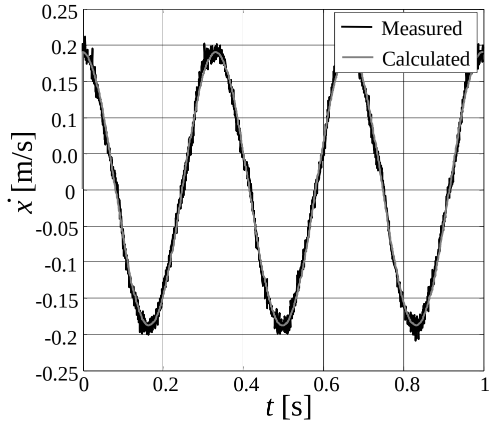

Fig. 5. Time histories of velocity after differentiating and calculating $\dot{x}$; sine excitation, amplitude 0.01 m, frequency 3 Hz

It should be noticed that for an ordinary electromagnetic power generator the permanent magnets generate the magnetic field whose distribution in the generator's region is determined by configuration of magnets and their position with respect to the coils' housing. The magnets remaining in respective movement with regard to the coil give rise to induction of voltage in the coil, that voltage being proportional to the velocity. In consideration of the fact that velocity of magnets is low, the effects of eddy currents induced in conducting elements of the generator can be neglected. Then the output voltage is proportional to the velocity. However, for the specially designed power generators the relationship between these two quantities is not always straightforward. Therefore, to obtain the direct information about velocity, special velocity sensing algorithms have to be developed.

In the work (Sapiński et al., 2016) only the self-powered capability of the MRD was tested. The main objective of the tests performed in this study was to confirm that the MRD could provide information about velocity across the damper that could be useful for controlling system dynamics. This can be achieved by implementation of control algorithms that utilize the velocity across the damper to determine control output (Karnopp et al., 1974; Jansen and Dyke, 2000). As demonstrated in (Chen and Liao, 2012) such approach requires an appropriate sensing function. For this purpose the authors proposed and validated a velocity-sensing method for the developed self-sensing MR damper with power generation. The method, however, requires real-time signal processing. The advantage of the defined sensing function is that it can be applicable to various control algorithms. Moreover the developed device will have good performance for broad vibration-damping applications.

As described in Section 2, the MRD has the damper part and the generator part. The damper part, having a piston assembly, is moveable to the cylinder under an external excitation while the generator part produces electrical power according to the relative movement between the piston and the cylinder assembly. On the basis of the acquired u and calculated $\dot{x}$ data sets registered at sine and triangular excitations with an amplitude of 0.01 m and a frequency of 1 Hz and 6 Hz, the relationship between these two quantities was identified. In this procedure the function polyfit.m available in MATLAB was used. Let us assume that that the relationship between e and$\dot{x}$ can be approximated by the following polynomial of 1-st order $u = \kappa\dot{x} + \sigma$. If so, the value of directional coefficient $\kappa$and shift coefficient σ have to be calculated. Fig. 6 compares the plot of rms u versus$\dot{x}$obtained from experimental data with that calculated in the identification procedure. The plot denoted by dash line was derived on the calculated coefficients κ=21.86 V·s/m and σ=0 V. It can be seen that rms u as function $\dot{x}$ is nearly linear. Time histories of velocity $\dot{x}$ and $u = 21.86\dot{x}$ obtained under sine excitation at amplitude of 0.01 m and frequency of 1 and 4 Hz are shown in Fig. 7.

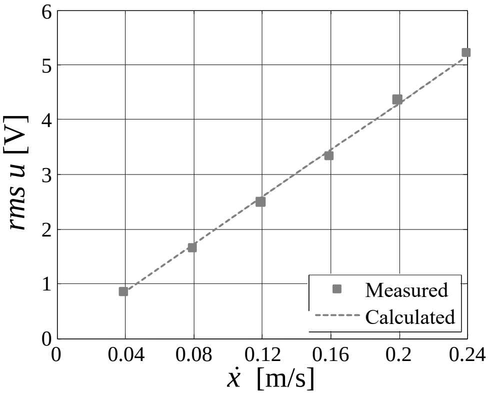

Fig. 6. Voltage *rms u* vs. velocity $\dot{x}$

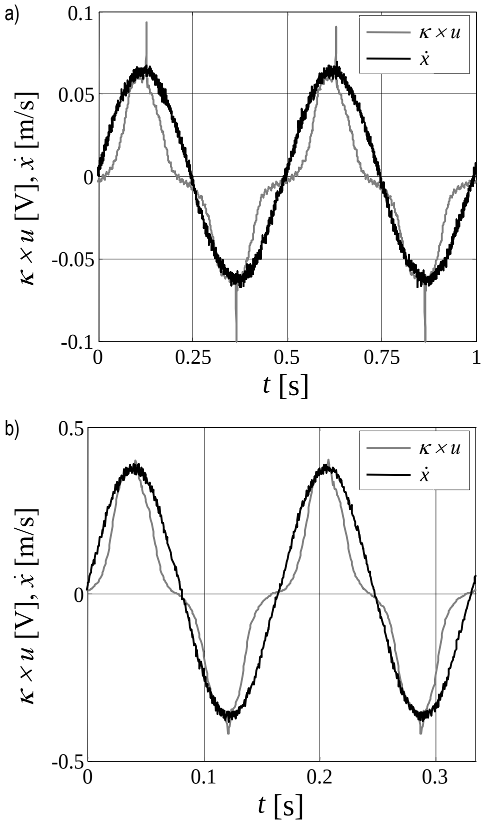

Fig. 7. Time histories of velocity $\dot{x}$ and voltage u; sine excitation, amplitude 0.01 mm, frequency: a) *f*=1 Hz, b) *f*=4 Hz

4. SUMMARY

The study investigates the velocity sensing capability in the MRD prototype. For this purpose the generator part of the device was tested under the idle run in laboratory conditions. The measurements of output voltage of the generator and position were taken and the tests results were processed accordingly. The obtained time histories of voltage and velocity were then analysed. The linear relationship between voltage and velocity was established enabling the comparison of registered voltage and velocity signals reconstructed from voltage data sets. The discussion of test results reveals that in order to reconstruct the velocity signal from the voltage produced by the generator a special velocity-sensing method involving real-time signal processing has to be developed. The tested velocity sensing capability of the MRD is most useful for collecting dynamic information required for system dynamics control.

Further research efforts will concentrate on the method development and its validation at higher excitation frequencies and on reconstruction of velocity signals from voltage produced by applying an accelerometer instead of the position sensor.

REFERENCES

1. **Chen C.**, **Liao W. H.** (2010), A self-powered, self-sensing magnetorheological damper, *Proceedings of IEEE Conference on Mechatronics and Automation*, 1364−1369.
2. **Chen C.**, **Liao W. H.** (2012), A self-sensing magnetorheological damper with power generation, *Smart Materials and Structures*, 21, 025014.
3. **Jansen L. M.**, **Dyke S. J.** (2000), Semi-active control strategies for MR dampers. ASCE, *Journal of Engineering Mechanics*, 126(8), 795–803.
4. **Jung H. J.**, **Jang D. D.**, **Cho S. W.**, **Koo J. H.** (2009), Experimental verification of sensing capability of an electromagnetic induction system for an MR fluid damper based control system, *11th Conference on Electrorheological Fluids and Magnetorheological Suspensions, Journal of Physics: Conference Series,* 149, 012058.
5. **Jung H. J.**, **Jang D. D.**, **Koo J. H.**, **Cho S. W.** (2010), Experimental Evaluation of a 'Self-Sensing Capability of an Electromagnetic Induction System Designed for MR Dampers, *Journal of Intelligent Material Systems and Structures*, 21, 837−836.
6. **Karnopp D. C.**, **Crosby M. J.**, **Harwood R. A.** (1974), Vibration control using semi-active force generator, *ASME Journal of Engineering for Industry*, 96(2), 619-626.
7. **Li Z, Zhuo L, Luhrs G, Lin L., Qin Y.(** 2013b), Electromagnetic Energy harvesting shock absorbers: design, modeling and road tests, *IEEE Transactions Vehicle Technology*, 62, 1065–74.
8. **Li Z.**, **Zhuo L.**, **Kuang J.**, **Luhrs G.** (2013a), Energy-Harvesting Shock Absorber with a Mechanical Motion Rectifier, *Smart Materials and Structures*, 22, 028008.
9. **Sapiński B.** (2011), Experimental study of a self-powered and sensing MR damper-based vibration control system, *Smart Materials and Structures*, 20, 105007.
10. **Sapinski B.** (2014), Energy harvesting MR linear damper: prototyping and testing, *Smart Materials and Structures*, 23, 035021.
11. **Sapinski B.**, **Rosół M.**, **Węgrzynowski M.** (2016), Investigation of an energy harvesting MR damper in a vibration control system, *Smart Materials and Structures*, 25, 125017.
12. **Wang D. H.**, **Bai X. X.** (2013), A magnetorheological damper with an integrated self-powered displacement sensor, *Smart Materials and Structures*, 22, 075001.
13. **Wang D. H.**, **Bai X. X.**, **Liao W. H.** (2010), An integrated relative displacement self-sensing magnetorheological damper: prototyping and testing, *Smart Materials and Structures*, 19, 105008.
14. **Zhu S. Y.**, **Shen W. A.**, **Xu Y. L.**, **Lee W. C.** (2012), Linear electromagnetic devices for vibration damping and energy harvesting: Modeling and testing, *Engineering Structures*, 34, 198−212.
15. www.mts.com

This work is supported by AGH University od Science and Technology under research program No. 15.11.130.431.

MODIFICATION OF TIN COATINGS BY ION IMPLANTATION

Jerzy NAROJCZYK*, **Dmitrij MOROZOW***

*Faculty of Mechanical Engineering, Kazimierz Pułaski University of Technology and Humanities,
ul. Malczewskiego 29, 26–600 Radom, Poland

jerzy.narojczyk@uthrad.pl, d.morozow@uthrad.pl

received 11 January 2016, revised 19 July 2017, accepted 9 August 2017

Abstract: The high-speed steel HS 6-5-2 cutting inserts coated with TiN were subjected to ion implantation with both silicon (dose $2x10^{17}Si^+/cm^2$) and silicon with nitrogen ions (dose $(1+1)x10^{17}(Si^+ + N^+)/cm^2$) on the subsurface layer of the rake face. Microhardness was examined before and after ion implantation. The composition and structural properties of the subsurface layer were examined by Glow Discharge Optical Emission Spectroscopy (GD-OES). The turning tests of 40H construction steel with the use of the cutting inserts implanted and non-implanted were performed. During the tests the two components of the net cutting force (the main cutting force F_c and feed force F_f) as well as the wear parameters VB on the major flankalong with the surface roughness (Ra) were measured. The implanted inserts exhibited higher durability compared to non-implanted ones.

Keywords: Ion Implantation, TiN, Silicon, HSS, Turning

1. INTRODUCTION

Good resistance to impact loads of HSS tools means that they are still used during various types of machining. The limiting factor in their application is faster loss of cutting properties during processing at higher cutting speeds. Improving the wear resistance of these steels can be achieved using several methods, egz.: by powder metallurgy for the manufacturing (Lindskog, 1993), by the PVD processes for coatings (Keenan et al., 1998) or the use of the ion technology to modify the properties of the steels' surface layer or coatings (Hensel et al., 1989; Narojczyk et al., 2005; Zhang et al., 2004; 2007). Ion implantation into the working surfaces of cutting tools allows to change certain of their characteristics (depending on the choice of dopant elements and the parameters of the process) (Liu et al., 1995; Perez et al., 1999; Shalnov et al., 2011; Mikula et al., 2011; Baojian et al., 2014). Implanted ions change the structure and chemical composition of the surface layer (Sun et al., 2010). The consequence of these changes is an increase of the wear resistance. The research done by other authors (Gerth et al., 2008; Kieckow et al., 2006; Martev et al., 2008; Mikula et al., 2011; Musil, 2012) show that the method of ion implantation can create transition layer with specified composition which enhances the adhesion of the TiN layer into the substrate and thereby improves its utility properties.

Good example of this technology may be the modification of TiN coatings with aluminum, boron or silicon ions, which stabilize the coating at higher temperatures (Zhang et al., 2004; 2007; Yang et al., 2007; Grančič et al., 2014). The purpose of this study was to evaluate the effect of ion implantation of silicon or silicon and nitrogen into the TiN subsurface layer on the properties of the rake face of HS 6-5-2 inserts.

2. EXPERIMENTAL PROCEDURE

For the purpose of the study, the samples from HS 6 – 5 – 2 (SW7M) high speed steel have been prepared in the form of SPUN 1203 04 (Fig. 1) standard inserts, and in the form of 3 mm cylinders with the diameter of 28 mm. The samples were coated with TiN (process: BALINIT®A by Balzers Sp. z o.o. Polkowice). The subsurface layer of the rake faces of all samples were subjected to ion implantation with silicon (Si^+) or silicon with nitrogen ($Si^+ + N^+$) ions. Parameters of the process have been presented in Tab. 1.

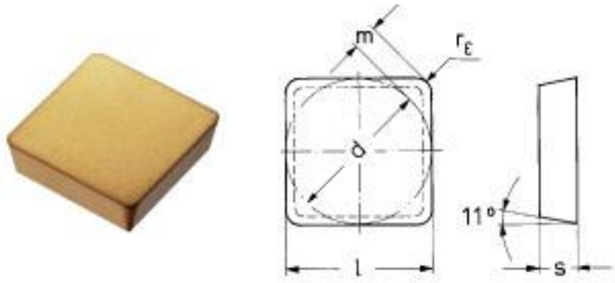

Fig. 1. The SPUN 1203 04 insert from HS 6 – 5 – 2 with TiN

Tab. 1. Parameters of high speed steel HS 6-5-2 inserts implantation.

HS 6-5-2 Inserts	Ion	Energy
Non implanted	-	-
Implanted with Si^+	$2x10^{17}$ Si^+/cm^2	80 keV
Implanted with $Si^+ + N^+$	$(1+1)x10^{17}$ $(Si^+ + N^+)/cm^2$	80 keV

The implantation was carried in TITAN direct beam ion implanter with MEVVA type ion source (fig. 2). Vacuum in the

DOI 10.1515/ama-2017-0028

implanter working chamber was at a level of $2 \div 4 \cdot 10^{-4}$ Pa and the sample temperature did not exceed 200°C.

The machining parameters were gathered in the Tab. 2. The turning tests were performed without cooling liquid. The geometry of the inserts used during machining were the following: tool clearance $\alpha_o = 6^0$, tool rake angle $\gamma_o = 5^0$, tool cutting edge angle $\kappa_r = 75^0$, corner radius $r_\varepsilon = 0.4$ mm (Fig. 3).

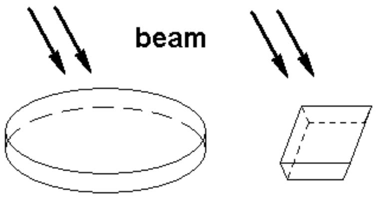

Fig. 2. The samples used for the tests

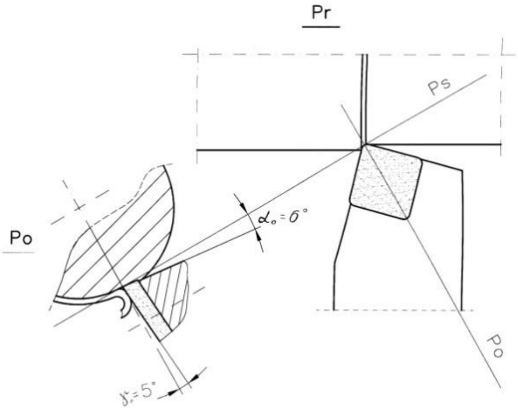

Fig. 3. The geometry of the insert used during turning

Tab. 2. Cutting conditions for the turning tests

Cutting speed v_c [m/min]	Feed rate f [mm/rev]	Cutting depth a_p [mm]
50	0.1	1

In order to determine the changes in the subsurface layer of the TiN coatings caused by implantation, the element composition analysis was performed on cylindrical samples. The Glow Discharge Optical Emission Spectrometry (GD-OES) was performed on JY 10000 RF spectroscope by Jobinn Yvon. This is a known method used for analyzing the chemical composition of the surface layers (Barbaszewski et al., 1989; Seidel et al, 1997). Atoms are sputtered from the sample surface in an argon (Ar) glow discharge. The sputtered atoms recombine with electrons in the plasma discharge. The light emitted from this recombination is analyzed using an optical emission spectrometer in order to obtain a depth profile of chemical composition (Fig. 4) (Toshiba, 2015).

The following elements were found in the surface layer: titanium (Ti), chromium (Cr), nitrogen (N), silicon (Si), tungsten (W), molybdenum (Mo), vanadium (V), and iron (Fe). Results have been presented in the Fig. 5.

Hardness measurements of layers prior and post implantation were done with the Vickers 402 MVD hardness meter by Wilson Wolpert.

Turning tests on annealed 40H steel of hardness 180 HB were performed on prepared samples. Tests were performed on AVIA Turn 30 turning machine. The wear of the samples was determined by periodic measurements of the wear parameters VB on the major flank (Fig. 6) using microscope. The measurements of the surface roughness of the machined surfaces (Ra) were performed on SJ301 by Mitutoyo after each turning (Fig. 7).

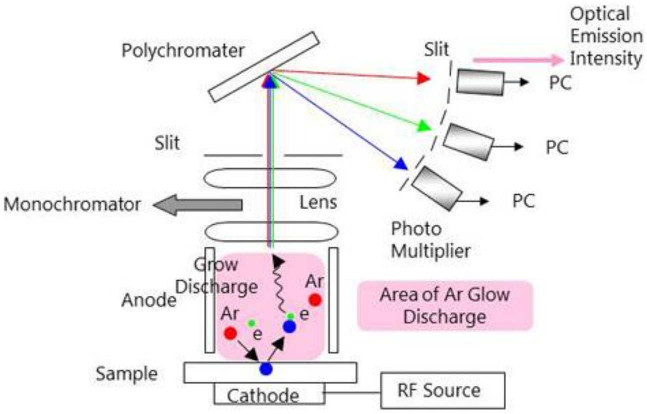

Fig. 4. Principle of operation RF GD-OES (Toshiba, 2015)

The forces during machining were measured with load cell dynamometer capable of measuring cutting force F_c and feed force F_f components. The average values were presented in the Fig. 8.

3. RESULTS AND DISCUSSION

The results of hardness measurements for both, implanted and non implanted TiN layers indicate a slight increase of silicon implanted layer, whereas in the case of silicon plus nitrogen implantation, the hardness decreased (Tab. 3).

Tab. 3. Hardness of the TiN coatings

HS 6-5-2 Inserts	Hardness [HV0.1]
Non implanted	$940^{\pm 27}$
Implanted with Si^+	$965^{\pm 32}$
Implanted with $Si^+ + N^+$	$870^{\pm 22}$

The former case is the effect of introduction of the silicon ions into the crystal lattice, the latter is probably due to nitrogen ions knocking out previously implanted silicon ions from the TiN surface layer.

The results of chemical analysis of the HS 6-5-2 inserts' TiN surface layers are presented in the Fig. 5.

Implanted layers indicate the presence of silicon with maximum at a certain depth from the surface (which is innate to this kind of processes).

Measurements of HS 6-5-2 steel inserts with implanted and non-implanted coatings, conducted after machining, indicate significant wear decrease on the major flank (VB parameter), especially in the case of silicon plus nitrogen implantation (Fig.6).

Similar tendency was observed in the case of roughness measurements (Ra) (Fig. 7) of the machined surfaces, especially when silicon plus nitrogen implanted inserts were used, where Ra

DOI 10.1515/ama-2017-0028

decreased by 50%.

The values of cutting forces (F_c) during machining with implanted samples, were observed to be smaller compared with non-implanted case. This is especially clear for the feed force (F_f) in fig. 8. This is probably due to the change in the conditions of friction on the rake face of the cutting insert as a result of ion implantation. Similar results were also observed by other researchers (Shalnov et al, 2011; Yang et al., 2007).

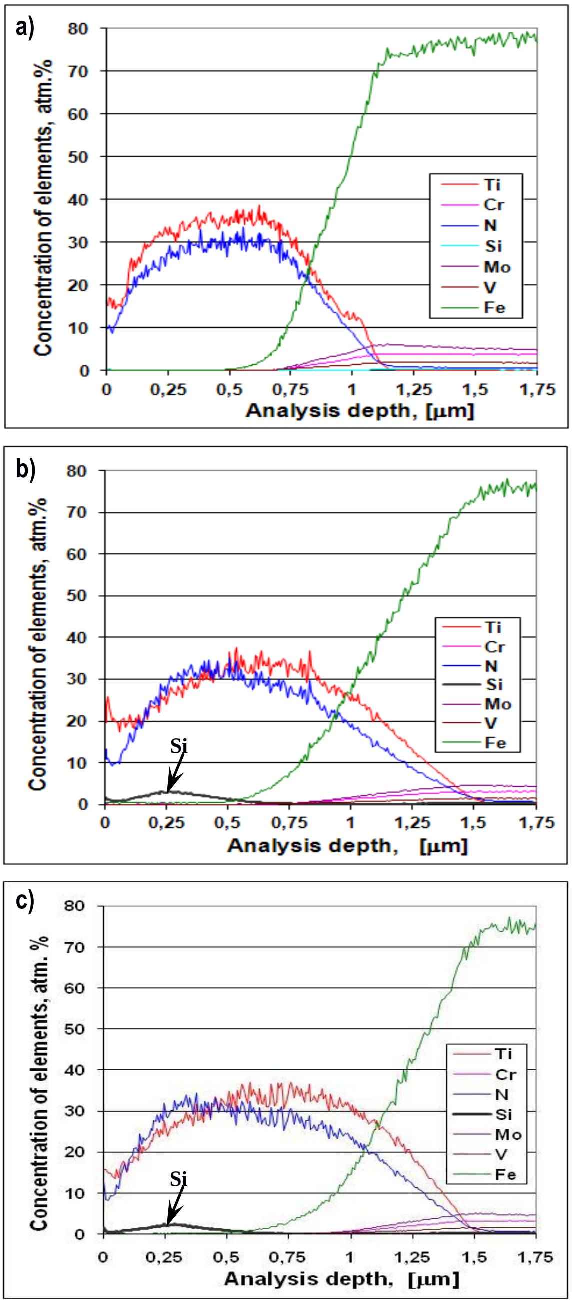

Fig. 5. The chemical composition of the TiN layer on high speed steel HS 6-5-2: a) non implanted, b) implanted with Si, c) implanted with Si+N

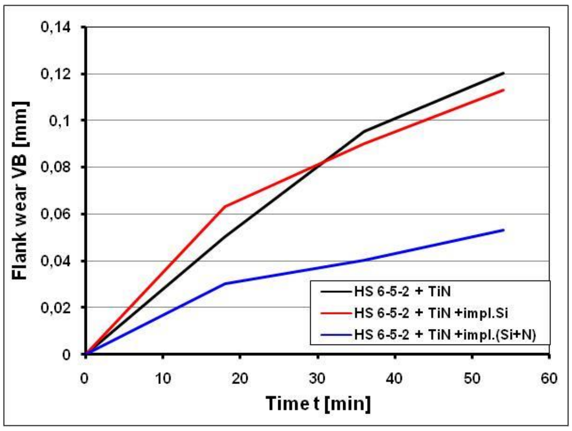

Fig. 6. The mean values flank wear during the turning of steel 40H with the use inserts HS 6-5-2 with TiN

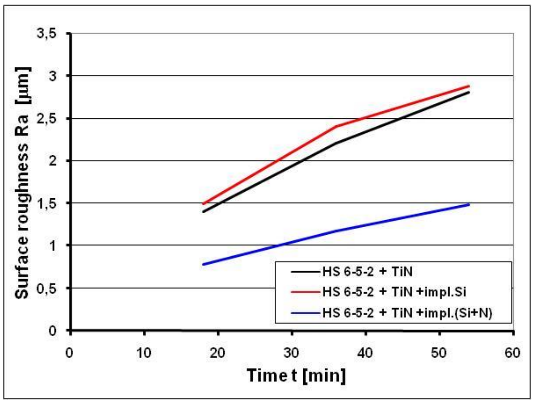

Fig. 7. Average workpiece surface roughness, Ra, during the turning of steel 40H with the use inserts HS 6-5-2 with TiN

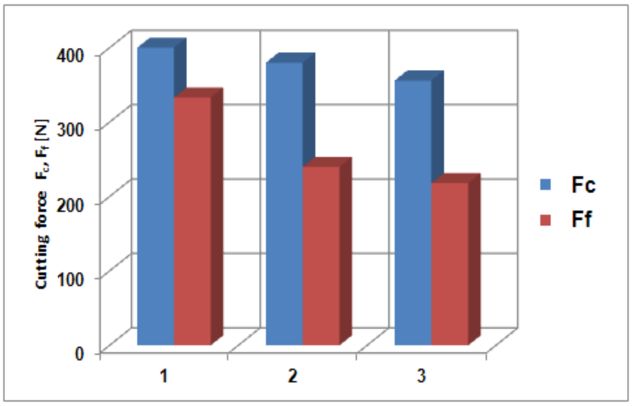

Fig. 8. The mean values cutting forces during the turning of steel 40H with the use inserts HS 6-5-2: 1 – TiN, 2 – TiN implanted Si, 3 – TiN implanted Si + N

4. CONCLUSION

Presented laboratory measurements and machining tests of the inserts made from high speed steel HS 6-5-2 with TiN coating further subjected to ion implantation with silicon and silicon plus nitrogen revealed that:

- significant decrease of the feed force Ff after the silicon and silicon plus nitrogen implantation,

- improved wear resistance on the major flank (VB) especially after the silicon plus nitrogen implantation,
- improved quality of the machined surface (Ra decrease the value to 50% after the implantation of silicon and nitrogen),
- the process of implantation of TiN coating did cause not case a significant change in the hardness of the layer.

REFERENCES

1. **Baojian L., Bin D., Ye T.** (2014), Influence of niobium ion implantation on the microstructure, mechanical and tribological properties of TiAlN/CrN nano-multilayer coatings, *Surface and Coatings Technology*, 240, 405-412.
2. **Barbaszewski T., Dąbrowski M., Drwięga M., Gawlik J., Lipińska E.** (1989), Implantation profiles of nitrogen and titanium in low energy bombarded high speed tool steel, *Physica Status Solidi (A) Applied Research*, 112(1), 347-352.
3. **Gerth J., Wiklund U**. (2008), The influence of metallic interlayers on the adhesion of PVD TiN coatings on high-speed steel, *Wear*, 264, 885-892.
4. **Grančič B., Mikula M., Roch T., Zeman P., Satrapinskyy L., Gregor M., Plecenik T., Dobrocka E., Hajovska Z., Micusik M., Satka A., Zahoran M., Plecenik A., Kúš P.** (2014), Effect of Si additional on mechanical properties and high temperature oxidation resistance of Ti-B-Si hard coatings, *Surface and Coatings Technology*, 240, 48-54.
5. **Hensel E., Sommer H., Knothe P., Richter E**. (1989), Silicon nitride layer on tool steel produced by ion beam mixing and ion beam assisted deposition, *Physica Status Solidi (A) Applied Research*, 112(2), 533 – 539.
6. **Keenan M.P., Bradbury S.R., Afzal A., Ahmed W.** (1998), Advanced surface engineering of circular saw blades for improved performance, *Surface Engineering*, 14(6), 463-468.
7. **Kieckow F., Kwietniewski C., Tentardini E.K., Reguly A., Baumvol Israel J.R**. (2006), XPS and ion scattering studies on compound formation and interfacial mixing in TiN/Ti nanolayers on plasma nitride tool steel, *Surface & Coatings Technology*, 201, 3066-3073.
8. **Lindskog P.** (1993), Recent developments in European powder metallurgy, *Powder Metallurgy International*, 25, 3, 138-142.
9. **Liu L.J., Sood D.K., Manory R.R., Zhou W.** (1995), Modification of tribomechanical properties of commercial TiN coatings by carbon ion implantation, *Surface and Coatings Technology*, 71, 159-166.
10. **Martev I.N., Dechev D.A., Ivanov N.P., Uzunov T.D., Kashchieva E.P.** (2008), Characterization and properties of highly adhesive titanium nitride and tungsten nitride thin films, Fifteenth International Summer School on Vacuum, Electron and Ion Technologies, *Journal of Physics*: Conference Series, vol. 113 (012025), 1- 4.
11. **Mikula M., Grančič B., Buršíková V., Csuba A., Držík M., Kavecký S., Plecenik A., Kúš P.** (2008), Mechanical properties of superhard TiB_2 coatings prepared by DC magnetron sputtering, *Vacuum*, 82, 278-281.
12. **Mikula M., Grančič B., Roch T., Plecenik T., Vavra I., Dobrocka E., Satka A., Buršíková V., Držík M., Zahoran M., Plecenik A., Kúš P.** (2011), The influence of low-energy ion bombardment on the microstructure development and mechanical properties of TiBx coatings, *Vacuum*, 85, 866-870.
13. **Musil J**. (2012), Hard nanocomposite coatings: Thermal stability, oxidation resistance and toughness, *Surface & Coatings Technology*, 207, 50-65.
14. **Narojczyk J., Werner Z., Piekoszewski J., Szymczyk W.** (2005), Effects of nitrogen implantation on lifetime of cutting tools made of SK5M tool steel, *Vacuum*, 78, 229-233.
15. **Perez F.J., Cristobal M.J., Hierro M.P., Pedraza F**. (1999), The influence of implanted silicon on the cyclic oxidation behaviour of two different stainless steels, *Surface and Coatings Technology*, 120-121, 442-447.
16. **Seidel F., Stock H. R., Mayr P.** (1997), Glow discharge optical spectroscopy depth profiles of ion implanted steel, titanium and titanium nitride coatings, *Thin Solid Films*, 308-309, 425-429.
17. **Shalnov K.V., Kukhta V.K., Uemura K., Ito Y.** (2011), Applications of combined ion implantation for improved tribological performance, *Surface and Coatings Technology*, 206, 849-853.
18. **Sun P.L., Hsu C.H., Liu S.H., Su C.Y., Lin C.K.** (2010), Analysis on microstructure and characteristics of TiAlN/CrN nano-multilayer films deposited by cathodic arc deposition, *Thin Solid Films*, 518, 7519-7522.
19. Toshiba Nanoanalysis Corporation. Theory of RF glow discharge optical emission spectroscopy (RF GD-OES), (2015), http://www.nanoanalysis.co.jp/en/business/case_example_93.html
20. **Yang J.H., Cheng M.F., Luo X.D., Zhang T.H.** (2007), Surface properties and microstructure of implanted TiN films using MEVVA ion source, *Materials Science & Engineering A*, 445-446, 558-562.
21. **Zhang D., Fei Q., Zhao H., Geng M., Zeng X., Chu P. K.** (2004), Low vacuum MEVVA titanium and nitogen co-ion implantation into D2 steel substrates, *Surface and Coatings Technology*, 185, 264-267.
22. **Zhang P., Cai Z., Xiong W** (2007), Influence of Si content and growth condition on the microstructure and mechanical properties of Ti-Si-N nanocomposite films, *Surface and Coatings Technology*, 201, 6819-6823.

DOI 10.1515/ama-2017-0029

RELUCTANCE NETWORK MODEL OF A PERMANENT MAGNET TUBULAR MOTOR

Andrzej WAINDOK[*], **Bronisław TOMCZUK**[*]

[*]Opole University of Technology, Department of Industrial Electrical Engineering
ul. Prószkowska 76, 45-758 Opole, Poland

a.waindok@po.opole.pl, b.tomczuk@po.opole.pl

received 10 October 2016, revised 29 July 2017 2017, accepted 16 August 2017

Abstract: The reluctance network model of a permanent magnet tubular motor (PMTM) has been presented in the paper. The reluctance values of the magnetic circuit have been calculated with using analytical expressions. The air gap reluctance has been determined with using both analytical expressions and the finite element method (FEM). Using the calculation model, the flux values coupled with the windings have been obtained and used in the calculations of force value. The calculated results have been compared with numerical and measured ones.

Keywords: Reluctance Network Method, Tubular Linear Motors, Electrodynamic Force Calculation

1. INTRODUCTION

Linear electric motors, which convert electric energy directly into mechanical thrust, have become increasingly popular in many applications, such as manufacturing automation (Gieras et al., 2011), transportation (Gieras et al., 2011), power generation, fatigue testing of materials (Tomczuk and Waindok, 2009) etc. In Fig. 1a the permanent magnet tubular motor (PMTM) has been presented (Tomczuk et al., 2012). It has been used in a drive for fatigue test stand. It is an original construction developed in Department of Electrical Engineering and Mechatronics at Opole University of Technology.

There are many various calculation methods used in the analysis of PMTM (Gieras et al., 2011; Tomczuk et al., 2012). Nowadays, FEM method is widely used (Tomczuk et al., 2007). However, it demands the knowledge of the field theory for formulation of the boundary problems and application of a computer package dedicated for the magnetic field analysis. In order to formulate some hints for design (initial values for geometry) and for evaluation of the field analysis the analytical methods are needed (Chevailler et al., 2004). In case of tubular motors an analytical approach, which applies Fourier series is commonly used (Wang and Howe, 2005; Wang et al., 1998; 2003; Amara and Barakat, 2010; Bianchi, 2000; Boroujeni et al., 2009; Gysen et al., 2011). In case of flat linear motors, beside Fourier series (Chung and Gweon, 2002), the reluctance network model (RNM) is very often used (Batdorff and Lumkes, 2009; Kazan and Onat, 2011; Okonkwo, 2006; Polinder et al., 2003; Sheikh-Glalavand et al., 2010) including the Carter coefficient (Gieras et al., 2011). In the presented paper, the RNM method is used for the calculation of tubular motor. This method is understood by all who know the solving of circuits and is available for everybody because it does not demand some commercial computer applications. The execution time for this case is relatively short, as well.

2. PHYSICAL MODEL

The picture and cross section of the analyzed linear motor have been presented in Fig. 1. The definitions of main dimensions are given in Fig. 2. The parameters of the motor are given in Tabs. 1 and 2. The presented construction has been designed for fatigue testing of materials. Thus, it have to be characterized by high reliability and good dynamic properties. In order to achieve these requirements, the moving coil construction has been developed.

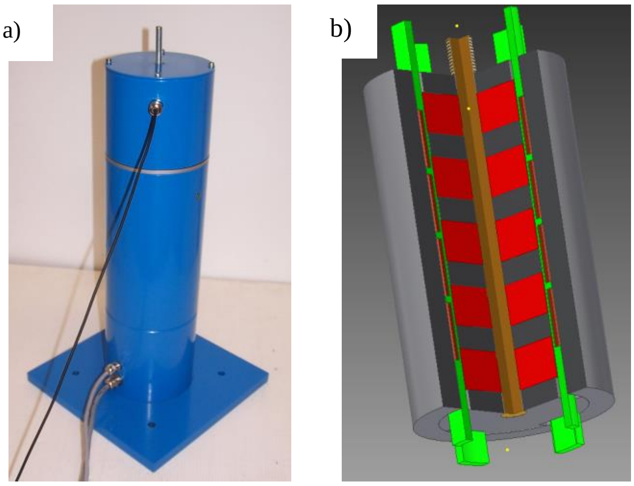

Fig. 1. a) Picture of the PMTM, b) Cross section

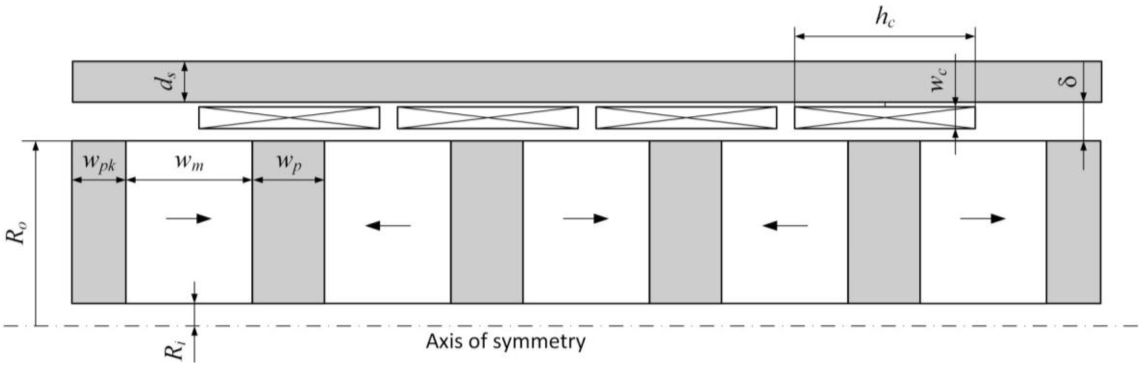

Fig. 2. Dimension symbols of the motor

Tab. 1. Dimensions of the PMTM

Dimension symbol	Value [mm]
R_i	8
R_o	40
δ	6.8
d_s	16
w_p	15
w_{pk}	13
w_m	26
w_c	4
h_c	37

Tab. 2. Main parameters of the PMTM

Parameter	Value
Nominal constant force [N]	400
Maximum force [N]	600
Nominal current [A]	2.4
Maximum current [A]	3.6
Nominal stroke [mm]	15
Nominal frequency [Hz]	50

3. RELUCTANCE NETWORK MODEL

The RNM model of the PMTM is presented in Fig. 3a. The linear properties of the steel has been assumed. In order to determine the linear magnetic permeability, the nonlinear B/H curve has been linearized (Fig. 3b). The value μ_r=434 has been assumed and used in the RNM model.

The fluxes in the motor section are given in Fig. 4. In case of steel cores and permanent magnets, the reluctance values (Fig. 3a) for such elements can be calculated using the standard expressions:

- Permanent magnet reluctance

$$R_{\mu m}=\frac{w_m}{\mu_0\mu_{rm}S_m}=\frac{0.026}{4\pi\cdot10^{-7}\cdot1.048\cdot0.004825}=4.09\cdot10^6\ \frac{1}{\text{H}} \qquad (1)$$

- Border ferromagnetic rings reluctance

$$R_{\mu1}=\frac{\ln\left(\frac{R_O+\delta+d_S/2}{R_i}\right)}{\mu_0\mu_r2\pi w_p}=\frac{\ln\left(\frac{0.04+0.0068+0.008}{0.008}\right)}{4\pi\cdot10^{-7}\cdot434\cdot2\pi\cdot0.013}=43.2\cdot10^3\ \frac{1}{\text{H}} \qquad (2)$$

- Outer stator reluctance

$$R_{\mu2}=\frac{w_m+w_p}{\mu_0\mu_rS}=\frac{0.026+0.015}{4\pi\cdot10^{-7}\cdot434\cdot0.000551}=13.6\cdot10^3\ \frac{1}{\text{H}} \qquad (3)$$

- Ferromagnetic rings reluctance

$$R_{\mu3}=\frac{\ln\left(\frac{R_O}{R_i}\right)}{\mu_0\mu_r2\pi w_p}=\frac{\ln\left(\frac{0.04}{0.008}\right)}{4\pi\cdot10^{-7}\cdot434\cdot2\pi\cdot0.015}=31.3\cdot10^3\ \frac{1}{\text{H}} \qquad (4)$$

where:

- The permanent magnet cross-section area equals the ring surface

$$S_m=\pi\cdot\left(R_o^2-R_i^2\right)=\pi\cdot\left(0.04^2-0.008^2\right)=4.825\cdot10^{-3}\ \text{m}^2 \qquad (5)$$

- Outer stator cross-section area

$$S=\pi\cdot((R_o+\delta+d_s)^2-(R_o+\delta)^2)=\pi\cdot(0.0628^2-0.0468^2)=5.509\cdot10^{-3}\ \text{m}^2 \qquad (6)$$

In the case of calculation the air gap reluctance, which is relatively long, the leakage flux lines have to be taken into account (Fig. 4). The simple expression (Fig. 2, Tab. 1)

$$R_{\mu\delta}=\frac{\ln\left(\frac{R_O+\delta}{R_O}\right)}{\mu_02\pi w_p}=\frac{\ln\left(\frac{0.04+0.0068}{0.04}\right)}{4\pi\cdot10^{-7}\cdot2\pi\cdot0.015}=1.326\cdot10^6\ \frac{1}{\text{H}} \qquad (7)$$

doesn't give the correct value, which leads to calculation errors in magnetic flux determination. Thus, some calculations of the air-gap reluctance have been carried out with using the finite element method (FEM). In Fig. 5, the simplified model of the air-gap and permanent magnet system, created in FEMM software, have been presented. It contains only two permanent magnets and one air gap. In Tab. 3 the dimensions of the model are given. In Figs. 6 and 7 the calculation results of the air gap reluctance have been presented. In case of FEM calculations both, linear (Fig. 7a) and nonlinear (Fig. 7b) magnetic materials were considered. Comparing Figs. 7a and 7b, it is visible that the properties of the steel does not influence the calculation results significantly. The differences do not exceed 1% (Fig. 8a). Due to relatively huge air gap, its reluctance calculated from expression (7) (Fig. 6) is much higher, than the real one (Fig. 7). The differences exceed 100% (Fig. 8b). Thus, a correction factor k has been introduced. Its value depends on the air gap and ferromagnetic ring dimensions (Fig. 9). In order to obtain more correct value of the reluctance, we should introduce the factor in the expression (7). After multiplication the expression (7) by this factor we obtain more precise result:

$$R_{\mu\delta k}=k\cdot R_{\mu\delta}=0.5694\cdot1.326\cdot10^6=754.8\cdot10^3\ \frac{1}{\text{H}}. \qquad (8)$$

DOI 10.1515/ama-2017-0029

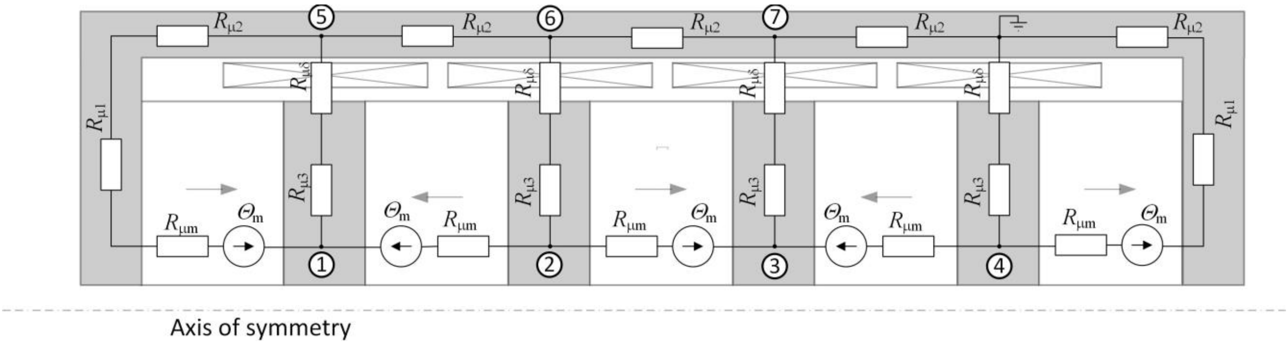

Fig. 3a. The reluctance network model of the PMTM

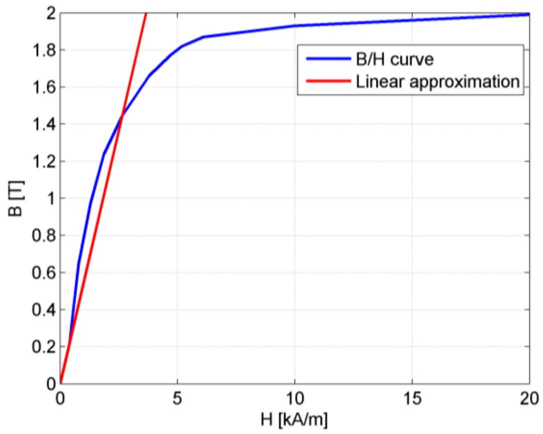

Fig. 3b. Nonlinear B/H curve of the steel

Tab. 3. Dimensions of the model in Fig. 5

Dimension	Value [mm]
w_{pk}	13
w_m	26
d_s	6
R_i	8
R_o	40
w_p	10÷20
δ	3÷10

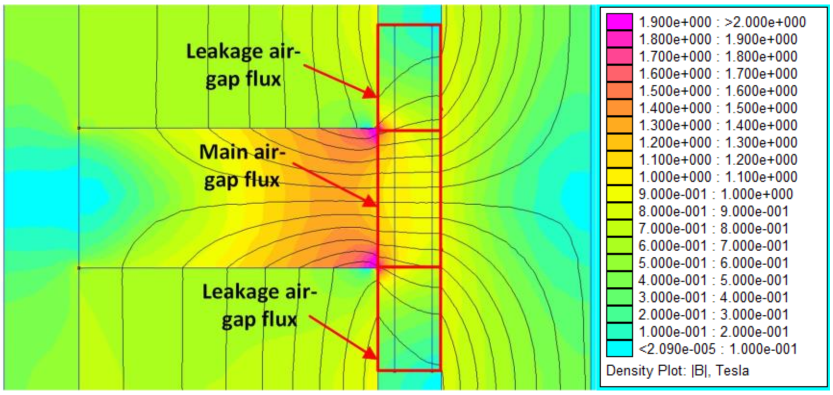

Fig. 4. Magnetic field distribution in the air gap of the PMTM

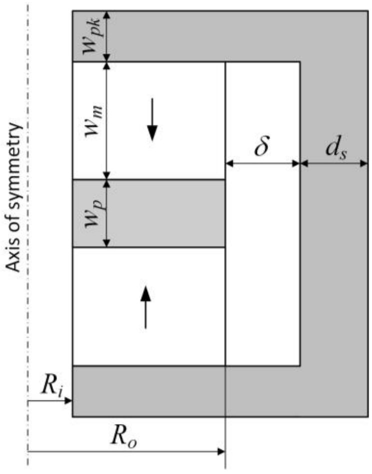

Fig. 5. Simplified model of an air-gap analyzed with using FEM

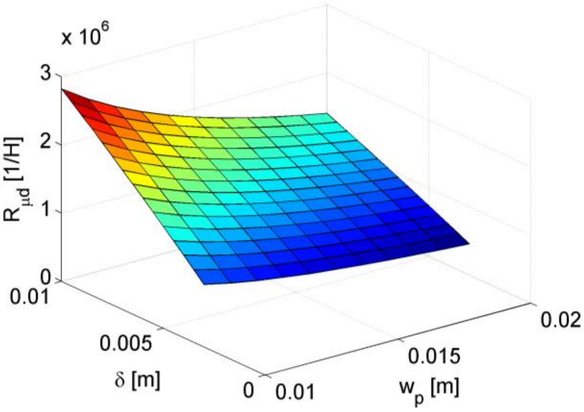

Fig. 6. Results obtained from eq. (7)

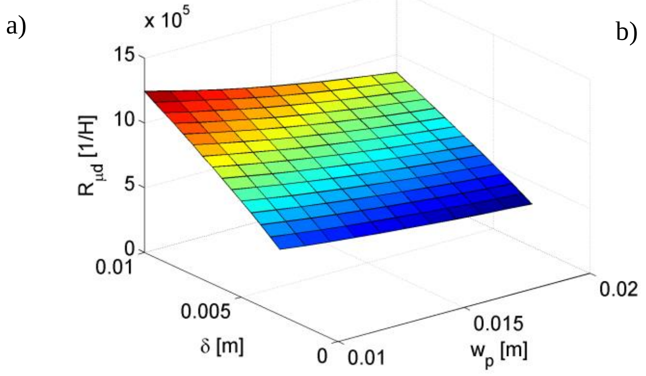

Fig. 7. Results from the FEM calculations: a) linear model, b) nonlinear model

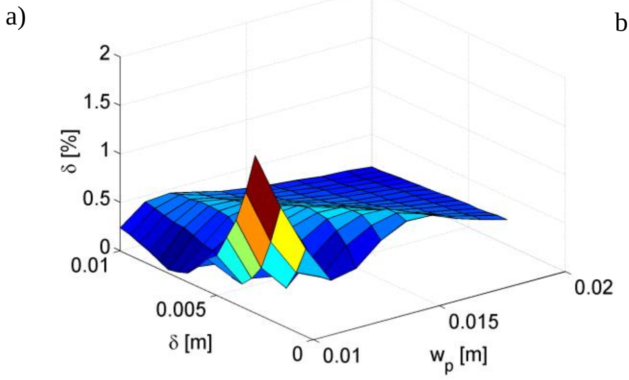

Fig. 8. Relative differences between: a) linear and nonlinear FEM models, b) nonlinear FEM and analytical models

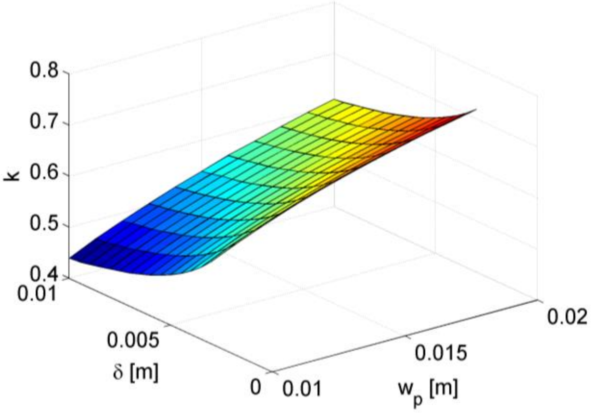

Fig. 9. Correction factor for the analytical model vs. w_p and δ dimensions

For the magnetic flux determination, we need not only the reluctance values, but also the magnetomotive forces (MMF). The MMF force of the permanent magnets can be easy calculated using their coercive force H_c:

$$\Theta_m = w_m \cdot H_c = 0.026\ [\mathrm{m}] \cdot 950000\ \left[\frac{\mathrm{A}}{\mathrm{m}}\right] = 24700\ \mathrm{A}. \tag{9}$$

Due to a small value of the MMF of the excitation winding in comparison with the permanent magnet MMF, the former one has been neglected.

Using the magnetic potential method the linear system of equations could be formulated in matrix form (Fig. 3a):

$$\begin{bmatrix} G_{11} & G_{12} & 0 & 0 & G_{15} & 0 & 0 \\ G_{21} & G_{22} & G_{23} & 0 & 0 & G_{26} & 0 \\ 0 & G_{32} & G_{33} & G_{34} & 0 & 0 & G_{37} \\ 0 & 0 & G_{43} & G_{44} & 0 & 0 & 0 \\ G_{51} & 0 & 0 & 0 & G_{55} & G_{56} & 0 \\ 0 & G_{62} & 0 & 0 & G_{65} & G_{66} & G_{67} \\ 0 & 0 & G_{73} & 0 & 0 & G_{76} & G_{77} \end{bmatrix} \cdot \begin{bmatrix} V_{\mu 1} \\ V_{\mu 2} \\ V_{\mu 3} \\ V_{\mu 4} \\ V_{\mu 5} \\ V_{\mu 6} \\ V_{\mu 7} \end{bmatrix} = \begin{bmatrix} 2\Theta_m/R_{\mu m} \\ -2\Theta_m/R_{\mu m} \\ 2\Theta_m/R_{\mu m} \\ -2\Theta_m/R_{\mu m} \\ -\Theta_m/R_{\mu m} \\ 0 \\ 0 \end{bmatrix}, \tag{10}$$

where:

$$G_{11} = G_{44} = \frac{1}{R_{\mu m}+R_{\mu 1}+R_{\mu 2}} + \frac{1}{R_{\mu 3}+R_{\mu\delta}} + \frac{1}{R_{\mu m}},$$

$$G_{22} = G_{33} = \frac{1}{R_{\mu 3}+R_{\mu\delta}} + \frac{2}{R_{\mu m}},$$

$$G_{55} = \frac{1}{R_{\mu m}+R_{\mu 1}+R_{\mu 2}} + \frac{1}{R_{\mu 3}+R_{\mu\delta}} + \frac{1}{R_{\mu 2}},$$

$$G_{66} = G_{77} = \frac{1}{R_{\mu 3}+R_{\mu\delta}} + \frac{2}{R_{\mu 2}},$$

$$G_{12} = G_{21} = G_{23} = G_{32} = G_{34} = G_{43} = -\frac{1}{R_{\mu m}},$$

$$G_{15} = G_{51} = -\frac{1}{R_{\mu m}+R_{\mu 1}+R_{\mu 2}} - \frac{1}{R_{\mu 3}+R_{\mu\delta}},$$

$$G_{26} = G_{62} = G_{37} = G_{73} = -\frac{1}{R_{\mu3}+R_{\mu\delta}},$$

$$G_{56} = G_{65} = G_{67} = G_{76} = -\frac{1}{R_{\mu2}}.$$

After solution of the system above, the magnetic potential values in the nodes of the circuit in Fig. 3a were obtained. They are used for calculation of the fluxes in the motor magnetic circuit.

The electrodynamic force could be calculated from the simple expression:

$$F = BIl. \tag{11}$$

However, in our case it is difficult to including the magnetic flux density values by points. Thus we have used more proper and convenient expression with the total magnetic flux value

$$F = \Phi\frac{IN}{h_c}. \tag{12}$$

In Fig. 10, the magnetic force values vs. the current intensity values, are presented. The results from linear RNM have been compared with the results from the finite element analysis and from the measurement results. A very good conformity between measurements and RNM calculation results is observed. The results from FEM method with nonlinear B/H characteristic differ a little bit more from measurement values. However, the differences are not significant (less than 7%).

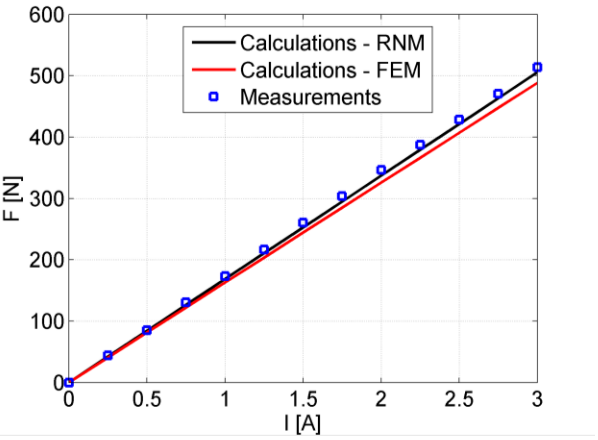

Fig. 10. Magnetic force vs. current value

4. CONCLUSIONS

In many cases, when we are designing an electromagnetic device with relatively big air gaps the magnetic reluctances can be calculated with analytical expressions. When the gaps are very small and the magnetic circuit shape is complicated the finite element method (FEM) should be used. Thus, in many cases the analytical models are a good alternative to the numerical ones. They are characterized by very short calculation time, under acceptable accuracy.

Of all the analytical methods, the reluctance network method (RNM) is easiest and simplest. For the presented PMTM calculations, it has only one disadvantage – the proper determination of the air-gap reluctance is quite difficult. It influences the results significantly. In the presented case of TLM (tubular linear motor) with relatively large air-gap, there is no correction coefficient (in the literature) for analytical calculation of the reluctance. In the paper, the FEM method has been used for determination of the correction coefficient.

Using the calculation model, the flux values coupled with the windings have been obtained and used in the calculations of the force value. The calculated results have been compared with numerical and measured ones. The measurement validation of the presented method confirms its correctness.

REFERENCES

1. **Amara Y., Barakat G.** (2010), Analytical modeling of magnetic field in surface mounted permanent-magnet tubular linear machines, *IEEE Trans. on Magnetics*, 46, 3870-3884.
2. **Batdorff M.A., Lumkes J.H.** (2009), High-fidelity magnetic equivalent circuit model for an axisymmetric electromagnetic actuator, *IEEE Trans. on Magnetics*, 45, 3064-3072.
3. **Bianchi N.** (2000), Analytical field computation of a tubular permanent-magnet linear motor, *IEEE Trans. on Magnetics*, 36, 3798-3801.
4. **Boroujeni S.T., Milimonfared J., Ashabani M.** (2009), Design, prototyping and analysis of a novel tubular permanent-magnet linear machine, *IEEE Trans. on Magnetics*, 45, 5405-5413.
5. **Chevailler S., Markovic M., Jufer M., Perriard Y.** (2004), Linear motor optimization using an analytical model, *ICEM*, Cracow, Poland, 5-8 September, paper no 311 (on conference CD).
6. **Chung M.J., Gweon D.G.** (2002), Modeling of the armature slotting effects in the magnetic field distribution of a linear permanent magnet motor, *Electrical Engineering*, 84, 101-108.
7. **Gieras J.F., Piech Z.J., Tomczuk B.** (2011), *Linear synchronous motors*, CRC Press, Taylor & Francis Group, USA.
8. **Gysen B.L.J., Meessen K.J., Paulides J.J.H., Lomonova E.A.** (2011), 3-D analytical and numerical modeling of tubular actuators with skewed permanent magnets, *IEEE Trans. on Magnetics*, 47, 2200-2212.
9. **Kazan E., Onat A.** (2011), Modeling of air core permanent-magnet linear motors with a simplified nonlinear magnetic analysis, *IEEE Trans. on Magnetics*, 47, 1753-1762.
10. **Okonkwo R.C.** (2006), Design and performance of permanent-magnet DC linear motors, *IEEE Trans. on Magnetics*, 42, 2179-2183.
11. **Polinder H., Slootweg J.G., Hoeijmakers M.J., Compter J.C.** (2003), Modeling of a linear PM machine including magnetic saturation and end effects: maximum force-to-current ratio, *IEEE Trans. on Magnetics*, 39, 1681-1688.
12. **Sheikh-Ghalavand B., Vaez-Zadeh S., Hassanpour Isfahani A.** (2010), An improved magnetic equivalent circuit model for iron-core linear permanent-magnet synchronous motors, *IEEE Trans. on Magnetics*, 46, 112-120.
13. **Tomczuk B., Schröder G., Waindok A.** (2007), Finite element analysis of the magnetic field and electromechanical parameters calculation for a slotted permanent magnet tubular linear motor, *IEEE Trans. on Magnetics*, 43, 3229-3236.
14. **Tomczuk B., Waindok A.** (2009), Tubular linear actuator as a part of mechatronic system, *Solid State Phenomena*, 147-149, 173-178.
15. **Tomczuk B., Waindok A., Wajnert D.** (2012), Transients in the electromagnetic actuator with the controlled supplier, *Journal of Vibroengineering*, 14, 39-44.
16. **Wang J., Howe D.** (2005), Tubular modular permanent-magnet machines equipped with quasi-Halbach magnetized magnets – Part I: magnetic field distribution, EMF, and thrust force, *IEEE Trans. on Magnetics*, 41, 2470-2478.
17. **Wang J., Howe D., Jewell G.W.** (2003), Fringing in tubular permanent-magnet machines: Part II. Cogging force and its minimization, *IEEE Trans. on Magnetics*, 39, 3517-3522.
18. **Wang J., Jewell G.W., Howe D.** (1998), A general framework for the analysis and design of tubular linear permanent magnet machines, *IEEE Trans. on Magnetics*, 35, 1986-1999.

DE GRUYTER
OPEN

DOI 10.1515/ama-2017-0030

MINIMAL KINEMATIC BOUNDARY CONDITIONS FOR COMPUTATIONAL HOMOGENIZATION OF THE PERMEABILITY COEFFICIENT

Marek WOJCIECHOWSKI[*]

[*]Technical University of Lodz, Department of Civil Engineering, Architecture and Environmental Engineering,
Chair of Geotechnics and Engineering Structures, Al. Politechniki 6, 90-924 Łódź, Poland

mwojc@p.lodz.pl

received 16 March 2016, revised 15 September 2017, accepted 18 September 2017

Abstract: In the paper, computational homogenization approach is used for recognizing the macroscopic permeability from the microscopic representative volume element (RVE). Flow of water, at both macro and micro level, is assumed to be ruled by Darcy law. A special averaging constraint is used for numerical flow analysis in RVE, which allows to apply macroscopic pressure gradient without the necessity to use directly Dirichlet or Neumann boundary conditions. This approach allows arbitrarily shaped representative volumes and eliminates undesirable boundary effects. Generated effective permeability takes into account the structuring effects, what is an advantage over other homogenization methods, like self-consistent one.

Key words: Computational Homogenization, Permeability, RVE, Minimal Kinematic Boundary Conditions

1. INTRODUCTION

In broad class of disordered porous materials with clear matrix-inclusions internal structure, the flow of fluid can be described by Darcy equation at both, micro and macro level. This is for example the case of concrete and sand-clay soils. In order to determine the macroscopic response with accurate account for microstructural characteristics and evolution, computational homogenization strategy can be exploited (see Geers et al., 2001, Feyel, 2003; Kousnietsova et al., 2010). When using this micro - macro strategy there is actually no necessity to define homogenized macroscopic constitutive equations. Instead, the constitutive behavior at macroscopic integration points is determined by averaging the response of the deforming microstructure. This enables a straightforward application of the method to geometrically and physically non-linear problems, making it a particularly valuable tool for the modeling of evolving non-linear heterogeneous microstructures under complex macroscopic loading paths.

Computational homogenization needs, at each macroscopic integration point, a microscopic representative volume to be defined and boundary value problem (BVP) to be solved. One of the concerns in homogenization theory is the kind of boundary conditions (BCs) which should be applied to this BVP. Recently, new concept in this area has been proposed, called minimal kinematic boundary conditions (see Mesarovic S.D. and Padbidri J., 2005; Inglis at al., 2008; Wojciechowski M. and Lefik M., 2016). This approach consists in applying special averaging constraint to the microscopic problem, instead of usual Dirichlet or Neumann boundary conditions. This allows for arbitrary shapes of RVE and eliminates undesirable boundary effects which may appear when e.g. periodic BCs are applied.

In the paper we use the computational approach for recognizing the macroscopic permeability from the microscopic representative volume element (RVE), which takes into account proportions, arrangement and shape of the material constituents. In the following, the homogenization scheme is formulated, the solution by finite element method is presented and the illustrative example is shown. Paper ends with some discussion and conclusions.

2. HOMOGENIZATION FRAMEWORK

Let's consider microstructurally complex porous material for which a representative volume element (RVE) Ω can be defined. In case of laminar flow, local flux u_i in the RVE is given by Darcy equation (skipping source terms):

$$u_i = -\frac{k_{ij}}{\gamma} p_{,j} \tag{1}$$

where $p_{,j}$: is a pressure gradient, k_{ij} is a permeability tensor depending on the position in RVE (in velocity units) and γ is a specific weight of the fluid. Averages of the microscopic fluxes and pressure gradients over domain Ω are given by:

$$P_{,j} = \frac{1}{\Omega}\int_{\Omega} p_{,j} d\Omega, \tag{2}$$

$$U_i = \frac{1}{\Omega}\int_{\Omega} u_i d\Omega. \tag{3}$$

These values are assumed to be related via the *effective permeability tensor* K_{ij}, such that:

$$U_i = -\frac{K_{ij}}{\gamma} P_{,j}. \tag{4}$$

The above equation describes macroscopic behavior of the composite. The fundamental concept from which the existence and consistency of the above averages can be derived is the Hill macrohomogeneity condition (Hill, 1965), which in case of Darcy flow is written as (Du X. and Ostoja-Starzewski M., 2006):

$$\int_{\Omega} u_i p_{,i} d\Omega = \frac{1}{\Omega}\int_{\Omega} u_i d\Omega \int_{\Omega} p_{,i} d\Omega. \tag{5}$$

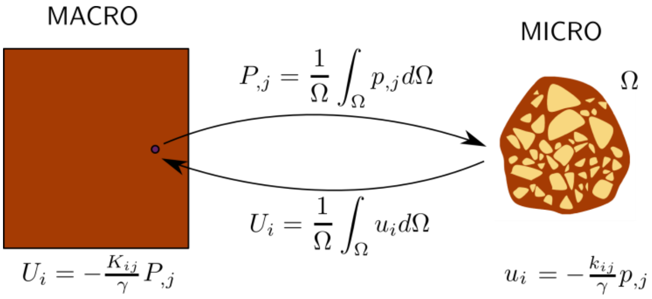

Fig. 1. Scheme of the computational homogenization for Dacy flow

Homogenization problem considered here is formulated as follows: find solution p of the compatibility equation $u_{i,i} = 0$ defined on Ω, subject to some macroscopic pressure gradient $P_{,j}$ in such a way that equation (2) is fulfilled. From this solution microscopic u_i and macroscopic U_i and K_{ij} are then derived (see Figure 1 for homogenization scheme). The above can be viewed as a problem of minimization of total potential energy (see again Du X. and Ostoja-Starzewski M., 2006) with additional averaging constraint:

$$\min_p \left[\int_{\Omega} -p_{,i}\frac{k_{ij}}{\gamma}p_{,j}\, d\Omega\right] \quad \text{subject to} \qquad \tag{6}$$
$$-\Omega P_{,k} + \int_{\Omega} p_{,k} d\Omega = 0$$

which can be converted to unconstrained minimization by means of Lagrange multipliers λ_k (Bertsekas, 1982):

$$\min_p \left[\int_{\Omega} -p_{,i}\frac{k_{ij}}{\gamma}p_{,j}\, d\Omega + \lambda_k\left(-\Omega P_{,k} + \int_{\Omega} p_{,k} d\Omega\right)\right]. \tag{7}$$

3. FINITE ELEMENT METHOD FORMULATION

Solutions p of the above homogenization problem have to belong to the Sobolev functional space $H^1(\Omega)$ (at least), and this is assured by piecewise polynomial base functions used in FEM discretizations (see e.g. Babuška I. and Strouboulis T., 2001; Brenner S.C. and Scott R., 2007). Let's assume the domain Ω is discretized into $e = 1, \dots, E$ elements such that $\Omega = \Omega_1 \cup \dots \cup \Omega_E = \sum_e \Omega_e$. Let's assume also, that each element has $n = 1, \dots, N$ nodes in which the solution will be known. Pressures and its spatial derivatives inside elements are then given by linear combinations:

$$p_e(\mathbf{x}) = \phi_{en}(\mathbf{x})\, p_{en},$$
$$p_{e,i}(\mathbf{x}) = \phi_{en,i}(\mathbf{x})\, p_{en} \tag{8}$$

where: p_{en} are the nodal pressures and $\phi_{en}(\mathbf{x})$ are element interpolation functions defined on global Cartesian coordinates. For numerical integration pressure values at Gauss points inside elements need to be known. If number of these points per element is marked as $g = 1, \dots, G$, then arrays of pressures and their derivatives for the discretized domain are written as:

$$p_{eg} = \phi_{egn} p_{en},$$
$$p_{egi} = \phi_{egni} p_{en} \tag{9}$$

where: ϕ_{egn}, ϕ_{egni} are appropriate arrays of interpolation functions and their derivatives. Minimization problem (7) can be now rewritten with discretized pressure field, replacing integrals with sums over elements and integration points:

$$\min_p \left[\sum_e p_{em}\left(-\sum_g w_{eg}\phi_{egmi}\frac{k_{egij}}{\gamma}\phi_{egnj}\right)p_{en} + \lambda_k\left(-\Omega P_{,k} + \sum_e\sum_g \phi_{egnk} p_{en}\right)\right] =$$
$$\min_p \left[\sum_e p_{em} A_{emn} p_{en} + \lambda_k\left(-\Omega P_{,k} + \sum_e B_{enk} p_{en}\right)\right] \tag{10}$$

where: k_{egij} is an array of permeability tensors at Gauss points and w_{eg} are weights of numerical integration. Moving from Einstein notation to the usual matrix representation of the finite element interpolations give us:

$$\min_{\mathbf{p}} \left[\sum_e \mathbf{p}_e^{\mathrm{T}} \mathbf{A}_e \mathbf{p}_e + \boldsymbol{\lambda}^{\mathrm{T}}\left(-\Omega\mathbf{P} + \sum_e \mathbf{B}_e^{\mathrm{T}}\mathbf{p}_e\right)\right]. \tag{11}$$

Finally, dropping the sum over elements (i.e. performing global assembling) we get:

$$\min_{\mathbf{p}}[\mathbf{p}^{\mathrm{T}}\mathbf{A}\mathbf{p} + \boldsymbol{\lambda}^{\mathrm{T}}(-\Omega\mathbf{P} + \mathbf{B}^{\mathrm{T}}\mathbf{p})] = \min_{\mathbf{p}}[\Pi(\mathbf{p}, \boldsymbol{\lambda})] \tag{12}$$

where: $\mathbf{p}$ is global vector of unknown pressures of the length M (M - total number of nodes in discretization), $\mathbf{A}$ is a global linear operator of the size $M \times M$, $\mathbf{B}$ is a problem specific matrix of the size $M \times D$ (D - space dimension: 2 or 3), $\boldsymbol{\lambda}$ is a vector of unknown Lagrange multipliers of the length D, and $\mathbf{P}$ is a vector of known, macroscopic pressure gradient to be applied, also of length D. Solution of the problem is found by differentiation of the resulting potential Π with respect to unknown $\mathbf{p}$ and $\boldsymbol{\lambda}$ and equating derivatives to 0:

$$\frac{\partial\Pi(\mathbf{p}, \boldsymbol{\lambda})}{\partial\mathbf{p}} = \mathbf{A}\mathbf{p} + \mathbf{B}\boldsymbol{\lambda} = \mathbf{0}, \tag{13}$$

$$\frac{\partial\Pi(\mathbf{p}, \boldsymbol{\lambda})}{\partial\boldsymbol{\lambda}} = \mathbf{B}^{\mathrm{T}}\mathbf{p} - \Omega\mathbf{P} = \mathbf{0}. \tag{14}$$

The above is a system of linear equations:

$$\begin{bmatrix}\mathbf{A} & \mathbf{B}\\ \mathbf{B}^{\mathrm{T}} & \mathbf{0}\end{bmatrix}\begin{bmatrix}\mathbf{p}\\ \boldsymbol{\lambda}\end{bmatrix} = \begin{bmatrix}\mathbf{0}\\ \Omega\mathbf{P}\end{bmatrix}. \tag{15}$$

For this problem only minimal set of Dirichlet boundary conditions should be applied, without introducing any additional pressure gradient and flux. This is achieved simply by fixing pressure at certain level: $p = p_0$ at single, arbitrary boundary point of the domain (or at arbitrary boundary node of its discretization).

Macroscopic, effective permeability can be now calculated from the observation, that Lagrange multipliers $\boldsymbol{\lambda}$ have interpreta-

DOI 10.1515/ama-2017-0030

tion of macroscopic average flux, with minus sign, i.e.: $\boldsymbol{\lambda} = -\mathbf{U}$ (see Wojciechowski M. and Lefik M., 2016). Combining equations (13) and (14) give us then:

$$\Omega \mathbf{P} = (\mathbf{B}^{\mathrm{T}} \mathbf{A}^{-1} \mathbf{B}) \mathbf{U}, \quad \mathbf{U} = \Omega (\mathbf{B}^{\mathrm{T}} \mathbf{A}^{-1} \mathbf{B})^{-1} \mathbf{P} \tag{16}$$

and from equation (4) we get finally the effective permeability:

$$K_{ij} = \mathbf{K} = -\gamma \Omega (\mathbf{B}^{\mathrm{T}} \mathbf{A}^{-1} \mathbf{B})^{-1}. \tag{17}$$

One should note that there is no direct dependence between effective permeability and macroscopic pressure gradient, thus the same result will be obtained for any $P_{,j}$. This means that explicit solution of the system of linear equations (15) is actually not needed. This will be true unless microscopic constitutive equation is nonlinear, i.e. unless operator $\mathbf{A}$ is pressure dependent. In addition one can observe, that equation (17) needs a kind of inversion of the operator $\mathbf{A}$ which might be costly for large number of the RVE discretization nodes (or even impossible). However, in these cases numerical differentiation can be used.

4. NUMERICAL EXAMPLE

Presented homogenization method for Darcy flow has been implemented in the frame of finite element package *fempy* (Wojciechowski, 2014). We performed calculations for exemplary two-dimensional representative volume of the sand-clay mixture (for permeability properties of such materials see e.g. Juang and Holtz, 1986; Chapuis, 1990; Revil and Cathles, 1999; Kacprzak, 2006; Boutin et al., 2011). RVE of the reference size about 5 mm is considered, with irregular boundary adjusted to the randomly generated grain distribution (see figure 2). Average particle size diameter has been chosen uniformly, in a random way, from the range 0.1 - 1 mm. The shape of sand grains is also irregular. Volume ratio of grains is assumed to be equal to $G = 0.4$. Sand grains are assumed to be impermeable. Matrix consists in saturated kaolin clay with the void ratio $e_c = 1$. Following the results reported by Kacprzak (2006) and Boutin et al. (2011) (see e.g. paragraph 4.4 in this second reference) the permeability tensor for such clay paste is taken as $k_c = \left[[10^{-9}, 0], [0, 10^{-9}]\right] \mathrm{m/s}$. Also, specific weight for water $\gamma = 9.807\ \mathrm{kN/m^3}$ is taken for calculations.

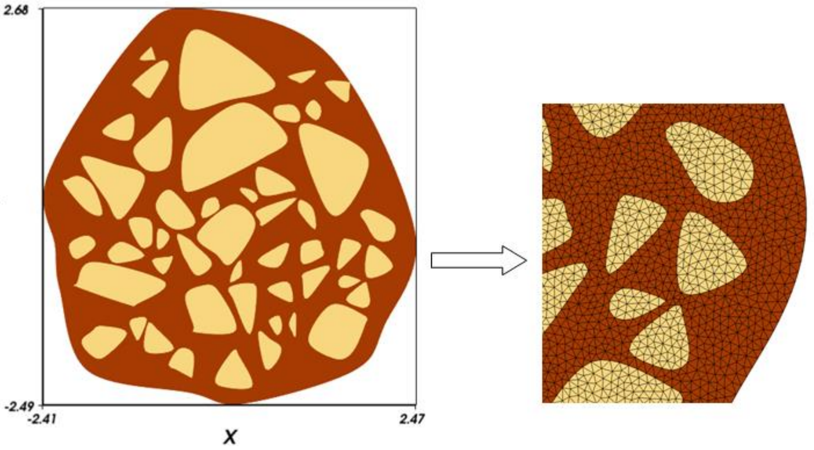

Fig. 2. Geometry of the representative volume element (dimensions in millimeters) and part of finite element discretization

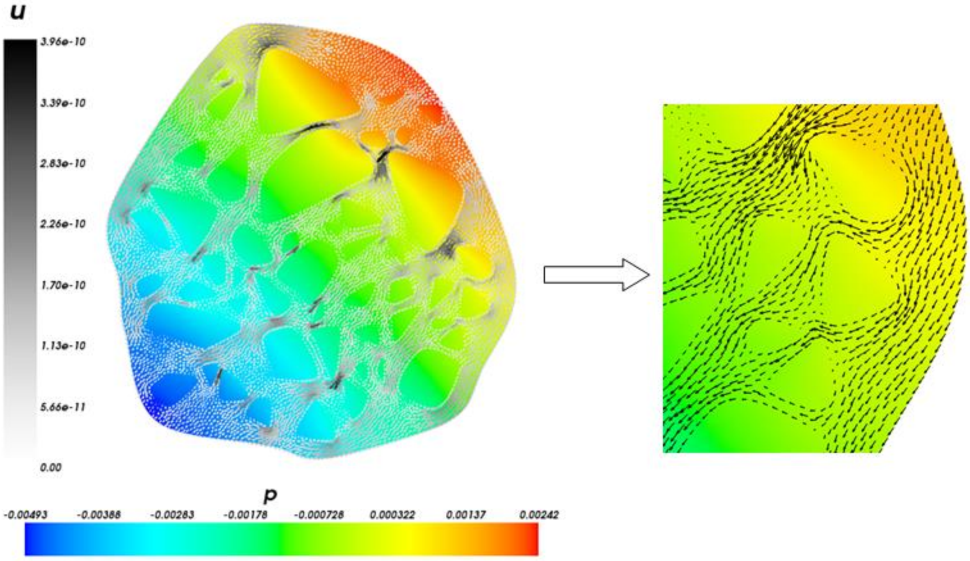

Fig. 3. Pressures *p* [kPa] and Darcy flux *u* [m/s] distribution inside the RVE after application of macroscopic pressure gradient. On the right hand side: zoom on the flux vectors.

Geometry of the RVE has been discretized into 3-noded, triangular, linear finite elements. Very fine discretization (10647 nodes, 21003 elements) is used for better handling grain shapes, but also coarser mesh should provide acceptable results (it was not tested though). In this example the reference pressure has been taken as $p_0 = 0\,\mathrm{kPa}$ at single boundary point of the discretization, and the macroscopic pressure gradient of the value $P_{,j} = [1, 1]\,\mathrm{kPa/m}$ is applied.

Results of the calculations are showed in Fig. 3. The flow occurs from top-right to bottom-left of the RVE, reflecting the applied macroscopic pressure gradient. The flux is zero inside the sand grains and varies in clay matrix taking the largest values in "bottlenecks" between grains. From this solution the macroscopic average flux is established from (3) as: $\mathrm{U_i} = [-3.74 \cdot 10^{-11}, -3.72 \cdot 10^{-11}]\,\mathrm{m/s}$. Also the homogenized, macroscopic permeability tensor calculated from equation (17) is equal to:

$$\mathrm{K_{ij}} = \begin{bmatrix} 3.69 \cdot 10^{-10} & -3.22 \cdot 10^{-12} \\ -3.22 \cdot 10^{-12} & 3.68 \cdot 10^{-10} \end{bmatrix} \mathrm{m/s}.$$

It's straightforward to verify, that equation (4) holds for these results.

5. DISCUSSION OF RESULTS

Macroscopic permeability obtained in numerical example is generally anisotropic, but it is almost equal in both Cartesian directions, i.e. $K = K_{11} \cong K_{22} \cong 3.7 \cdot 10^{-10}\,\mathrm{m/s}$. This indicates that the randomly generated RVE is appropriate for the considered problem – statistically isotropic at macroscale. The difference between K_{11} and K_{22}, and also the small skew component K_{12} should then tend to zero with increasing size of RVE. Comparisons to the oedometric laboratory tests reported by Kacprzak (2006) and Boutin et al. (2011) show, that computed permeability K falls, as expected, into the range of variation of experimental results performed for similar volume ratio of sand grains and void ratio of clay paste.

Computational approach provides generally better approximation of the mixture permeability than simplified analytical methods. Self-consistent homogenization scheme for 2D case gives effective filtration coefficient equal to:

$$K_{S-C} = k_c \cdot \frac{1 - G}{1 + G}. \tag{18}$$

Exactly the same result will arise also from Mori-Tanaka homogenization scheme. For the parameters used in numerical example the above equation gives coefficient $K_{S-C} = 4.3 \cdot 10^{-10}\,\mathrm{m/s}$, which is larger than numerically obtained K. This could be explained by the fact, that the structuring effects, i.e. irregular, elongated paths of water flow through the RVE, visible in figure 3, have been automatically taken into account in computational results, which is not the case in analytical result. One should note that the proposed numerical approach will produce reliable effective parameters for any G and k_c, also if these parameters vary both at microscopic and macroscopic level. Conversely, in case of the mentioned analytical self-consistent method special extensions with additional grain distribution and concentration parameters have to be considered, in order to catch microscopic structuring effects (see e.g. Boutin, 2011).

6. CONCLUSIONS

Computational homogenization approach is an attractive method for dealing with Darcy flow in heterogeneous porous media. This is because of the possibility of taking into account local proportions, arrangements, shapes and permeability parameters of composite constituents. At every integration point of macroscopic problem such locally defined representative volume elements can be loaded with local macroscopic pressure gradients, in an average sense, to get the macroscopic flux vectors. In general, effective macroscopic permeability is actually not necessary to be explicitly established in this approach. However, as we have showed, obtaining it is quite straightforward and reliable. In numerical example, the obtained effective permeability takes into account the structuring effects in the sand-clay mixture and this is an advantage in comparison to other homogenization methods.

In this paper only an illustrative example of single RVE analysis is presented, without actual macroscopic problem, as the main goal was presentation of the computational approach. Also, no special analysis is performed for establishing the adequate size and discretization of the RVE. Instead we relied on large representative volume with fine finite elements. It should be emphasized, that the shape of RVE used in this paper is rather unusual in numerical homogenization, where square or box shapes are commonly used, for easy application of linear or periodic kinematic BCs (pressure gradients in this case). Irregular shape of RVE is possible thanks to the novel method of application of macroscopic pressure gradient. The influence of RVE shape on homogenization results is however an open topic and should be addressed in future works.

REFERENCES

1. **Babuška I., Strouboulis T.** (2001), *The finite element method and its reliability*, Clarendon Press, Oxford.
2. **Bertsekas D.P.** (1982), *Constrained optimization and Lagrange multiplier methods*, Athena Scientific, Belmont, Massachusetts.
3. **Boutin C., Kacprzak G., Thiep D.** (2011), Compressibility and permeability of sand–kaolin mixtures. Experiments versus non-linear homogenization schemes, *International Journal for Numerical and Analytical Methods in Geomechanics*, 35(1), 21-52.
4. **Brenner S.C., Scott R.** (2007), *The mathematical theory of finite element methods* (Vol. 15), Springer Science & Business Media.
5. **Chapuis R.P.** (1990), Sand-bentonite liners: predicting permeability from laboratory tests, *Canadian Geotechnical Journal*, 27(1), 47-57.
6. **Du X., Ostoja-Starzewski M.** (2006), On the size of representative volume element for Darcy law in random media, in *Proceedings of the Royal Society A: Mathematical, Physical and Engineering Science*, 462(2074), 2949-2963, The Royal Society.
7. **Feyel F.** (2003), A multilevel finite element method (FE 2) to describe the response of highly non-linear structures using generalized continua, *Computer Methods in Applied Mechanics and Engineering*, 192(28), 3233-3244.
8. **Geers M.G.D., Kouznetsova V.G., Brekelmans W.A.M.** (2001), Gradient-enhanced computational homogenization for the micro-macro scale transition, *Le Journal de Physique IV*, 11(PR5), Pr5-145.
9. **Hill R.** (1965), Continuum micro-mechanics of elastoplastic polycrystals, *Journal of the Mechanics and Physics of Solids*, 13(2), 89-101.
10. **Inglis H.M., Geubelle P.H., Matouš K.** (2008), Boundary condition effects on multiscale analysis of damage localization, *Philosophical Magazine*, 88(16), 2373-2397.

11. **Juang, C.H., Holtz R.D.** (1986), Fabric, pore size distribution, and permeability of sandy soils, *Journal of Geotechnical Engineering*, 112(9), 855-868.
12. **Kacprzak G.** (2006), *Etude du comportement mécanique des mélanges sable/argile*, PhD ENTPE/INSA, Lyon.
13. **Kouznetsova V.G., Geers M.G.D., Brekelmans W.A.M**. (2010), Computational homogenisation for non-linear heterogeneous solids, *Multiscale Modeling in Solid Mechanics: Computational Approaches*, 3, 1-42.
14. **Mesarovic S.D., Padbidri J.** (2005), Minimal kinematic boundary conditions for simulations of disordered microstructures, *Philosophical Magazine*, 85(1), 65-78.
15. **Revil A., Cathles L.M.** (1999), Permeability of shaly sands, *Water Resources Research*, 35(3), 651-662.
16. **Wojciechowski M.** (2014) Fempy – finite element method in python, *http://fempy.org, http://geotech.p.lodz.pl:5080/fempy*, last access: August 2017.
17. **Wojciechowski M**., **Lefik M.** (2016), On the static nature of minimal kinematic boundary conditions, *Engineering Transactions*, 64(4), 581-587.

DOI 10.1515/ama-2017-0031

INCREASING OF ENERGY EFFICIENCY OF SPINDLES WITH FLUID BEARINGS

Dmytro FEDORYNENKO*, **Serhii SAPON***, **Sergiy BOYKO***, **Anastasiia URLINA***

*Chernihiv National University of Technology, Mechanical Engineering Department, 95 Shevchenko Street, Chernihiv, Ukraine

fdy1974@gmail.com, s.sapon@gmail.com, svboyko.cstu@gmail.com, urlina.anastasia@gmail.com

received 5 October 2015, revised 15 September 2017, accepted 18 September 2017

Abstract: Promising ways of energy efficiency gain of spindles with fluid flow bearings are offered. New design of journal hybrid flow bearing which contains spherical bearing pockets and adjustable valves with relay control system is offered to improve energy efficiency of spindle units of machine tools. To reduce power losses of fluid bearings at high speed special lubrication based on water with integrated system of corrosion protection is offered. Results of theoretical research of energy consumption of grinding machine tool with a new design of spindle hybrid bearings are presented. Power losses of the spindle unit with both new design and base design of journal bearings are assessed. Effectiveness of new design of spindle hybrid bearings at high operating speeds is shown.

Keywords: Energy Efficiency, Power Losses, Hybrid Fluid Bearing, Spindle, Machine Tool, Low Viscosity Lubrication, Corrosion Protection

1. INTRODUCTION

According to the data of the works (Diaz et al., 2011; Estomad Project, 2013) great influence on current consumption in the course of processing is made by a spindle drive (about 30 %) and auxiliary machine tool units (to 60 % from general expenses on electric power). At the same place, it is specified that power consumption by a spindle unit and power consumption for lubricant oil inlet for its lubrication and cooling vary in the range from 50-70 % depending on processing conditions on CNC machine. Energy efficiency of main motion drive will decrease if it works below rated power. On the other hand, maximum allowed power of spindle limits the speed of cutting and productivity of machining process.

Energy efficiency indicators of a spindle unit are mostly provided with a correct choice of type and design of its bearings (Cao et al., 2017). Fluid film bearings provide high rotational accuracy and high indicators of stiffness and damping compared with other types of spindle arrangements. However, at use of viscous lubricant oils as operating liquids hydrostatic bearings are characterized by big losses of capacity on friction and, as a consequence, vigorous heating at increased rotational frequencies (Perovic, 2012; Wardle, 2015). For example, at high-speed cutting on lathes it is established that at rotational frequency of 8000 rpm and cutting capacity of 30 kW losses on friction in hydrostatic bearings reach 35 kW (Perovic, 2012).

Lubrication of hydrostatic bearings with low viscous liquids, in particular, water presents separate interest considering constantly increasing requirements concerning specific speed of spindles. In work (Nakao et al., 2012) prospects of application of water lubrication is noted, designs of bearings are specified. However, question of anticorrosive protection of bearings and systems of their supply are highlighted insufficiently in technical literature and require further research.

It is commonly known that energy efficiency of spindle drive will decrease at growth of cutting speed which is caused by increase of mechanical and hydraulic power friction loss. According to the data (http://hyprostatik.de) it is established that power loss in high-speed (more than 100,000 rpm) spindle with hydrostatic bearings increases by 3-4 times in comparison with low-speed ones (to 4,000 rpm) and makes about 30 % of spindle drive power.

Thus, there is a contradiction in technological machining system between simultaneous maintenance of high values of productivity and energy efficiency of machining processes on machine tools. Moreover, existing technical solutions of fluid film spindle bearings are designed either for roughing of materials at low cutting speeds or high-speed finishing with low loading on the spindle of machine tool.

Overcoming of the specified contradictions will allow creating machine tools with expanded technological possibilities, by combination of processing with significant loadings, high-speed processing simultaneously providing energy efficiency gain and reduction of production cost.

2. PROMISING WAYS OF ENERGY EFFICIENCY GAIN OF SPINDLES WITH FLUID FLOW BEARINGS

Scientific approaches to energy research of machine tools and their components are characterized by a wide variety. Obviously, the most rational one is a systematic approach to designing of energy efficient machine constructions that can analyse elements and subsystems of machines and their interrelationships within a given hierarchical structure.

Regarding spindle units with fluid bearings two promising ways are offered (Fig. 1), namely, energy efficiency gain of existing elements of power systems and improving of structure efficiency of control systems.

Analysis of spindle energy flow should be performed in two dimensions: space and time. Spatial dimension involves analysis of energy flows in components and systems of the spindle unit, such as analysis of electricity consumption of spindle drives, analysis of power loss due to friction in bearings. Method of structural analysis is appropriate to identify processes and systems which are characterized by significant power consumption.

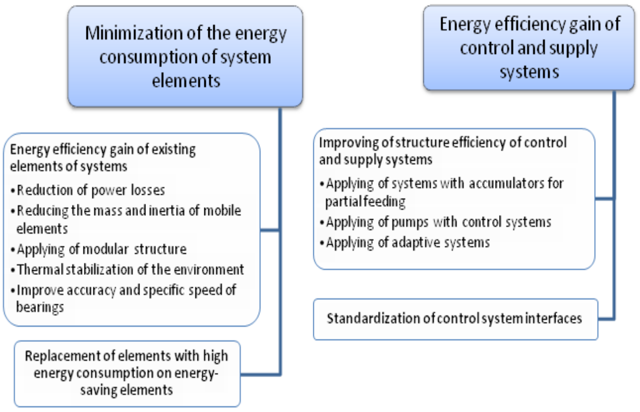

Fig. 1. Promising ways to increase energy efficiency of spindles with fluid bearings

Determination of energy loss can be made through appropriate passport data of separate mechanism subsystems or by known theoretical or empirical relationships. The best option in terms of adequacy of the obtained values of energy loss is experimental research. However, this approach is associated with considerable investments, characterized by long duration and is not always possible, especially in production environment. The most promising approach in terms of preliminary prognosis of energy consumption is the use of special software to analyse energy flow in processing (Estomad Project, 2013), but it requires apriori information on energy options and expanding of libraries of standard elements in order to take into account a broad range of power equipment.

Construction of generalized energy balance allows to identify "narrow" place of systems characterized by significant power consumption. The next phase - synthesis is directed on overcoming of these technical contradictions in the system; it begins with development of mathematical models, usually numerical modelling and experimental studies of mechanisms and machine systems with significant power.

A promising way to reduce power consumption is to decrease power loss in bearing system tools, reducing weight, inertia, acceleration of moving parts while ensuring high rates of accuracy, rigidity and heat resistance. Power loss in spindle units takes place primarily due to energy loss in mechanical and hydraulic elements of system, energy losses in motors.

For example, it was found that high-speed cutting power loss due to friction in the hydrostatic spindle bearing can exceed cutting power (Wardle, 2015; Chasalevris et al., 2016). Search of rational design solutions for units of friction and bearing lubrication systems is determined to minimize energy loss. Improvement of efficiency of hydraulic systems is possible by minimizing of volumetric, mechanical and hydraulic energy losses.

Reduced mass and inertia of moving parts reduces material and energy output of machines in general. Reduction of weight and inertia can reduce reactive power and electric energy loss which affects positively power consumption when accelerating work of the spindle. In addition, weight reduction can reduce energy loss in spindle bearings, raise vibration frequency of the system, and as a result, machining productivity.

Energy efficiency can be also increased due to the modular design structure of hydraulic power units that reduces pressure loss in highways and local supports; thermal stabilization of environment through convective heat removal through the walls of the tank and supply system elements.

Reducing energy consumption is also possible by improving of accuracy and specific speed of spindle bearings. This allows us to use high-speed processing of materials. Compared to the traditional usage high-speed processing can reduce specific energy consumption for processing workpieces by several times (Singh et al., 2012; Zahedi et al., 2015).

Replacement of machine components on energy efficient ones allows saving up to 25% of consumed electricity (Grossmann, 2015). For example, motors of smaller sizes that are more energy efficient may be also used with a moderate acceleration of moving parts of the machine.

Use of hydraulic accumulators for partial supply of hydraulic executive mechanisms allows to increase efficiency of throttles adjustment and to reduce power consumption by more than three times (Grossmann, 2015).

Use of special regulators (flow rate, pressure and power regulators) allows increasing of pump efficiency in several times. Similar results can be achieved by use of adaptive adjustment based on microprocessor control. It should be noted that one of the most effective solutions for minimization of energy consumption is application of unregulated pumps with frequency control in fluid supply system to spindle bearings.

Efficiency control systems, use of continuous monitoring of energy consumption play significant role in resource saving. Thus, control of machines should be adjusted to minimize energy options while ensuring high performance. Modern machines represent complex mechatronic systems with lots of measuring and converting elements for various purposes and principles of action. Improving of energy efficiency management systems and monitoring can be achieved through standardization and integration of these interfaces (Estomad Project, 2013).

Promising way to improve efficiency of industrial equipment is energy recovery. Regarding machine tools the recovery of kinetic energy during braking of high speed spindles using blocks of capacitors to store electrical energy is the most effective way of energy use (Pfefferkorn et al., 2009; Takabi et al., 2015).

3. DEVELOPMENT OF HIGH-SPEED HYBRIDFLUID CONSTRUCTION OF THE BEARING

In Chernihiv National University of Technology design of high-speed hybrid fluid bearing was developed to reduce energy loss and improve rapidity of spindle (Fedorynenko et al., 2014).

Increase of rapidity and efficiency of fluid bearing performance is achieved by spherical bearing pockets to which compressed fluid flows through adjustable fluid valves.

Implementation of bearing pockets to spherical form reduces power consumption caused by abrupt changes of flow form which reduces power loss because of viscous friction while increasing the rotor speed (Badescu, 2016).

Use of adjustable valves for fluid supply to the bearing with increasing frequency rotor allows stopping fluid flow to pockets of bearing, resulting in proceeds to the hydrodynamic bearing mode, thus reducing power loss as viscous friction and fluid flow. This causes increasing rapidity bearing.

Power system of hybrid fluid adjustable journal bearing is divided into five branches for supply of each of the pockets (Fig. 2). Each of the proportional valves 5–9 are previously adjusted to the required throughput of oil. For adjustment and control of power systems multipoint distribution valve 1 is designed, use of two gauges allows to control pressure in the bearing pockets.

During hydrostatic bearing fluid supply mode compressed fluid comes to five bearing pockets through valves 5-9, setting up a permanent throughput. Spindle speed is determined by encoder 4, after it a digital signal goes to microprocessor controller 3.

While speed of spindle exceeds pre-set limit, microprocessor controller 3 disables oil supply to valves 5, 8, 9, leaving valve 6 or 7 enabled. As a result, the bearing is operating in the hydrodynamic lubrication mode. While reducing rotation speed below the pre-set limit, controller 3 turns on the flow of the operating fluid to all bearing pockets, thereby restoring hydrostatic lubrication mode to ensure high load carrying capacity and radial stiffness of the bearing when operating at low speeds.

Friction and pumping power losses are reduced by decreasing of fluid supply to pockets in hydrodynamic mode and spherical bearing pockets. It allows increase of operating speed of bearing rotation.

4. RESEARCH RESULTS OF CONSTRUCTION OF HIGH-SPEED HYBRID FLUID BEARING

One of the main factors determining possibility of hydraulic lubrication of spindle at high operating speeds is energy loss in bearing spindle hub. Total energy loss in the bearings of hydraulic type consists of viscous friction loss P_μ in oil bearing layers and loss for pumping the operating fluid P_q.

Estimation of total energy loss in fluid bearing is made using the formula:

$$P_\Sigma = P_\mu + P_q.$$

Loss of power P_μ and P_q in hydrostatic bearing is determined using the formula (Fedorynenko et al., 2016):

$$P_\mu = 0{,}022 \cdot 10^{-13} \cdot \frac{\mu \cdot D^3 \cdot n^2 \cdot (L \cdot \theta + l_o \cdot \varphi)}{\delta},$$

$$P_q = p_H \cdot Q,$$

where: μ – dynamic viscosity fluid, Pa·s·10^{-3}; D – spindle diameter (front bearing), mm; n – spindle speed, rpm; L – length of operating surface of hydrostatic sleeve, mm; l_0 – land axial length, mm; δ – value of diametrical clearance, mm; θ – angular size of tangential lands, radians; φ – corner pocket size in tangential direction, radians; p_H – pump pressure, Pa; Q – operating fluid flow, m^3/s.

During work in hydrodynamic lubrication mode supply of operating fluid is required only for cooling of viscous zone. Bearing capacity is provided by hydrodynamic effect. Therefore, during hydrodynamic mode it is advisable to supply with operating fluid only one bearing pocket, thus reducing consumption of oil by several times, resulting in corresponding decrease in power loss for pumping of operating fluid in resistance during mode of hydrodynamic lubrication as compared to loss in hydrostatic mode.

It is known (Mahner et al., 2016) that the growth of dynamic viscosity of operating fluid leads to corresponding increase in power loss to viscous friction resistance, and with increasing frequency of spindle this process is more intense.

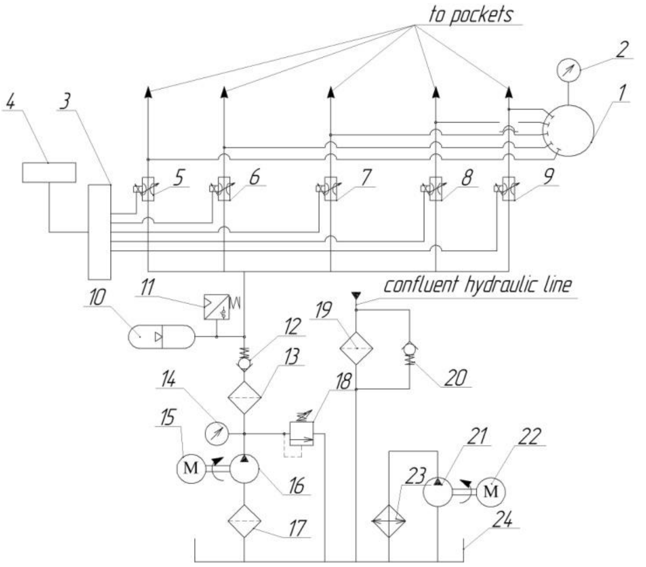

Fig. 2. Power system of controlled journal bearing: 1 – multipoint distribution valve; 2, 14 – pressure detectors; 3 – microprocessor controller; 4 – encoder; 5-9 – proportional valves; 10 – accumulator; 11 – pressure switch; 12, 20 – check valves; 13, 17,19 – filters; 15, 22 – electric motors; 16, 21 – fixed displacement pumps; 18 – pressure relief valve; 23 – coolant device; 24 – tank

Thus, in order to minimize energy loss it is offered to use appropriate operating fluids with low-viscosity (kinematic coefficient of viscosity v <1 cSt) for lubrication of high speed spindles. It is offered to use lubricating medium with fluid from distilled water with a complex system of corrosion protection - corrosion inhibitor and protector.

Forming high indicators of corrosion resistance of friction pairs is a determining factor to ensure high operational reliability of spindle bearings in general. Investigation of corrosion-electrochemical behaviour of hydrostatic bushings carried out by a complex system using an electrochemical method and physical and mechanical tests on fatigue.

It is established that the use of corrosion inhibitor – ε-caprolaktam with concentration of 1 g/L (Tsybulia et al., 2011) is an effective way to protect power system elements of hydrostatic bearing. To increase effectiveness of corrosion protection of the supplies system additional use of electrochemical method was offered. In relation to the inhibition, it does not require constant monitoring. As the tread, we propose use of zinc. Standard electrode potential of zinc in water is - 0.761 V, and iron - 0.44 V, with this combination on zinc will focus on anode process, and on the elements protected by cathode process.

Constructive response tread protection is offered in the form of fitting that is placed in the injection hydraulic line feed system spindle bearings. The fitting is made of zinc, directly connected by tapered thread with manifold injection of hydraulic pumps.

As we can see, use of special low-viscosity lubrication can reduce total energy losses in the bearing by almost 6 times (Fig. 3) comparing to mineral oilI-5A (μ=5·10^{-3} Pa·s, at temperature of 50 degrees Celsius).

Thus, total energy loss in the modernized bearing is lower by 1.5 times during hydrostatic lubrication mode and 4 times during hydrodynamic mode than loss in the base version of bearing (Fig. 4, a).

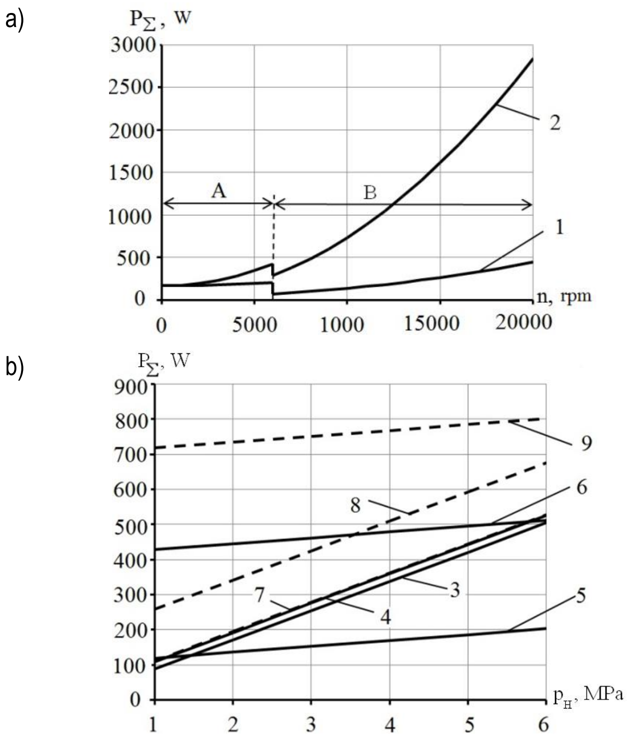

Fig. 3. Dependence of total energy loss P_Σ in the bearing: a – on the speed n of spindle: 1 – special low-viscosity lubrication, 2 – oil I-5A; A – hydrostatic lubrication mode; B – hydrodynamic lubrication mode; b – supply pressure p_H (solid curves – special low-viscosity lubrication; dashed curves - lubrication with oil I-5A): 3, 7 - n = 2,000 rpm; 4,8 - n = 5,000 rpm; 5,9 - n = 10,000 rpm; 6 - n = 20,000 rpm

In Fig. 4, dependence of total energy loss on P_Σ effective power during grinding P_{ef} and overall power consumption while grinding details on grinding machine tools P_t ($P_t = P_\Sigma + P_{ef}$) on the speed of spindle *n* is presented.

The developed construction has relay control of lubrication mode which is realised by microcontroller device. The output characteristics of hybrid bearing are changed step-like at transition from hydrostatic to hydrodynamic mode of lubrication and vice versa due to the relay control system of the lubrication mode. As is seen from Figs. 3 and 4, actuation of the relay controller leads to abrupt change of power losses P_Σ, P_t at spindle speed of 6,000 rpm due to the change of fluid supply to the bearing pockets at transition to another lubrication mode.

With increasing of spindle speed up to 6,000 rpm when the bearing still works in hydrostatic lubrication mode, power P_{ef} differs by 14% from P_t during processing of the details (final grinding of steel 45). While increase of the speed of rotation from 6,000 to 20,000 rpm takes place at installed hydrodynamic lubrication mode, P_{ef} relation to P_t during processing of the details is in the range of 4 to 7%.

Assessment of energy efficiency of base and modernized bearing of spindle is performed in terms of specific electricity consumption of machine tool (*Ep*) (the ratio of consumed electricity facilities to the volume of products produced during the same time under certain conditions). Energy loss of main motion and total power consumption of auxiliary machinery and machine were taken into consideration while determining specific consumption of electric energy.

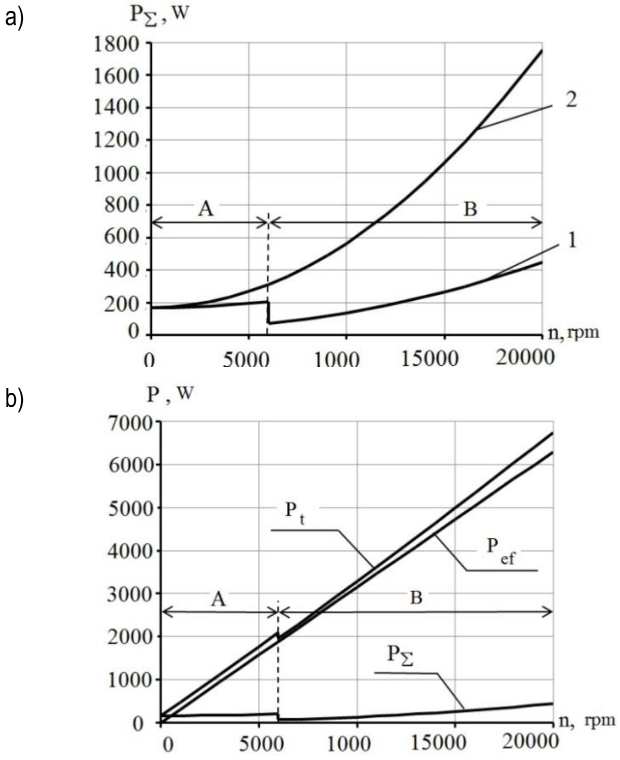

Fig. 4. Dependence of total energy loss P_Σ (a) and energy losses P during grinding details (b) on the speed n of spindle: 1 – controlled bearing; 2 – prototype; A – hydrostatic lubrication mode; B – hydrodynamic lubrication mode

It was discovered that when spindle rotation speed is up to 10,000 rpm, unit costs of electricity of basic and modernized machines differ slightly. But with increasing of rotational speed up to 20,000 rpm rapid growth of energy consumption base model machine (*Ep*) is observed to value of 2.91, but power consumption of machine tool with upgraded model of a new type of bearing is 1.2.

One of the main spindle indicators that determine machining accuracy is bearings stiffness. To evaluate static radial stiffness C_b of bearings we used the formula $C_b = dW/de$, where *W* – radial bearing film force at static loading; *e* – bearing eccentricity under external force acting.

Bearing film force *W* can be define as: $W = \sqrt{W_x^2 + W_y^2}$, where W_x, W_y – projections of the force *W* on the coordinate axes X and Y respectively. Let us consider translational movements of bearing journals without misalignment. In such case for idealized bearing surfaces (no account of surfaces imperfection tendencies), we can define forces as:

$$W_x = \frac{DL}{2} \int_0^{2\pi} p\left(\varphi_p\right) \cos\left(\varphi_p\right) d\varphi_p,$$

$$W_y = \frac{DL}{2} \int_0^{2\pi} p\left(\varphi_p\right) \sin\left(\varphi_p\right) d\varphi_p,$$

where: $p(\varphi_p)$ – pressure function on the bearing surface; φ_p – polar angle of the bearing surface.

Determining pressure function $p(\varphi_p)$ in hydrostatic bearings is a separate and complicated task. The procedure for determination of the pressure function was considered in detail in the works (Fedorynenko et al., 2015; 2016).

Theoretical plots are given for precise lathe UT16A in Fig. 5. As is seen in Fig. 5, stiffness of the prototype and the hybrid bearing in the hydrostatic mode of lubrication are approximately equal. Stiffness of the hybrid bearing in the hydrodynamic lubrication mode (curve 2) is less than the prototype (curve 1) and increases with the spindle speed. It should be noted that stiffness of the hybrid bearing satisfies conditions of a high-speed finish turning machining.

Hydrostatic spindle thermal stability is of key importance to achieve high accuracy of machining. The main sources of heat in the hydrostatic spindle are bearings. In the works (Salazaraet al., 2017; Zuo et al., 2013) it is noted that in order to increase spindle thermal stability it is necessary to minimize heating of the fluid in slide bearings. Fig. 5 shows temperature rise ΔT for a single pass of lubricant between bearing inlet and outlet of the prototype design (curve 3) and hybrid bearing (curve 4) depending on the spindle speed. ΔT parameter was estimated by formula (Rowe, 2012):

$$\Delta T = \frac{p_H(1+K)}{\rho c}$$

where: $K = P_\mu / P_q$; ρ – fluid density, kg/m^3; c – specific heat capacity, J/kg K.

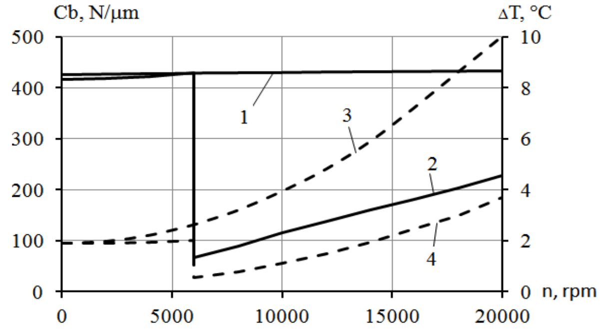

Fig. 5. Radial bearing stiffness Cb (solid curves) and fluid temperature rise ΔT (dashed curves) vs spindle speed n: 1, 3 – prototype; 2, 4 – controlled bearing

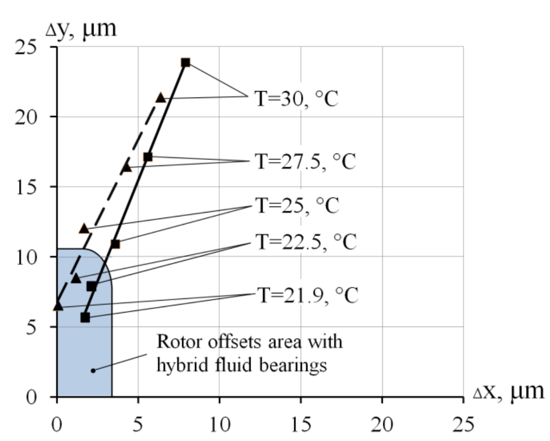

Fig. 6. Experimental values of the rotor thermal offsets Δx, Δy along X and Y coordinates respectively at turning machining: solid line – pocket pressure equals 2 MPa; dashed line – pocket pressure equals 3 MPa

As we can see, hybrid spindle bearings design provides fluid heating 2.6 times less that prototype at maximum spindle speed.

Spindle heat resistance is characterized by offset of the spindle axis under the action of thermal field in machining process. Fig. 6 shows offsets Δx, Δy of the spindle rotor with hydrostatic bearings during turning machining of workpieces depending on the lubricant temperature T inside front bearing. Rotor displacements were measured by laser sensors mounted on two coordinate axes X and Y at distance of 200 mm from the front spindle bearing. Precise mandrel was installed in the rotor to measure spindle offsets. The workpieces were fixed to the mandrel by a special fixing device. The method of experimental studies of rotor offsets is considered in detail in the works (Fedorynenko et al., 2016; Huang et al., 2016).

Increase of lubricant temperature due to friction in the hydrostatic bearing leads to a substantial displacement of the rotor on its overhang area. Increase of pockets pressure in the bearing up to 3 MPa reduces the rotor offsets up to 2 times in a horizontal plane. Use of a hybrid design of spindle bearings makes it possible to reduce rotor thermal offsets by 3-4 times at turning machining in comparison with the prototype.

5. CONCLUSIONS

Developed scientific approaches can be used to improve energy performance of high-speed fluid bearings of spindles as well as to design new facilities based on analysis of similar purpose.

According to the results shown in the article, due to a new design of controlled journal hybrid bearing it was possible to reduce total energy loss in enhanced resistance by 1.5 times during hydrostatic lubrication mode and 4 times during hydrodynamic mode compared to loss in the base version of the bearing. Beside this, application of the hybrid bearings allows us to reduce spindle thermal offsets at turning machining up to 4 times compared with hydrostatic journal bearings.

Effective way to improve energy efficiency of spindles with fluid bearings is application of operating fluids with low viscosity. Use of special lubrication based on water with corrosion inhibitor (ε - caprolaktam) can reduce energy loss in journal bearing almost by 6 times at spindle speed 20,000 rpm compared with lubrication by mineral oils.

It is established that with spindle speed of 20,000 rpm energy consumption of lather machine tool with the new design of journal spindle bearings is reduced by 2.4 times in comparison to the base one.

Prospects for future research include experimental validation of received theoretical results and optimization of bearings design to find optimal solutions for energy efficiency and productivity.

REFERENCES

1. **Badescu V.** (2015), Optimal profiles for one dimensional slider bearings under technological constraints, *Tribology International,* 90, 198-216.
2. **Cao H, Zhang X., Chen X.** (2017), The concept and progress of intelligent spindles: A review**,** *International Journal of Machine Tools and Manufacture,* 112, 21-52.
3. **Chasalevris A., Dohnal F.** (2016), Improving stability and operation of turbine rotors using adjustable journal bearings, *Tribology International,* 104, 369-382.

4. **Diaz N., Redelsheimer E., Dornfeld D.** (2011), Energy Consumption Characterization and Reduction Strategies for Milling Machine Tool Use, *Sustainability in Manufacturing. Energy Efficiency in Machine Tools*, 263 - 267.
5. EC - 7th Framework Programme. Challenge 6: ICT for Mobility, Environmental Sustainability and Energy Efficiency. Deliverable D3.3: “Design for energy efficiency” (2013), *Estomad Project*.
6. **Fedorynenko D., Boyko S., Sapon S.** (2015), The search of the spatial functions of pressure in adjustable hydrostatic radial bearing**,** *Acta Mechanica et Automatica*, 9(1), 23-26.
7. **Fedorynenko D., Boyko S., Sapon S.** (2016), Accuracy of spindle units with hydrostatic bearings, *Acta Mechanica et Automatica*, 10(2), 117-124.
8. **Fedorynenko D., Sapon S.** (2016), Spindle Hydrostatic Bearings (in Ukrainian), *ChNUT*.
9. **Fedorynenko D., Sapon S., Habibulina A.** (2014), Adjustable Journal Hybrid Fluid Bearing, *Patent of Ukraine No 89288*.
10. **Grossmann K.** (2015), Thermo-energetic Design of Machine Tools, *Springer International Publishing.*
11. **Huang P., Lee W., Chan C.** (2016), Investigation on the position drift of the axis average line of the aerostatic bearing spindle in ultra-precision diamond turning, *International Journal of Machine Tools and Manufacture,* 108, 44-51.
12. **Mahner M, Lehn A., Schweizer B.** (2016), Thermogas- and thermo-hydrodynamic simulation of thrust and slider bearings: Convergence and efficiency of different reduction approaches, *Tribology International,* 93, 539-554.
13. **Nakao Y., Mimura M., Kobayashi F.** (2012), Water energy drive spindle supported by water hydrostatic bearing for ultra-precision machine tool, http://www.researchgate.net/publication/228896125.
14. **Perovic B.** (2012), *Hydrostatic guides and bearings: basic principles, calculation and design of hydraulic diagrams* (in German), Springer-Verlag Berlin Heidelberg.
15. **Pfefferkorn F., Lei S., Jeon Y., Haddad G.** (2009), A metric for defining the energy efficiency of thermally assisted machining, *International Journal of Machine Tools and Manufacture,* 49, 357-365.
16. **Rowe W.B.** (2012), Hydrostatic, aerostatic and hybrid bearing design**,** *Butterworth-Heinemann Press*.
17. **Salazara J, Santosa I.** (2017), Active tilting-pad journal bearings supporting flexible rotors: Part I – The hybrid lubrication, *Tribology International,* 107, 94-105.
18. **Singh V., Venkateswara Rao P., Ghosh S.** (2012), Development of specific grinding energy model**,** *International Journal of Machine Tools and Manufacture,* 60, 1-13.
19. **Takabi J., Khonsari M.** (2015), On the thermally-induced seizure in bearings: A review**,** *Tribology International,* 90, 118-130.
20. **Tsybulia S., Fedorynenko D., Kostenko I., Buialska N.** (2011), Corrosion Protection of Elements of Spindle Hydrostatic Bearing of Machine Tools (in Ukrainian), *Materials of the XI International Conference: Efficiency Implementation of Scientific, Resource and Industrial Facilities in Modern Terms, Kyiv*.
21. **Wardle F.** (2015), *Ultra Precision Bearings*, *Elsevier*.
22. **Zahedi A., Tawakoli T, Akbari J.** (2015), Energy aspects and workpiece surface characteristics in ultrasonic-assisted cylindrical grinding of alumina–zirconia ceramics, *International Journal of Machine Tools and Manufacture,* 90, 16-28.
23. **Zuo X., Wang J., Yin Z., Li S.** (2013), Comparative performance analysis of conical hydrostatic bearings compensated by variable slot and fixed slot, *Tribology International,* 66, 83-92.
24. http://hyprostatik.de/fileadmin/inhalte/pdfs/hydrostatic_spindles.pdf

Acknowledgement: The presented results are part of projects 0113U000503 "Development of the Precision-Controlled Hydraulic Bearings of High-Speed Spindle Units" and 0115U002362 "Development of Energy-Efficient High-Speed Spindles with the Adaptive Journal Bearings" funded by the Government of Ukraine.

DOI 10.1515/ama-2017-0032

STRUCTURAL TESTS OF FREIGHT WAGONS ON THE BASIS OF SIGNALS GENERATED BY PIEZOELECTRIC MACRO FIBER COMPOSITES

Marek PŁACZEK[*], **Andrzej WRÓBEL**[*], **Andrzej BUCHACZ**[*]

[*]Institute of Engineering Processes Automation and Integrated Manufacturing Systems, Faculty of Mechanical Engineering,
Silesian University of Technology, ul. Konarskiego 18A, 44-100 Gliwice, Poland

marek.placzek@polsl.pl, andrzej.wrobel@polsl.pl, andrzej.buchacz@polsl.pl

received 10 October 2016, revised 16 September 2017, accepted 19 September 2017

Abstract: Paper presents a report of a research work that concerns possibilities of freight wagons modernization using new composite materials. The main aim of presented work was to verify the possibility of inference from the dynamic response of the wagon about the changes in its technical condition. During the presented works tests on real objects were carried out using Macro Fiber Composite (MFC) piezoelectric transducers glued to the freight wagon's frame. The dynamical response of the wagon was measured while the object was driving. On the next stage the measured signal was generated on a laboratory stand using electrodynamic modal shaker and vibrations of the laboratory model were measured. Measured signals were juxtaposed on charts and analysed. The aim of this work was to verify if it is possible to detect the change in the system using measurements of vibrations that are being generated during exploitation of the freight wagon.

Keywords: Dynamic Response, Freight Wagon, Piezoelectric Transducers, Smart Materials, Analysis of Vibration

1. INTRODUCTION

The aim of presented research work was to modernize the analysed wagon during its renovation using new materials. This work is a continuation of the previous research works concerned with analysis of new, composite materials application in freight wagons (Wrobel et al., 2015; Baier and Zolkiewski, 2013; Placzek et al., 2015 a,b). Effects that are to be achieved by the modernization are better corrosion protection of the wagon elements, easier unloading of the wagon in winter conditions (no freezing of the cargo to the sides and floor of the wagon), reduction of the weight of the wagon while its load increases and easier management of freight wagons during exploitation. The 4-axle open wagon series EAOS type 1415 A3 produced by BREC Belgium is being taken into consideration because it is one of the most popular type of wagons designed to unload with the use of tipplers.

An opportunity to apply new materials and new methodology allows designing devices and systems that, for example are more effective, have better properties and lower costs of production. This is why a lot of effort is spent on development of any types of devices that are used (Jamroziak, 2013; Rusinski et al., 2012; Tuma, 2009; Jamroziak et al., 2013). Smart materials, so the materials that can change one or more of their properties during operations and this change can be controlled bring a lot of new possibilities as well. Piezoelectric transducers which are widely used in many kinds of technical devices and number of their applications are still increasing are also smart materials. They properties caused that they can be used in large variety of applications, for example in vibration damping or excitation, energy harvesting systems, as sensors or in order to obtain precise elements positioning (Tuma et al., 2011; Placzek, 2015; Buchacz et al., 2014, 2015).

In 1996 Macro Fiber Composites (MFC) was invented by NASA. MFC transducer is consists of rectangular piezo ceramic rods sandwiched between layers of adhesive, electrodes and polyimide film. Main benefits of the MFC are: increased strain actuator efficiency, damage tolerance, environmentally sealed packages, available as elongators and contractors (Placzek et al., 2015b; Buchacz et al., 2015). The development of transducers allows new applications of piezoelectric materials and improves operation of existing devices.

In this work some benefits obtained by using new piezoelectric transducers application is presented. In previous works for example efficiency of both PZT and MFC transducers used as actuators of the mechanical system was presented. An analysis of the considered mechatronic system was done using a discrete-continuous mathematical model and an approximate method presented in previous publications (Placzek, 2015; Buchacz et al., 2014, 2015). On the other hand, computer aided methods of designing, manufacturing and product life cycle management are also powerful tools that helps to design and produce modern technical devices (Paprocka et al., 2014; Banas et al., 2015; Monica, 2015; Klarecki et al., 2015). Modern systems include elements from different science areas, such as mechanics, electronics and informatics. Such connection brings new possibilities and new effects, so those systems can be called mechatronic systems (Buchacz and Galeziowski, 2012; Gwiazda et al., 2015).

Rail transport is a very important part of the modern economy, one of the components determining its dynamic development. It is therefore important to conduct research and taking action aimed at the development and refinement of this branch of industry. Numerous studies are conducted, aimed at introducing new technologies and solutions, both in terms of railway infrastructure and logistics management systems, as well as in traction vehicles themselves (Grebowski and Zielinska, 2015; Oleszak et al., 2013; Stypula; Stypula, 2009; Bruni et al., 2011; Connolly et al., 2014; Hecht 2009; Herwig and Bruhwiler, 2011; Jönsson et al., 2008, Kovalev et al., 2009; Mehrpouya and Ahmadian, 2009). Such actions directly translate into an increase in its effectiveness, safety, reduction of burden on the environment and society. This paper contains a report on the part of works conducted in the research and development project entitled "Analytical and experimental studies and determination of the structural features of components and assemblies in innovative structure of repaired wagons". This project is realized within the Program of Applied Research by Institute of Engineering Processes Automation and Integrated Manufacturing Systems of Silesian University of Technology together with consortium partners: company DB Schenker Rail Poland SA and Germaz. The main objective of the project is to develop a technology of modernization of freight wagons for the transport of coal and aggregates, through the use of innovative materials and technologies to repair this type of wagons during periodic repairs. Actions which have been undertaken within the project are to improve the operating conditions considered types of wagons by increasing their resistance to corrosion and freezes transported cargo to the shell of the body in the winter conditions, and thus an easier unloading (Wrobel et al., 2015; Baier and Zolkiewski, 2013; Placzek et al., 2015 a,b). An additional objective is also verification of strength of modernized carriages and an estimation of the possibility of reducing their weight, while maintaining or increasing the permissible load. One of elements of the project is also to develop a system for diagnosing the technical condition of the modernized shell of wagon body during operation. For this purpose the use of non-destructive testing methods of technical state of constructions will be used, including methods that use the analysis of dynamic response of the object. Therefore research is conducted which examines the possibility of use of the foils with piezoelectric properties as sensors used in the system of vibration measurement of tested items (Placzek et al., 2015a). These research efforts are a continuation of previous work related to the analysis of possibilities to use of composite materials as a part of the wagons boxes shell. Application of the composite panels to the freight wagon's body shell was proposed as the solution that can solve mentioned problems during exploitation of freight wagons (Wrobel et al., 2015; Baier and Zolkiewski, 2013; Placzek et al., 2015 a,b). The composite panels composed of fiberglass and epoxy resin were proposed. They will be mounted on the body shell using rivet nuts. What is more the body shell of the modernized freight wagon will be painted using an anti-corrosion agent.

2. A PROCESS OF QUALIFICATION TO REPAIR

The main aim of the system designed for of inferred from the dynamic response of the wagon about the changes in its technical condition is to support a process of freight wagons qualification to repair. At this moment all freight wagons should be verified about their technical condition at a certain time interval. During the qualification process a qualifying protocol is used. In the DB Schenker Rail Poland SA Company in order to decide which elements of the freight wagon should be repaired or replaced by the new ones the protocol includes such data as:

- the type of the analysed freight wagon;
- the drawings of the analysed type of wagons including views of all side walls and the floor;
- the identification number of the wagon;
- the date and type of the previous repair and the date and type of the actual renovation;
- the table with listed elements of the wagon with the possibility to mark whether the item is suitable for repair, replacement, or whether it is in good technical condition;
- the signatures of the responsible people and the place for other notes.

During mentioned research work also a statistic analysis of data from qualifying protocols were analysed in order to verify if there are elements the most exposed to damage during standard exploitation of the freight wagons. Qualifying protocols from years 2012 up to 2014 were analysed. The number of analysed protocols was 298 for different types of freight wagons. Protocols were scanned and sorted taking into account types of freight wagons. Data from protocols were analysed in order to specify the percentage of repairs of individual wagons elements. Obtained results were presented on charts. In order to analyse date from protocols elements of the freight car's box were named and marked on the scheme of the freight wagon. In Fig. 1 names of the EAOS 1415 A2 and A3 wagon's elements designations are presented. The front of the wagon is indicated by the position of the brake cylinder.

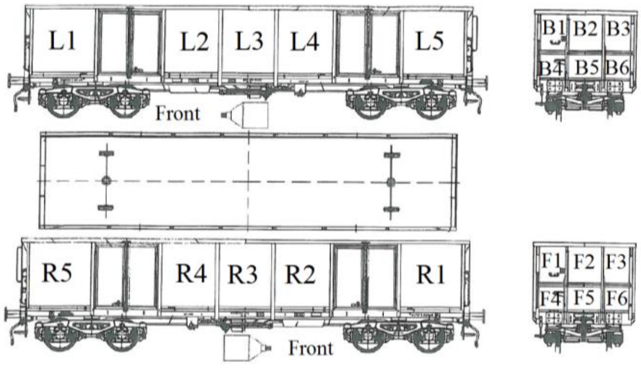

Fig. 1. Designation of EAOS 1415 A2 and A3 wagon's elements, where symbols denotes: L – the left side, R – the right side, F – the front, B – the back of the wagon

The most important, taking into account assumption of modernization of the freight wagons using composite panels mounted to the wagon's shell of the body, is the information about the damage of its elements. Percentage of repairs of individual elements of the shell of the body is presented in Fig. 2.

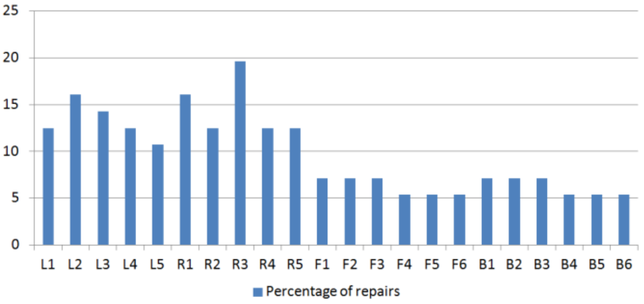

Fig. 2. Percentage of individual elements repairs of the body shell of freight wagon EAOS 1415

Presented results of qualifying protocols analysis shows that there are some different between percentage of repairs of different elements of the freight wagons body shell. In case of type EAOS 1415 freight wagons it can be noticed that elements of the side walls were repaired more often than elements of the front wall and the back wall. What is more it can be noticed that even simetrical elements of the freight wagon (ex. L3 and R3) have different values of percentage of repairs. It can be explain by the random characteristic of the corrosion process of freight cars. It should be mentioned that in order to obtain more precise information about the process of damage of individual elements of the freight wagons body shell during their exploitation it is necessary to carry out a more accurate operational documentation starting from the production of wagons, which will take into account operating conditions of carriage, such as the type of transported cargo, as well as all carried out repairs.

The system that is to be developed should inform about destruction of the wagon's body shell during standard operation of the wagon. This should help to detect of major defects of wagon's body shell without transporting it to the service station. In order to develop such system it is necessary to verify the possibility of inference from the dynamic response of the wagon about the changes in its technical condition during its standard operation.

3. MEASUREMENTS OF WAGON'S VIBRATION DURING OPERATION

At the first step of the carried out tests measurements of the wagon's elements vibration during operation were carried out.

The object of research is the four axial freight wagon of ordinary type Eaos 1415-A3 production BREC Belgium. It is presented in Fig. 3. It was being taken into consideration because it is one of the most popular types of wagons designed to unload with the use of tipplers.

Fig. 3. The considered type of freight wagon

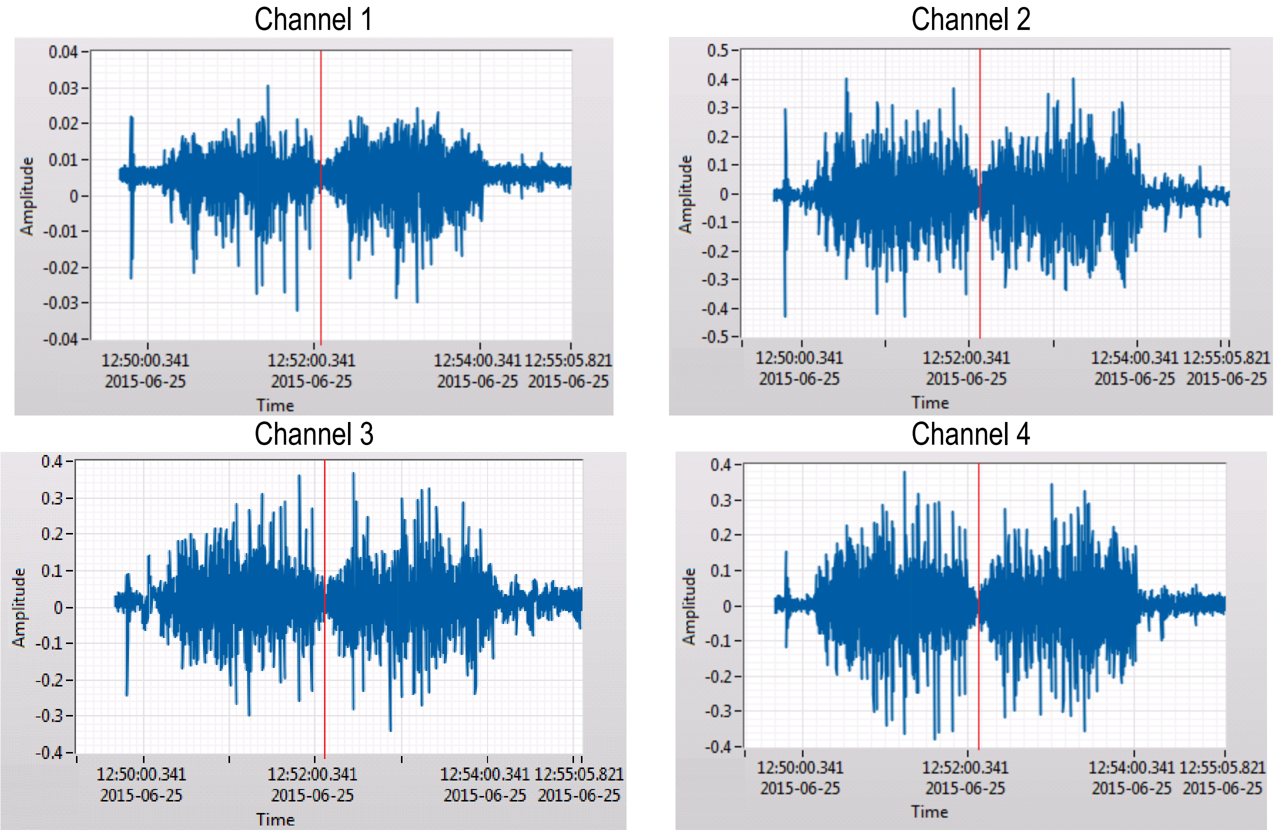

Fig. 4. The measured profile of excitations (empty wagon and max. speed 10 km/h)

Measurements were carried out using analogue input card type NI-9215 (http://www.ni.com/pdf/manuals/373779a_02.pdf) and portable device NI cDAQ-9191 (http://www.ni.com/datasheet/pdf/en/ds-371) – the compact 1-Slot chassis which allows Send data to a host PC over Ethernet or IEEE 802.11 Wi-Fi. As sensor M-8514-P1 model of Macro Fiber Composite transducer was used with active area 85 x 14 mm (http://www.smart-material.com/MFC-product-main.html). Four sensors were glued on the surface of the frame and body shell of the tested wagon and connected to the portable measurement system for data acquisition. Measurements were carried out while the observed train was driving (locomotive and two wagons) with the maximum travelling speed about

10 km/h. The speed of the train was limited as a result of the applicable regulations because measurements were carried out in the area of the railway repair company. There was no agreement to conduct research during normal exploitation. The train was driving a section of about 400 meters, stopped and then it was returning. The test was repeated five times to verify the repeatability of the results. Measurements were made in repair facility of DB Schenker Rail Poland in Rybnik. Measurement points were as:

Channel 1 – the centre of the top band of the box, interior of the freight wagon;

Channel 2 – the support frame – the bottom surface of the main, outer beam of the frame;

Channel 3 – the support frame – the inner surface of the main, outer beam of the frame;

Channel 4 – the support frame – side surface of the cross-beam.

Measuring points were selected on centre points of main beams of the wagon's frame and on the centre of the top band of the box because it was predicted that deformation of surfaces of these elements of the wagon construction will be the biggest. This was important for the measurements using MFC piezoelectric foils glued on surfaces of these elements.

The main aim of the measurements was to acquire a profile of excitations that are elements of the freight wagon exposed to during exploitation of the wagon. This profile was in the next step used in tests using laboratory stands in order to verify their dynamical response onto the excitation occurring during operation. In Fig. 4 examples of results of measurements obtained for the described channels are presented. The measured profile of excitations occurring during operation for empty wagon and maximal speed 10 km/h for all measuring points is presented. The red vertical line separates two operating ranges: in the first range the wagon was pulled by the locomotive, while in the second one the wagon was pushed by the locomotive.

It can be observed that the electric voltage generated by the piezoelectric MFC sensors has not a high value but measured signal can be used in order to reproduce the extortion profile course during laboratory tests.

The measured signal was then analysed used Fast Fourier Transform to verify the resonance zones of the vibrating elements. An example of results of measured signal FFT analysis obtained using Hanning window is presented in Fig. 5.

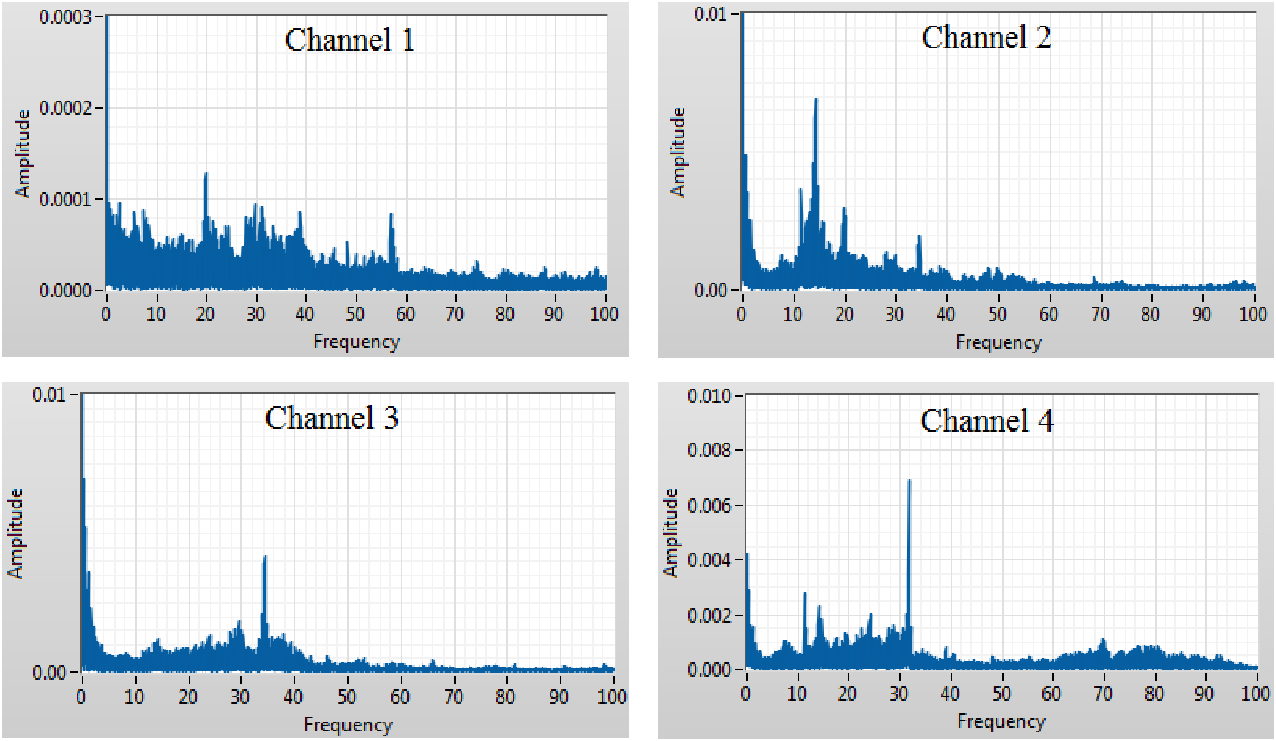

Fig. 5. An example of results of measured signal FFT analysis

The carried out measurements proved that results are repetitive and can be used in laboratory tests. During all measurements it could be observed that obtained results are repeatable (taking into account range of possible measurement errors) for all tested measuring points without influence of the weather conditions and temperature. It can be concluded that Macro Fiber Composite piezoelectric transducers proposed as sensors in developed system could be successfully used. They have a lot of advantages which causes that they can be proposed as a very good solution, for example they can be easily applied to the structure by gluing it to its surface. They are produced in the form of thin foils, so they also can be easily laminated into the structure of the composite panels that will be mounted in the modernized freight wagons. What is more they are resistant to weather conditions and do not require additional power source. What is more, for a low frequencies measurments the store & hold amplifier can be used with the MFC transducers what can improve precision of measurements (http://www.smart-material.com/MFC-product-main.html).

4. MEASUREMENTS USING LABORATORY STAND

The composite panels composed of fiberglass and epoxy resin were proposed. They will be mounted on the body shell using rivet nuts. What is more the body shell of the modernized freight

DOI 10.1515/ama-2017-0032

wagon will be painted using an anti-corrosion agent. Application of the new materials in the considered freight wagons is connected with the need to conduct a series of studies of the proposed materials properties, taking into account their strength analysis, abrasion resistance, fatigue resistance, and other properties important because of the working conditions in the modernized freight wagons. Very important property that has strong influence onto the safety of the modernized freight wagons exploitation is also the verification of the new elements flammability. Results of those studies were presented in other papers (Wrobel et al., 2015; Baier and Zolkiewski, 2013; Placzek et al., 2015 a,b).

a)

b)

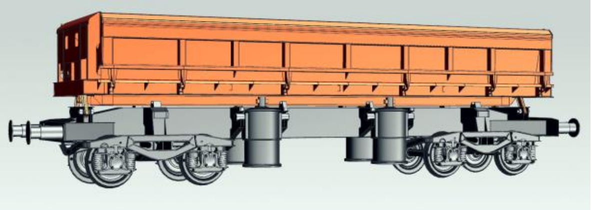

Fig. 6. The type of type 418V freight wagon (a) and its CAD model (b)

a)

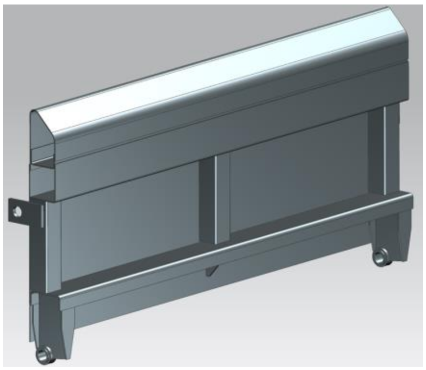

b)

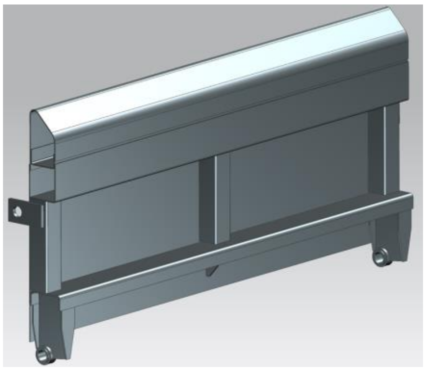

Fig. 7. The CAD model of the tested piece of 418V freight wagon's side (a) and The CAD model of the laboratory stand (b)

At the next step the measured profile of vibration excitation that is a result of the operation of the freight wagon was used for tests on a created laboratory stand. The laboratory stand was prepared for strength analysis of a side of a hopper freight wagon type 418V. This type of wagon is presented in Fig. 6.

In Fig. 7a) a CAD model of the tested piece of the freight wagon's side is presented. In carried out measurements the laboratory stand for strength analysis of the 418V freight wagon side element was used. A CAD model of the stand with the analysed wagon's side is presented in Fig. 7b). The side's element was prepared in 1:2 scale.

During measurements the freight wagon's side was excited using vibration test system produced by TIRA GmbH. As sensors also Macro Fiber Composite M-8514-P1 piezoelectric transducers were used and connected with analogue input cards and portable device NI cDAQ-9191. Measurements were carried out with and without composite panels mounted to the wagon's side using rivet nuts. The aim of this work was to verify if it is possible to detect the presence of composite panels mounted to the tested wagon's side element. The tested element was excited using electrodynamic shaker and vibration profile obtained during the measurements carried out on the real freight wagons. Vibrations of the analysed side were measured in four measuring points using MFC piezoelectric transducers. The MFC sensors were glued to the surfaces of the side's frame as well as to the sheet metal fill. Measuring points were selected on centre points of main beams of the wagon's side model and on the centre point of the composite panel. It was predicted that deformation of surfaces of these elements of the wagon's side model will be the biggest.

5. RESULTS

Results obtained for measuring points on the side's frame and on the sheet metal fill for the wagon's side model with and without composite panels are presented in this work. As the next step of the carried out analysis the Fast Fourier Transform of measured signals was carried out in order to verify if any change in the obtained results can be observed. Results of the FFT analysis of measured signals obtained for the system with and without composite panels are juxtaposed in Fig.9 up to frequency 200 Hz. The red line denotes results obtained for the model of the freight wagon's side without any additional element while the blue line denotes results for the model with composite panels. The panels were made of fiberglass and epoxy resin with thickness 6 mm. They were mounted using rivet nuts.

It can be noted that for both measuring channels the analysed system has higher values of the amplitude for all frequencies of vibrations in case when there is no composite panels mounted. Such results can be very useful for the algorithm that will be use in the system designed for modernized freight wagons technical condition monitoring during their exploitation. There may be a possibility to detect destruction of the mounted composite panels by the system on the basis of measured signals from applied piezoelectric foils. The system should also detect if the freight wagon is loaded or it is used empty and inform about its status using GPS system. Such information can be very useful for better managing of freight wagons and for data collecting in the system that should record the history of the wagons exploitation.

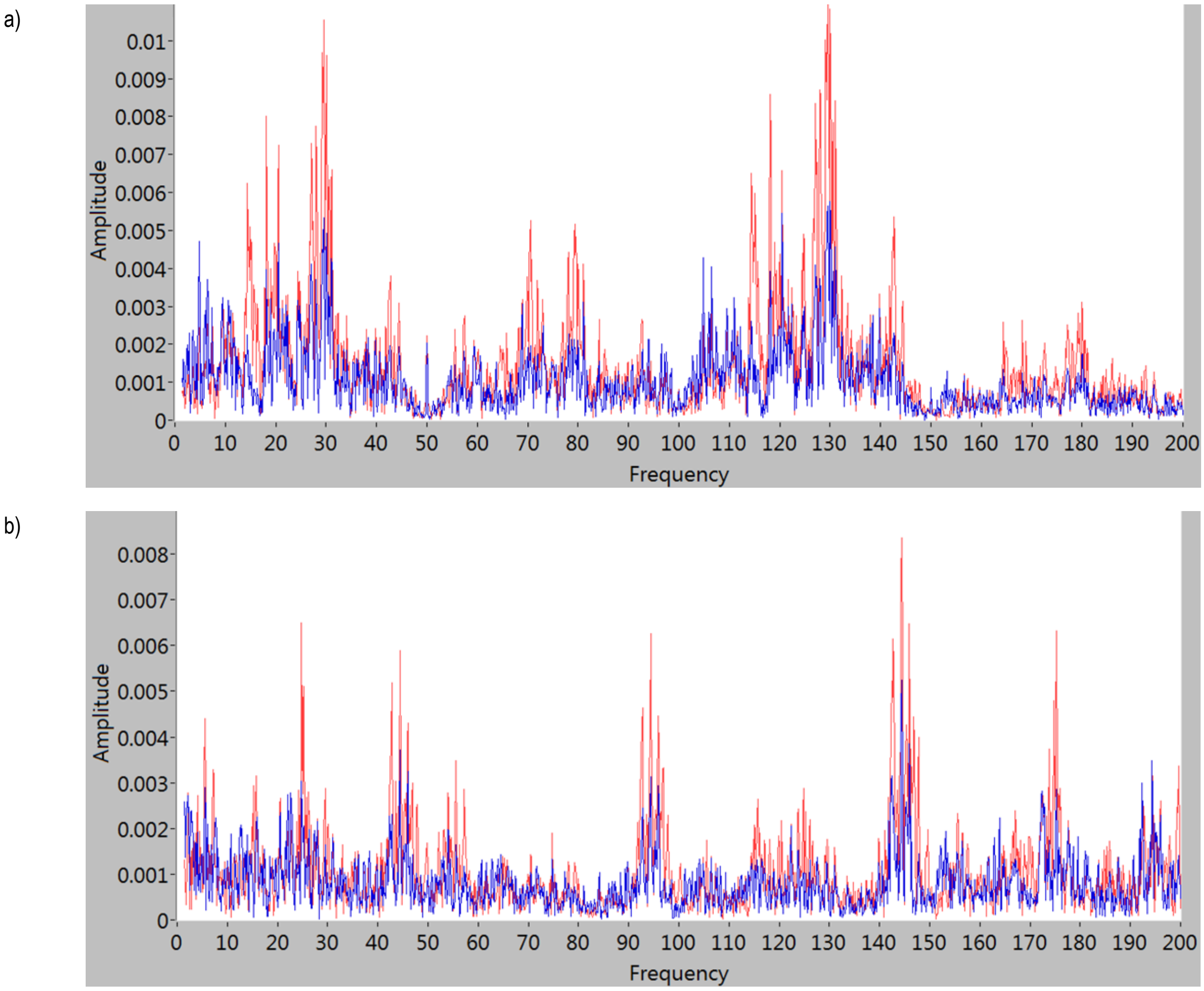

Fig. 9. Results of the FFT analysis of measured signals juxtaposed for the system witch (the blue line) and without (the red line) composite panels for channel 1 (a) and channel 2 (b)

6. CONCLUSIONS

Carried out tests and measurements on freight wagons as well as using laboratory stands proved that Mecro Fiber Composite piezoelectric transducers can be successfully used as sensors for measurements of freight wagon's elements vibrations. They can be easily applied to the surface of monitoring structure as well as laminated in composite panels that will be used during proposed freight wagons modernization. What is more they can be easily protected to weather conditions.

During carried out tests on the real freight wagon the speed was limited and it was lower than speed of a train during its standard exploitation. It caused that values of measured signals were lower than they can be predicted in application on freight wagons for standard operation. However, using measured profile of excitation it was possible to infer about the status of the laboratory stand. Taking into account obtained results of laboratory tests it was possible to conclude whether composite panels are connected to the tested model of the freight wagon's side or they are lacked. Obtained results allows to conclude that proposed method of control of technical condition of modernized freight wagons may be a good solution.

In further research more measurements on laboratory stands and especially on real objects during their standard exploitation will be carried out in order to verify repeatability of the obtained results and to take into account influence of various conditions such as weather conditions, deformations of the wagon's body shell that are results of its exploitation, mainly unloading using excavators etc. The influence of changes in monitored system created during its exploitation appears as a main problem which may result in system malfunction.

REFERENCES

1. **Baier A., Zolkiewski S.** (2013), Initial research of epoxy and polyester warp laminates testing on abrasive wear used in car sheathing, *Eksploatacja i Niezawodnosc – Maintenance and reliability*, 15(1), 37–43.
2. **Banas W., Sekala A., Gwiazda A., Foit K., Hryniewicz P., Kost G.** (2011), The modular design of robotic workcells in a flexible production line, IOP *Conf. Series: Materials Science and Engineering*, 95, 012099.
3. **Bruni S., Vinolas J., Berg M., Polach O., Stichel S.** (2011), Modelling of suspension components in a rail vehicle dynamics context, *Vehicle System Dynamics*, 49(7), 1021-1072.
4. **Buchacz A., Banas W., Placzek M.** (2015), Influence of the excitation parameters of the mechanical subsystem on effectiveness of energy harvesting system, *IOP Conference Series-Materials Science and Engineering*, 95, 012052.
5. **Buchacz A., Galeziowski D.** (2012), Synthesis as a designing of mechatronic vibrating mixed systems, Journal of Vibroengineering, 14(2), 553 -559.

DOI 10.1515/ama-2017-0032

6. **Buchacz A., Placzek M., Wrobel A.** (2014), Modelling of passive vibration damping using piezoelectric transducers – the mathematical model, *Eksploatacja i Niezawodnosc – Maintenance and Reliability*, 16(2), 301-306.
7. **Connolly D.P., Kouroussis G., Giannopoulos A., Verlinden O., Woodward P.K., Forde M.C.** (2014), Assessment of railway vibrations using an efficient scoping model, *Soil Dynamics and Earthquake Engineering*, 58, 37-47.
8. **Grebowski K., Zielinska M.** (2015), Modelling of dynamic interactions of Pendolino train type on structures of historic railway bridges in Poland, *Przeglad Budowlany*, 1, 27-32.
9. **Gwiazda A., Herbuś K., Kost G., Ociepka P.** (2015), Motion analysis of mechatronic equipment considering the example of the Stewart platform, *Solid State Phenomena*, 220/221, 479-484.
10. **Hecht M.** (2009), Wear and energy-saving freight bogie designs with rubber primary springs: principles and experiences, *Proceedings of the Institution of Mechanical Engineers Part F: Journal of Rail and Rapid Transit*, 223(2), 105-110.
11. **Herwig A., Bruhwiler E.** (2011), In-situ dynamic behaviour of a railway bridge girder under fatigue causing traffic loading, *Proceedings of the 11th International Conference on Applications of Statistics and Probability in Civil Engineering*, 389-395.
12. **Jamroziak K., Bocian M., Kulisiewicz M.** (2013), Effect of the attachment of the ballistic shields on modelling the piercing process, *Mechanics*, 19(5), 549-553.
13. **Jamroziak K., Bocian M., Kulisiewicz M.** (2013), Energy consumption in mechanical systems using a certain nonlinear degenerate mode, *J. of Theor. and Appl. Mechanics*, 51(4), 827-835.
14. **Jönsson P.A., Stichel S., Persson I.** (2008), New simulation model for freight wagons with UIC link suspension, *Vehicle System Dynamics*, 46, 695-704.
15. **Klarecki K., Rabsztyn D., Hetmanczyk M.** (2015), Analysis of pulsation of the sliding-vane pump for selected settings of hydrostatic system, *Eksploatacja i Niezawodnosc – Maintenance and Reliability*, 17(3), 338-344.
16. **Kovalev R., Lysikov N., Mikheev G., Pogorelov D., Simonov V., Yazykov V., Zakharov S., Zharov I., Goryacheva I., Soshenkov S., Torskaya E.** (2009), Freight car models and their computer-aided dynamic analysis, Multibody System Dynamics, 22(4), 399-423.
17. **Mehrpouya M., Ahmadian H.** (2009), Estimation of applied forces on railway vehicle wheelsets from measured vehicle responses, *International Journal of Vehicle Structures and Systems*, 1(4), 104-110.
18. **Monica Z.** (2015), Optimization of the production process using virtual model of a workspace, I*OP Conf. Series: Materials Science and Engineering*, 95, pages.
19. **Oleszak P., Ciesla J., Szaniec W.** (2013), Study of the effects of side impacts on railway viaduct lying on the arc, *Budownictwo i Architektura*, 12(2), 47-54 (in Polish).
20. **Paprocka I., Kempa W., Grabowik C., Kalinowski K.** (2014), Predictive and reactive scheduling for a critical machine of a production system, *Advanced Materials Research*, 1036, 909-914.
21. **Placzek M.** (2015), Modelling and investigation of a piezo composite actuator application, *International Journal of Materials & Product Technology*, 50(3-4), 244-258.
22. **Placzek M., Buchacz A., Wrobel A.** (2015a), Use of piezoelectric foils as tools for structural health monitoring of freight cars during exploitation, *Eksploatacja i Niezawodnosc – Maintenance and Reliability*, 17(3), 443-449.
23. **Placzek M., Wrobel A., Baier A.** (2015b), Computer-aided strength analysis of the modernized freight wagon, *IOP Conference Series-Materials Science and Engineering*, 95, 012042.
24. **Rusinski E., Dragan S., Moczko P., Pietrusiak D.** (2012), Implementation of experimental method of determining modal characteristics of surface mining machinery in the modernization of the excavating unit, *Archives of Civil and Mechanical Engineering*, 12, 471-476.
25. **Stypula K.** (2009), Selected problems of surface building protection against vibrations generated by underground communication, *Gornictwo i Geoinzynieria*, 3(1), 351- 362 (in Polish).
26. **Tuma J.** (2009), Gearbox Noise and Vibration Prediction and Control, *Int. J. of Acoustic and Vibration*, 14(2), 99-108.
27. **Tuma J., Simek J., Skuta J., Los J., Zavadil J.** (2011), Active Vibration Control of Hydrodynamic Journal Bearings, *Springer Proceedings in Physics*, 139, 619-624.
28. **Wrobel A., Placzek M., Buchacz A., Majzner M.** (2015), Study of mechanical properties and computer simulation of composite materials reinforced by metal, *International Journal of Materials & Product Technology*, 50(3-4), 259-275.
29. http://www.ni.com/pdf/manuals/373779a_02.pdf (Access 22.03.2017)
30. http://www.ni.com/datasheet/pdf/en/ds-371 (Access 22.03.2017)
31. http://www.smart-material.com/MFC-product-main.html
(Access 22.03.2017)

The work was carried out under the project number PBS2/A6/17/2013 agreement implemented under the Applied Research Program, funded by the National Centre for Research and Development.

DE GRUYTER
OPEN

DOI 10.1515/ama-2017-0033 *acta mechanica et automatica, vol.11 no.3 (2017)*

DYNAMIC STRESS CONCENTRATION AT THE BOUNDARY OF AN INCISION AT THE PLATE UNDER THE ACTION OF WEAK SHOCK WAVES

Olena MIKULICH[*], **Vasyl' SHVABYUK**[*], **Heorhiy SULYM**[**]

[*]Department of Technical Mechanic, Lutsk National Technical University, 75 Lvivska st., Lutsk, 43018, Ukraine
[**]Bialystok University of Technology, ul. Wiejska 45C, 15-351 Bialystok, Poland

shypra@ukr.net, shvabyk@lutsk-ntu.com.ua, h.sulym@pb.edu.pl

received 21 June 2016, revised 18 September 2017, accepted 20 September 2017

Abstract: This paper proposes the novel technique for analysis of dynamic stress state of multi-connected infinite plates under the action of weak shock waves. For solution of the problem it uses the integral and discrete Fourier transforms. Calculation of transformed dynamic stresses at the incisions of plates is held using the boundary-integral equation method and the theory of complex variable functions. The numerical implementation of the developed algorithm is based on the method of mechanical quadratures and collocation technique. For calculation of originals of the dynamic stresses it uses modified discrete Fourier transform. The algorithm is effective in the analysis of the dynamic stress state of defective plates.

Key words: Stress State, Plate, Incision, Weak Shock Wave

1. INTRODUCTION

In metallurgy, machinery, construction and other industries a significant part of processes includes the presence of a variety of dynamic loads, which are caused by technological and mechanical processes. A variety of the dynamic loads are exerted in the structures of buildings by the wind and the seismic forces.

The dynamic loads result in the periodic changes of stresses. They may be within a single cycle, as a vibration or pulse packets, and a combination thereof. Dynamic load of any of these types may have a shock character.

The vibration-shock and shock loads can lead to the damage which cannot be explained by the excess of the yield stress or the accumulation of fatigue phenomena.

The use of the shock load by the ultrasound pulses has been effective in the study of the material defects. These methods are described in the book of Isbell (2005).

Sound pulses are transformed into shock waves, weak due to significant energy dissipation. The transition of shock waves through the domain of any defects, including cracks and pores, is accompanied with dispersing. Scattering of shock pulses gives essential information about the defect condition. Evaluation of diffraction parameters can predict the strength of the solid.

Dynamic stress state, which is occurred by the interaction of a shock wave scattered by the holes and incision in the plates differs from the case of quasi-static deformation.

In the literature, the study of dynamic stress state of the plates with holes was conducted by various methods.

In the works of Guz et al. (1978) and Kubenko (1967) the study of the distribution of dynamic stresses in the plate with a circular hole by the action of the shock load, which is applied to the boundary, is based on the Laplace transform with usage of the series method.

In the works of Benerjee (1994) and Brebbia et al. (1984) for the solving of the problems the singular integral equations are received by using the Laplace transform.

In the work of Popov at al. (2009) by using the Laplace transform it is studied the dynamic stress state of elastic bodies with inclusions.

In the works of Myhas'kiv et al. (2009) for the solution of dynamic problems for the bodies with inclusions and cracks it is used the finite-difference method in time and method of integral equations.

In the works of Ayzenberg-Stepanenko et al. (2012, 2013) with using finite-difference algorithms it is obtained the description of fronts and front zones with a minimal influence of spurious effects of numerical approximation.

By using a modified finite-difference method with respect to time and the method of Fourier series with respect to the angular variable in the works of Onyshko et al. (2015) it is got the time dependence of the dynamic stress concentration on the hole for plane dynamic problem of the theory of elasticity.

In the works of Pasternak et al. (2013) the study of dynamic stresses in the plates due to the antiplane deformation is conducted using the Fourier transform.

In the works of O. Mikulich (Shvabyuk et al., 2015) the method of study the stress concentration in the plates with holes and incisions for time-harmonic case is developed. This method is based on the application of the boundary integral equation method and the theory of function of complex variable. For the numerical calculation the methods of mechanical quadrature and collocation are used. Results of numerical calculations showed that the algorithm is effective for investigation of the action of time-harmonic loads.

DOI 10.1515/ama-2017-0033

2. SOLUTION OF THE PROBLEM

2.1. Statement of the problem

In applying of the Fourier transform it is existed the following relation between original and transformed function:

$$\tilde{f}(x,\omega)=\int_{-\infty}^{\infty} f(x,t)e^{-i\omega t}dt,$$
$$f(x,t)=\frac{1}{2\pi}\int_{-\infty}^{\infty}\tilde{f}(x,\omega)e^{i\omega t}d\omega. \quad (1)$$

This paper applies the Fourier transform (1) to study of the dynamic stress state of infinite plate with an incision.

Consider the equation of the motion of the isotropic plate written for displacements (Brebbia et al., 1984):

$$(c_1^2-c_2^2)u_{i,ij}-c_2^2u_{j,ii}+b_j=\frac{\partial^2 u}{\partial t^2}, \quad (2)$$

where: $\mathbf{u}(\mathbf{x},t)=\{u_j(\mathbf{x},t)\}, j=1;2$ is the vector of the displacement of the point $\mathbf{x}=\{x_1,x_2\}$, $c_1^2=\frac{\mathrm{E}}{\rho(1-\nu^2)}$, $c_2^2=\frac{\mathrm{E}}{2\rho(1+\nu)}$ are speeds of expansion and shear waves, E is the Young's modulus, ρ is the density of the material; ν is the Poisson ratio, $\mathbf{b}=\{b_j\}$ is the vector of mass forces, $i=1;\ 2$, $(\,)_{,j}$ means for differentiation with respect to x_j, t is time.

Applying transform (1) to equation (2) one obtain

$$(c_1^2-c_2^2)\tilde{u}_{i,ij}-c_2^2\tilde{u}_{j,ii}+\tilde{b}_j+\omega^2\tilde{u}_j=0, \quad (3)$$

where:
$\tilde{u}_j=\int_{-\infty}^{\infty}u_j(x,t)e^{-i\omega t}dt,\quad \tilde{b}_j=\int_{-\infty}^{\infty}b_j(x,t)e^{-i\omega t}dt.$ This equation is equivalent to the equation of time-harmonic motion with a cyclic frequency ω (Brebbia et al., 1984).

This approach allows conducting the research in the field of transforms of displacements; thereby the effect of the time factor is isolated.

Consider the case when incident weak shock wave is scattered by the incision at the plate. This weak shock wave is similar to (Gruber at al., 2013), which is given by the potential in the form:

$$\phi(\mathbf{x},t)=\begin{cases}\phi_0 f\left(\frac{\mathbf{x}}{a}-c_1\frac{t}{a}\right), & t\geq 0,\\ 0, & t<0;\end{cases}\quad \psi(\mathbf{x},t)=0.$$

Here ϕ_0 is a constant (Gruber et al., 2013), a is a characteristic of length. Applying transform (1) to this formula leads to

$$\tilde{\phi}(\mathbf{x},t)=\widetilde{\phi_0}\frac{a}{c_1}\tilde{f}\left(\frac{\omega a}{c_1}\right)e^{-k_1\mathbf{x}};\ \tilde{\psi}(\mathbf{x},t)=0, \quad (4)$$

where: $\tilde{f}(\omega)=\int_{-\infty}^{\infty}f(t)e^{-i\omega t}dt.$

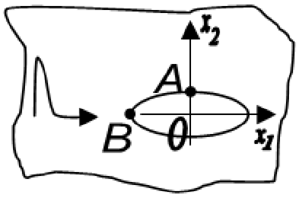

Fig. 1. Model of the plate

In further studies modulation of impulse from the time is chosen in the form of weak shock waves (Pasternak et al., 2013): $f(t)=p_*t^{n_*}e^{-\alpha_* t}, t>0, n_*\geq 0,$

where: $\tilde{f}(\omega)=p_*(n_*)!\,(\alpha_*+i\omega)^{-n_*-1}.$

Consider an infinite plate with an incision that is under the weak shock wave (4) (Fig. 1). The problem consists in determination of the dynamic stresses at the boundary of incision at the plate.

The centre of gravity of the plate is placed at the origin of a Cartesian coordinate system $Ox_1\mathrm{x}_2$. Symbol D denotes the domain occupied by the plate, and L is the boundary of the domain D.

The boundary conditions of the problem are written as (Brebbia et al., 1984):

$$\sigma_n|_L=\Phi_1(\mathbf{x},t),\ \tau_{sn}|_L=\Phi_2(\mathbf{x},t), \quad (5)$$

where: $\Phi_1(\mathbf{x},\mathrm{t}),\Phi_2(\mathbf{x},\mathrm{t})$ are the predetermined functions. Applying the Fourier transform (1) to the boundary conditions (5) leads to

$$\tilde{\sigma}_n|_L=\widetilde{\Phi_1}(\mathbf{x},\omega),\ \tilde{\tau}_{sn}|_L=\widetilde{\Phi_2}(\mathbf{x},\omega). \quad (6)$$

2.2. Integral equations of the problem

For the plane stress state the potential solution for transforms of displacements is selected as (Bonnet, 1995):

$$\tilde{u}_j(\mathrm{x},\omega)=\int_L p_i(\mathbf{x}^0,\omega)U_{ij}^*(\mathbf{x},\ \mathbf{x}^0,\omega)ds, \quad (7)$$

where $p_1,\ p_2$ are unknown complex potential functions. Integration along the boundary is performed within variables x_1^0,x_2^0, where $\mathbf{x}^0=\{x_1^0,x_2^0\}$. The representation of the images U_{ij}^* should be choosing with the regard to Zommerfeld radiation condition, since the plate is infinite. It has the form (Brebbia et al., 1984):

$$U_{ij}^*=\frac{1}{2\pi\rho c_2^2}\left(\psi\delta_{ij}-\chi\cdot r_ir_j\right), \quad (8)$$

where:

$$\psi=K_0(k_2r)+\frac{1}{k_2r}\left(K_1(k_2r)-\frac{c_2}{c_1}K_1(k_1r)\right);$$
$$\chi=K_2(k_2r)-\left(\frac{c_2}{c_1}\right)^2K_2(k_1r),$$

$r_j=\frac{\partial r}{\partial x_j}$, $r=\sqrt{(x_1-x_1^0)^2+(x_2-x_2^0)^2}$, $k_j=\frac{i\omega}{c_j}$, $K_m(r)$ are Bessel functions of the third kinds, $j=1,2,\ m=0,1,2.$

For determination of unknown boundary functions $p_1,\ p_2$ the calculation of stresses at an arbitrary point of the plate are performed by the formula (Savin, 1968):

$$\tilde{\sigma}_n=\frac{\sigma_{11}+\sigma_{22}}{2}+\frac{1}{2}\left(e^{-2i\alpha}\left(\frac{\sigma_{11}-\sigma_{22}}{2}+i\sigma_{12}\right)+e^{2i\alpha}\left(\frac{\sigma_{11}-\sigma_{22}}{2}-i\sigma_{12}\right)\right);\ \tilde{\tau}_{sn}=\frac{i}{2}\left(e^{2i\alpha}\left(\frac{\sigma_{11}-\sigma_{22}}{2}-i\sigma_{12}\right)-e^{-2i\alpha}\left(\frac{\sigma_{11}-\sigma_{22}}{2}+i\sigma_{12}\right)\right), \quad (9)$$

where: α is the angle between the normal $\vec{n}$ to the boundary of the plate and the axis Ox_1.

Substituting the representation for displacements (7) in the formulas (9), we obtain formulas for determining stresses at the boundary of the plate:

$$\tilde{\sigma}_n=\int_L f_1(z,\zeta)qd\zeta+\int_L f_2(z,\zeta)\overline{q}d\overline{\zeta};$$
$$\tilde{\tau}_n=\int_L \mathrm{g}_1(\mathrm{z},\zeta)\mathrm{q}d\zeta+\int_L \mathrm{g}_2(\mathrm{z},\zeta)\overline{\mathrm{q}}d\overline{\zeta}, \quad (11)$$

where: $q = \frac{ipds}{dt}$ is an unknown function, which had to be determined, $\zeta = \mathrm{x}_1^0 + \mathrm{ix}_2^0$, $f_k(z,\zeta)$, $g_k(z,\zeta)$, $k = 1, 2$ are known functions, which contain Bessel functions of third kind and are obtained similarly to those in Mikulich (2016).

Integration of functions $f_k(z,\zeta)$, $g_k(z,\zeta)$, $k = 1,2$ for small values of the argument leads to singularity. To establish their characteristics we use the asymptotic expressions for the Bessel functions of the third kind for small values of the argument (Cohen, 2007).

Let us perform the limiting transition when $(x_1, x_2) \to L$ in the last formula according to Plemelj-Sokhotski formulas (Savin, 1968). Consequently, integral equations for determination of the unknown functions q and $\overline{q}$ for given loading at the boundary are obtain:

$$Re\left(\frac{q}{2}\right) - Im\left(A_1\int_L \frac{qd\zeta}{z-\zeta} + \frac{dz}{d\bar{z}}\left(A_2\int_L \frac{\bar{q}d\bar{\zeta}}{z-\zeta} + A_3\int_L \frac{(\bar{z}-\bar{\zeta})qd\zeta}{(z-\zeta)^2}\right)\right) +$$

$$+\int_L f_1^R(z,\zeta)qd\zeta + \int_L f_2^R(z,\zeta)\overline{q}d\overline{\zeta} = \widetilde{\Phi_1}(\mathbf{x},\omega); \qquad (12)$$

$$Im\left(\frac{q}{2}\right) - Re\left(\frac{dz}{d\bar{z}}\left(A_2\int_L \frac{\bar{q}d\bar{\zeta}}{z-\zeta} + A_3\int_L \frac{(\bar{z}-\bar{\zeta})qd\zeta}{(z-\zeta)^2}\right)\right)$$

$$+\int_{\mathrm{L}} \mathrm{g}_1^{\mathrm{R}}(\mathrm{z},\zeta)\mathrm{qd}\zeta + \int_{\mathrm{L}} \mathrm{g}_2^{\mathrm{R}}(\mathrm{z},\zeta)\overline{\mathrm{q}}\mathrm{d}\overline{\zeta} = \widetilde{\Phi_2}(\mathrm{x},\omega),$$

where: $A_i, i = 1..3$ are constants, that in the case of plane stress state are as follows $A_1 = \frac{1+\nu}{4\pi\nu}$; $A_2 = \frac{3-\nu}{4\pi}$; $A_1 = \frac{1+\nu}{4\pi}$, ν is a Poisson's ratio, functions $f_1^R, f_2^R, g_1^R, g_2^R$ are known and regular (Mikulich, 2016).

2.3. Numeric solution algorithm

For calculation of the dynamic stresses at the infinite plate with incision the algorithm (Shvabyuk et al., 2016) is applied. The incision in the plates is modeled as an elliptic hole with axis ratio of 10.

Replacing the integrals at the system of integral equations (12) with the specified quadrature formulas (Eshkuvatov et al., 2009), the system of linear algebraic equations for determination of the nodal values of unknown boundary functions q and $\overline{q}$ is obtained:

$$\frac{q_s+\bar{q}_s}{4} + h\sum_{n=1}^{N} f_{1sn}q_n\psi'_n + h\sum_{n=1}^{K} f_{2sn}\bar{q}_n\overline{\psi}'_n = \widetilde{\Phi}_{1s},$$

$$\frac{q_s-\bar{q}_s}{4i} + h\sum_{n=1}^{N} g_{1sn}q_n\psi'_n + h\sum_{n=1}^{K} g_{2sn}\bar{q}_n\overline{\psi}'_n = \widetilde{\Phi}_{2s}, \quad (13)$$

where: $\psi = \psi(\theta)$, $0 < \theta < 2\pi$ is a set of parametric boundary equations, $f_{jsn} = f_j(\zeta_n, z_s), g_{jsn} = g_j(\zeta_n, z_s), j = 1, 2;$ $z_s = \psi(\theta_s)$, $\zeta_n = \psi(\theta_n)$, $\theta_n = nh$, $\theta_s = \theta_n + \frac{h}{2}, h = \frac{2\pi}{N}$, N is a set of points of the partition boundaries, $\widetilde{\Phi}_{1s}, \widetilde{\Phi}_{2s}$ are known functions, which are determined by (4).

After determination of the unknown functions, dynamic stresses of the plate are calculated by dependencies, which are obtained in accordance with representation (7) by providing singular components in the kernels of equations and consequently using Plemelj-Sokhotski formulas:

$$\tilde{\sigma}_{\theta s} = \frac{q_s+\bar{q}_s}{4} + h\sum_{n=1}^{N} y_{1sn}q_n\psi'_n + h\sum_{n=1}^{K} y_{2sn}\bar{q}_n\overline{\psi}'_n +$$

$$+G_{2s}, \qquad (14)$$

where: $y_{jsn} = y_j(\zeta_n, z_s)$, $j = 1, 2;$ G_{2s} is a known function, which is determined as a potential of reflected wave by (4).

For determination of the original of calculated dynamic stresses it is used the type of representation received from (1):

$$\sigma_\theta(x,t) = \frac{1}{2\pi}\int_{-\infty}^{\infty} \widetilde{\sigma_\theta}(x,\omega)e^{i\omega t}d\omega.$$

At numeric calculations of unknown quantities it can be implemented based on the discrete Fourier transform, which proved effectiveness in the calculations for antiplane deformation (Pasternak at al., 2013). A transforms of mentioned hoop stresses are complex. For calculation of originals of the dynamic stresses it is used a modified discrete Fourier transform:

$$\sigma_\theta(t_k) =$$
$$\frac{1}{T}\left(\sum_{n=-K}^{K-1} \tilde{\sigma}_\theta(\omega_n)\, exp\left(2\pi i\frac{nk}{K}\right) - \sum_{n=-K}^{K-1} \tilde{\sigma}_\theta(\omega_n)\right), \qquad (15)$$

where: $t_k = \frac{kT}{K}$, $k = -K..K-1$, T is time of weak shock wave propagation, K is a number of elements of discrete sample, $\omega_n = \frac{2\pi n}{T}$ are frequency of sample. To optimize the numerical calculations by the formula (15) fast discrete Fourier transform (Ramamohan at al., 2010) is used, where the number of elements is chosen as follows $K = 2^m$, m is a positive integer. The calculations are performed for dimensionless time parameter $\mathcal{T} = t\frac{c_1}{a}$.

2.4. Numeric calculation of stresses in the plate

Let's study the dynamic stress state of the plate with incision from the actions of a weak shock wave. Potential of the waves is written as (4) with pulse duration $t = 1\ s$. At numerical calculations the parameters of the shock wave at formula (4) are chosen as $\alpha^* = 10, p^* = 185, n^* = 2$.

The incision is modelled as an elliptical hole with axes a and $0.1a$. At the calculations, it was assumed that the wave front is directed along the axis Ox_1. The study is conducted for the dimensionless time parameter $\mathcal{T} \in \left(0, \frac{Tc_1}{a}\right), T = 4\ s$. For additional testing of the algorithm the center of incision is shifted along the axis at a distance $\mathcal{T}_0 = T_0\frac{c_1}{a}, T_0 = 2\ s$. In this case, before the wave reaches the boundary of incision ($\mathcal{T}_* = T_*\frac{c_1}{a}, T_* = 1\ s$) dynamic stresses should be zero.

Since derived from the formula (15) the values of the originals of dynamic stresses σ_θ are complex in general, the results of numerical calculations graphically presents both real and imaginary values of dynamic circular stresses $\sigma_\theta^R = Re(\sigma_\theta)$, $\sigma_\theta^I = \mathrm{Im}(\sigma_\theta)$. Since the potential (4) is selected to be a complex one, real and imaginary parts of stresses correspond to the real and imaginary parts of complex loading given by (4).

Fig. 2 shows the change of the real and imaginary values of the dynamic stresses related to σ_0, which are calculated at the points A and B of the boundary. Here and in further calculations the value of σ_0 is chosen to be 1.

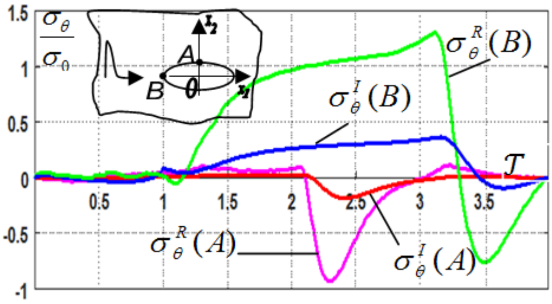

Fig. 2. Effects of weak shock waves on the incision at the plate

Fig. 2 shows that the dynamic stresses at the point B start growing at time $\mathcal{T}_* = T_* \frac{c_1}{a}, T_* = 1\,s$, when the shock wave reaches the semi-major axis of the incision. This is because the incision itself becomes the stress concentrator due the waves reflected from its boundary. This phenomenon is consistent with the principle of Huygens-Fresnel. Wave dissected by the heterogeneity propagates along the boundary of the incision, and the reflected wave portion extends from the boundary of the incision. At time $\mathcal{T}_{**} = T_{**} \frac{c_1}{a}, T_{**} = 3\,s$ the shock wave reaches the right border of the incision. Increasing of stresses at the boundary of incision at time $\mathcal{T}_r = T_r \frac{c_1}{a}, T_r = 3.5\,s$ is associated with the effect of the reflected wave. The intensity of the dynamic stresses decreases at $\mathcal{T}_e = T \frac{c_1}{a}, T = 4\,s$, when shock wave passes through the incision and is damped by reflected waves.

The reliability of the calculations is confirmed with the fact that the dynamic stresses are close to zero until the weak shock wave achieve the boundary of incision.

For a complete study of the dynamic stress state of the plate with an incision the time distributions of the absolute value of stresses for the interval of dimensionless time parameter $\mathcal{T}_* \in \left(2\frac{c_1}{a};\ 3\frac{c_1}{a}\right)$ are studied. The calculation results for the step $\Delta\mathcal{T}_* = 0.2\frac{c_1}{a}$ are shown in Fig. 3.

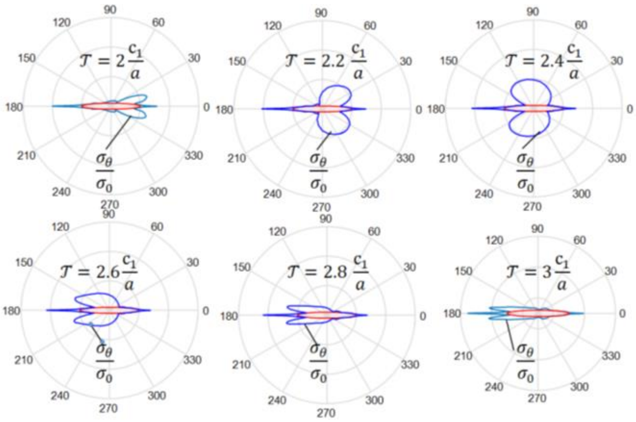

Fig. 3. Time slices of dynamic stresses distributions in the plate

Fig. 3 shows the effect of a weak shock wave at the incision accompanied by a reflected wave that moves along the boundary of the incision and causes a local increase in stresses in the plate. This reflected wave fades quickly and reduces its intensity.

Let's study the influence of weak shock waves with two successive pulses with duration $t = 1\,s$ on the stress state of the plate with the incision. The study is held for the case when the first shock impulse is induced at time parameter $\mathcal{T} = 0$, and the second is at $\mathcal{T}_1 = T_1 \frac{c_1}{a}, T_1 = 1\,s$. Shock pulses have the same intensity. Research is conducted for the dimensionless time parameter $\mathcal{T} \in \left(0,\ T\frac{c_1}{a}\right), T = 4\,s$.

For the mathematical setting of shock loads one can apply the time-shifting theorem and linearity theorem for the Transform (4) (Ramamohan at al., 2010). At numerical calculations the parameters of both pulses of the shock wave are chosen as $\alpha^* = 10$, $p^* = 185$, $n^* = 2$.

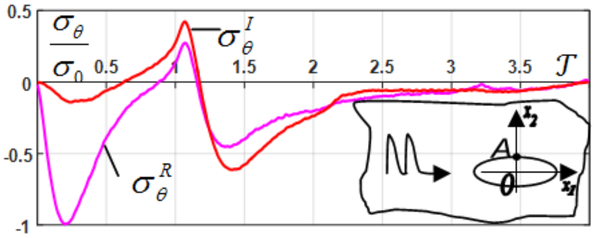

Fig. 4. The action of the weak shock waves with two pulses on the incision in the plate

Fig. 4 shows that dynamic stresses at the point A start growing at time $\mathcal{T} = 0$ due to the effects of the first shock wave pulse. The action of the second pulse at the moment of time parameter $\mathcal{T}_1 = 1\frac{c_1}{a}$ is imposing forward and backward from the right side of the boundary of incision of the waves. This leads to decrease of the intensity of dynamic stresses. Further action of reflected waves doesn't cause a significant increase in dynamic stresses.

Let's study the influence of intensity of pulses of weak shock wave to dynamic stress state of the plate with the incision. Calculations are held for the case of the weak shock wave in the form of two pulses of varying intensity and duration.

The first pulse lasts $t = 1\,s$. The second pulse is twice weaker than the first and lasts twice longer. The study is held for the case when the first shock pulse is induced at time $\mathcal{T}_0 = 0$, and the second is at $\mathcal{T}_1 = T_1 \frac{c_1}{a}, T_1 = 2\,s$. For the mathematical setting of shock loads one can apply the time-shifting theorem and linearity theorem of the transform (4) (Ramamohan at al., 2010). In numerical calculations the parameters of the shock waves have been identified as (4) at $\alpha * = 10, p * = 185, n * = 2$ for the first pulse and $\alpha * = 5, p * = 23, n * = 2$ for the second. Research is conducted for the time parameter $\mathcal{T}_* \in \left(0;\ 8\frac{c_1}{a}\right)$.

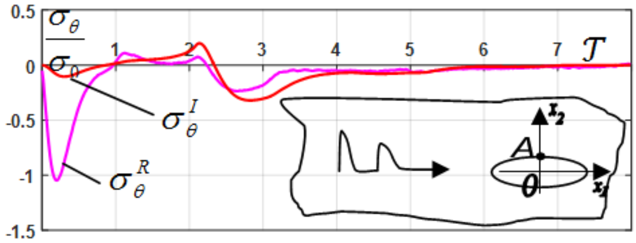

Fig. 5. Effects of weak shock waves with two pulses of varying intensity on incision at the plate

Fig. 5 shows that dynamic stresses at the point A start growing at time $\mathcal{T} = 0$ due to the effects of the first shock wave pulse. The action of the second pulse at $\mathcal{T}_1 = 2\frac{c_1}{a}$ is the imposition of the incident and reflected waves. This leads to increase in dynamic stresses $\mathcal{T} \in \left(2.2\frac{c_1}{a}, 4\frac{c_1}{a}\right)$. Further action of reflected waves doesn't cause a significant dynamic growth.

3. SUMMARY

The technique developed in this paper allows studying the dynamic stresses at the boundary of incisions in plates under the action of weak shock waves. Using Fourier transform of time-variable the dynamic problem reduces to a finite number of time-harmonic problems. To determine the original of dynamic stresses the formula of numerical Fourier inverse transform is modified.

Based on the numerical algorithm the dynamic stresses in the plate with incision for different cases of shock loading are calculated.

The advantage of the proposed algorithm is the ability of determination of the dynamic stresses along the entire boundary, and not at the only specific point. This makes it possible to investigate in details the dynamic stress state of defective plates.

REFERENCES

1. **Ayzenberg-Stepanenko M., Osharovich G., Sher E., Yanovitskaya Z.** (2012) Numerical Simulation of Shock-wave Processes in Elastic Media and Structures. Part I: Solving Method and Algorithms, *Journal of Mining Science,* 48(1), 76–95.
2. **Ayzenberg-Stepanenko M., Sher E., Osharovich G., Yanovitskaya Z.** (2013) Numerical Simulation of Shock-wave Processes in Elastic MEDIA and structures. Part II: Application Results, *Journal of Mining Science*, 48(5), 839–855.
3. **Banerjee P.** (1994) *Boundary Element Method in Engineering Science,* McGraw Hill, New York, London.
4. **Bonnet M.** (1995), *Integral Equations and Boundary Elements. Mechanical Application of Solids and Fluids, (in French)*, CNRS Éditions / Éditions EYROLLES, Paris.
5. **Brebbia C., Telles J., Wrobel L.** (1984), *Boundary Element Techniques,* Springer, New York.
6. **Cohen H.** (2007) *Number Theory Volume II: Analytic and Modern Tools***,** Springer, New York.
7. **Eshkuvatov Z. K., Nik Long N. M. A., Abdulkawi M.** (2009), Quadrature Formula for Approximating the Singular Integral of Cauchy Type with Unbounded Weight Function on the Edges, *Journal of Computational and Applied Mathematics*, 233, 334–345.
8. **Gruber S., Skews B.** (2013) Weak Shock Wave Reflection from Concave Surfaces, *Experiments in Fluids,* 54(1751), 1-14.
9. **Guz A.M. Kubenko V., Chernenko M.** (1978) *Diffraction of Elastic Waves,* Naukova Dumka, Kyiv.
10. **Isbell W.** (2005) *Shock Waves: Measuring the Dynamic Response of Materials,* Imperial College Press.
11. **Kubenko V.** (1967) Dynamic Stress Concentration Around an Elliptical Hole, *Reports of the Academy of Sciences USSR*, 3, 60-64.
12. **Mikulich O. A.** (2016) Dynamic Concentration of the Stresses Near the Holes in Infinity Plates under the Weak Shock Waves*, Naukovi notatky*, 53, 102-107.
13. **Mykhas'kiv V., Stankevych V., Zhbadynskyi I., Zhang Ch.** (2009) 3-D Dynamic Interaction Between a Penny-shaped Crack and a Thin Interlayer Joining Two Elastic Half-Spaces*, International Journal of Fracture,* 159(2), 137-149.
14. **Onyshko L., Senyuk M., Onyshko O (2015)** Dynamic Stress Concentration Factors in a Plane with Circular Hole Under the Action of Impact Nonaxisymmetric Loads**,** *Materials Science,* 50(5)*,* 755–761.
15. **Pasternak Ja., Sulym H., Pasternak R. (2013)** Dynamic Stress Concentration at Thin Elastic Inclusions under the Antiplane Deformation*, Physical and Mathematical Modeling and Information Technologies*, 18, 157-164.
16. **Popov V., Litvin O., Moysyeyenok A.** (2009) The Dynamic Problems About the Definition of Stress State Near Thin Elastic Inclusions Under the Conditions of Perfect Coupling, *Modern Analysis and Applications,* 191*, 485-498.*
17. **Ramamohan K.; D N Kim D.; Hwang J**. (2010) *Fast Fourier Transform: Algorithms and Applications,* Springer, New York.
18. **Savin G. N.** (1968) *Distribution of the Stresses near the Holes,* Naukova Dumka, Kyiv.
19. **Shvabyuk V., Sulym H., Mikulich O. (2015)** Stress State of Plate with Incisions under the Action of Oscillating Concentrated Forces, *Acta Mechanica et Automatica,* 9(3), 140-144.

DOI 10.1515/ama-2017-0034

SKY-HOOK CONTROL AND KALMAN FILTERING IN NONLINEAR MODEL OF TRACKED VEHICLE SUSPENSION SYSTEM

Andrzej JURKIEWICZ[*], **Janusz KOWAL**[*], **Kamil ZAJĄC**[*]

[*]Faculty of Mechanical Engineering and Robotics, AGH University of Science and Technology,
Al. A. Mickiewicza 30, 30-059 Kraków, Poland

jurkand@agh.edu.pl, jkowal@agh.edu.pl, kazajac@agh.edu.pl

received 10 October 2016, revised 19 September 2017, accepted 21 September 2017

Abstract: The essence of the undertaken topic is application of the continuous sky-hook control strategy and the Extended Kalman Filter as the state observer in the 2S1 tracked vehicle suspension system. The half-car model of this suspension system consists of seven logarithmic spiral springs and two magnetorheological dampers which has been described by the Bingham model. The applied continuous sky-hook control strategy considers nonlinear stiffness characteristic of the logarithmic spiral springs. The control is determined on estimates generated by the Extended Kalman Filter. Improve of ride comfort is verified by comparing simulation results, under the same driving conditions, of controlled and passive vehicle suspension systems.

Key words: Continuous Sky-Hook Control Strategy, Extended Kalman Filter, Military Vehicle, Nonlinear Model, Semi-Active Suspension System, Simulation

1. INTRODUCTION

Effective vibration damping of the hull of a tracked vehicle improves working conditions of vehicle crew, which affects the growth of conducting fire accuracy (Machoczek and Mężyk, 2015; Rybak et al., 2011). As a result, the success of combat operations can be indirectly dependent on properties of the suspension system. It stimulates the development of modern tracked vehicle systems. Nowadays, suspension structures use conventional passive systems and semi active or even active systems. Semi-active systems provide the ability to generate variable damping force and for this reason these systems are control systems. Their primary task is to reduce an impact of changes in shape of substrate on the chassis.

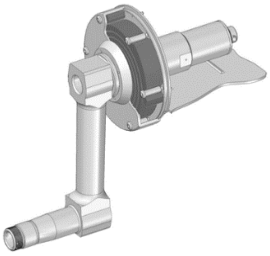

Fig. 1. The logharithmic spiral springs package of the modernized 2S1 tracked vehicle suspension system

Original version of 2S1 chassis is equipped with, ia. fourteen road wheels. The suspension system of each road wheels consists a rocker and a torsion bar (Fig. 1), which imparts stiffness in this system (Jurkiewicz et al., 2014; Nabagło et al., 2014). The torsion bar is considered as a relatively simple and reliable solution. The disadvantages of this component are reduction of space in the vehicle and reduction of vehicle resistance against anti-tank mines. In recent years, the project of modernization of the 2S1 suspension system has been performed. The torsion bars have been replaced by logarithmic shaped spiral springs. Damping properties were improved by the compression of oil by the coils of spiral springs. Unfortunately, the impact of control of oil pressure on the vibration transmission characteristics has proved to be insufficient. Based on this observation, the magnetorheological dampers in the theoretical model of 2S1 suspension system have been applied (Nabagło et al., 2015). The chamber of such damper is filled with magnetorheological fluid. This fluid exposed to magnetic field changes its state from free-flowing liquid to semi-solid state so the damping characteristic can be continuously controlled by proper changes of magnetic field (Bajkowski, 2012). One of the advantages resulting from the application of magnetorheological dampers in suspension systems is the possibility of adjusting the damping force to the current driving conditions and to the actual weight of the vehicle, which among others includes the mass of vehicle equipment.

The result of application magnetorheological dampers is semi-active system. Semi-active systems are used to control energy dissipation. For this reason, in this kind of systems it is possible to adopt control algorithms which provide an increase of the ride comfort. In case of military vehicles or special purpose vehicles the ride comfort significantly affects the quality of soldier's work (Jamroziak et al., 2013). The exposure of the human body to the vibrations could cause a muscular, sensory, intellectual and emotional fatigue or even health problems. It follows that the ride comfort is meaningful for the efficiency of operations on the battlefield. The main goal of this work was assumed on this basis. Researches are focused on the structure of a control system which guarantees an increase of the ride comfort.

In case of ride comfort oriented systems sky-hook control is widely used. Since 1974, the sky-hook control has been mostly used in automobile suspension systems (Lam and Liao, 2003; Simon and Ahmadian, 2001). In recent years, applications of this control in railway vehicles are also considered (Li and Goodall, 1999). Machoczek et. al. applies the sky-hook control theory in model of military multi-wheeled vehicle (2015). Evaluation of suspension is made by comparison of the displacement, velocity and acceleration amplitudes of vehicle hull, measured in the vertical direction. The authors indicate advantages resulting from the usage of semi-active suspension. Moreover, skyhook control algorithm with energy regenerative system has been studied by Sapiński et al. and Snamina et al. (2011, 2009). The interest of sky-hook control strategy is also observed in case of military vehicles. Nabagło et al. notes that sky-hook control strategy may improve ride comfort in tracked vehicles (2015). For purpose of this work, the continuous sky-hook control strategy was applied due to good results observed in so-called quarter-car model of the 2S1 suspension system. Researches have showed reduction of vertical velocity amplitude and increase of ride comfort, in relation to the model of 2S1 with passive suspension system. In this article, the nonlinearity of logarithmic spiral springs was considered in the continuous sky-hook control strategy formulation.

The continuous sky-hook control strategy depends on some state variables of the suspension system, such as the vertical velocity of the sprung mass and the vertical velocities of unsprung masses. The method, which produces the estimates of these unknown variables with high accuracy is the discrete Kalman filter. This algorithm, based on measurements of control signals and variables representing observable behaviour of the system determines the internal state. It is assumed, that in the theoretical model of the 2S1 suspension system the measured output variables are suspension deflections in first and last axles. The so-called half-car model was used in simulation research in this paper.

The application of magnetorheological dampers determine nonlinearity in equation of motion of the tested 2S1 suspension model. For this reason, the Extended Kalman Filter was considered as the appropriate way of state estimation (Julier and Uhlmann, 2004). The Extended Kalman Filter calculates current state on the basis of measurements of control signals and output variables representing observable behaviour of the system. In addition to the observation of a nonlinear system, this method minimizes the impact of disturbances which affect to control process and measurement process. Lindgärde as the main source of those disturbances gives interference that may be related to vibrations generated by the engine of the vehicle (2002). As an alternative measurement of relative velocity of the sprung mass and unsprung mass, Lindgärde uses differentiation of signal generated by suspension deflection sensor which are previously undergone conventional filtration by a low pass Butterworth filter. However, he argues, that the Kalman filter is preferred solution due to smaller estimation error.

The paper is organized as follows: in section II the 2S1 suspension system is described and the theoretical model with magnetorheological dampers is introduced. The continuous sky-hook control strategy which takes into account nonlinearity of logarithmic spiral spring is described in next section. Section IV is devoted to state estimation by the Extended Kalman Filter. In section V the results of simulation research are presented. Conclusions and observations are included in last section.

2. THE 2S1 SUSPENSION SYSTEM

The 2S1 platform is used in many military vehicles of Polish Land Forces among which may be mentioned about self-propelled mortar RAK, self-propelled howitzer M120G, armoured command staff and command vehicles. The original version of 2S1 vehicle suspension system uses torsion bars as parts introducing stiffness to the suspension system. Torsion bars have been popular after the Second World War. Stiffness characteristic of these elements is not progressively non-linear. The stiffness does not increase in a non-proportional way, during twisting of the torsion bar.

The modernization of the 2S1 suspension system includes the use of logarithmic spiral springs. Static characteristic of the logarithmic spiral spring is progressive nonlinear, which is shown in Fig. 2.b, is progressive nonlinear for large value of suspension deflection. It should be noted that this characteristic represents the results of laboratory measurements with the use of spring with thickness 3 [mm].

In addition to the progressivity, further advantage of suspension structure based on spiral springs in relation to the original suspension with torsion bars, is improvement of damping properties. This results from the presence of the oil in package of spiral springs. Control of oil pressure is another factor influencing the damping characteristics of the suspension.

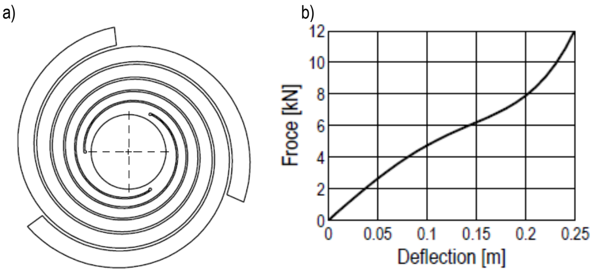

Fig. 2. Logarithmic spiral spring: a) shape of the spring; b) stiffness characteristic when oil pressure equals 0 [bar]

In order to perform simulation studies the static characteristic of logarithmic spiral spring was described by polynomial approximation of experimental data. It was assumed, that the static characteristic for negative deflection of suspension is a symmetry with respect to the origin. With such assumptions, the approximated function has the following form:

$$F_s(z_w) = k_{15}z_w^5 + k_{14}z_w^4 + k_{13}z_w^3 + k_{12}z_w^2 + k_{11}z_w \qquad (1)$$

where: F_s – approximation of spring force of logarithmic spiral spring, $k_{11}...k_{15}$ – approximation function coefficients, z_w – relative displacement of sprung mass and unsprung mass.

Fig. 1 shows the modified suspension with applied the package of logarithmic spiral springs. The theoretical model of the suspension has been enhanced with magnetorheological damper by Nabagło et al. (2015). Magnetorheological damper is characterized by low power consumption and fast response to changes of current value flowing through the electrical coil. However, this element causes great difficulties during designing process of control system due to the nonlinear dynamic (Spencer et al., 1997). Two magnetorheological dampers generate force which can be determined by the following Bingham model (Sapiński and Filuś, 2003):

DOI 10.1515/ama-2017-0034

$$F_{t1}=\frac{2}{\pi}(f_a+f_b i_1)arctg(pv_{11})+v_{11}(c_a+c_b i_1), \quad (2)$$

$$F_{t7}=\frac{2}{\pi}(f_a+f_b i_7)arctg(pv_{17})+v_{17}(c_a+c_b i_7). \quad (3)$$

In above equations, v_{11} and v_{17} are relative velocities between the damper pistons and the damper rods respectively. Quantities i_1 and i_7 are the electric current intensity signals. Elements $f_a+f_b i_1$ and $f_a+f_b i_7$ are Coulomb friction coefficients. Elements $c_a+c_b i_1$ and $c_a+c_b i_7$ describe the viscous friction coefficients.

Before formulating the theoretical model, following assumptions have been made. It was assumed that temperature does not affect magnetorheological fluid properties, as well as lack of leakage of this fluid. The nonlinear stiffness characteristic associated with spiral springs has been adopted. Linear stiffness and linear damping of road wheels were assumed. The sprung mass and unsprung masses were concentrated in points. Furthermore, bilateral constraints were assumed. It means that road wheels always have a contact with substrate. The theoretical model for such simplified structure of the 2S1 tracked vehicle suspension system (Fig. 2) is shown below. Equation of motion of unsprung mass in first axle has following form:

$$m_1\ddot{z}_1=F_{k21}+F_{c21}-F_{k11}-F_{t1}. \quad (4)$$

For unsprung masses in axles from the second to the sixth these equations are as follows (index i – axle number):

$$m_i\ddot{z}_i=F_{k2i}+F_{c2i}-F_{k1i}. \quad (5)$$

Equation for unsprung mass in the last axle:

$$m_7\ddot{z}_7=F_{k27}+F_{c27}-F_{k17}-F_{t7}. \quad (6)$$

Dynamics of vertical motion of the centre of gravity of the vehicle hull has been described in a manner as shown below:

$$m\ddot{z}=F_{t1}+F_{t1}+\sum_{j=1}^{7}F_{k1j}. \quad (7)$$

Dynamic equation of rotational motion of the vehicle hull around the pitch axis has been described by the following equations:

$$J_x\ddot{\varphi}_x=\sum_{j=5}^{7}l_jF_{k1j}-\sum_{j=1}^{4}l_jF_{k1j}+l_7F_{t7}-l_1F_{t1}. \quad (8)$$

Constants $k_{21}...k_{27}$ and $c_{21}...c_{27}$ are stiffness and damping coefficients of respective road wheels. J_x defines moment of inertia around the pitch axis. Constants $l_1...l_7$ expresses distance from the centre of gravity of the vehicle hull to further axles. Finally, quantity d is half of the vehicle hull width. Signals $g_1...g_7$ represent external excitation signals as road profile functions travelled by the vehicle road wheels. It can be therefore concluded that control of suspension system is an example of vibration isolation system. Variables $F_{k1}...F_{k7}$ are forces exerted by compressed logarithmic spiral springs being part of the 2S1 suspension system. According to (1) these forces can be described as follows:

$$F_{k1i}=F_s(z_{wi}) \quad (9)$$

where index i means number of vehicle axle so z_{wi} are relative displacements of sprung mass and unsprung masses. These variables, for first four axles, can be calculated according to the following equation:

$$z_{wi}=z-z_i+l_iz_i. \quad (10)$$

In next three axles of vehicle, the relative displacements of sprung mass and unsprung masses are described by:

$$z_{wi}=z-z_i-l_iz_i. \quad (11)$$

Prior to the formulation of state-space model based on equations (4) – (16) following state variables were assumed: $x_1...x_{14}$ – displacements and velocities of the unsprung masses; x_{15} and x_{16} – displacement and velocity of the sprung mass; x_{17} and x_{18} – angles and angular velocities around pitch axis. The electric current intensity signals i_1 and i_7 were described by control u_1 and u_2. The substrate profiles and derivatives of the road profile signals were assumed as control $u_3...u_{16}$. The state-space representation of the simplified 2S1 suspension system (Fig. 3) for such variables has form:

$$\begin{bmatrix}\dot{x}_1\\ \dot{x}_2\\ \dot{x}_3\\ \dot{x}_4\\ \dot{x}_5\\ \dot{x}_6\\ \dot{x}_7\\ \dot{x}_8\\ \dot{x}_9\\ \dot{x}_{10}\\ \dot{x}_{11}\\ \dot{x}_{12}\\ \dot{x}_{13}\\ \dot{x}_{14}\\ \dot{x}_{15}\\ \dot{x}_{16}\\ \dot{x}_{17}\\ \dot{x}_{18}\end{bmatrix}=\begin{bmatrix}x_2\\ \frac{1}{m_1}(F_{k21}+F_{c21}-F_{k11}-F_{t1})\\ x_4\\ \frac{1}{m_1}(F_{k21}+F_{c21}-F_{k11}-F_{t1})\\ x_6\\ \frac{1}{m_1}(F_{k21}+F_{c21}-F_{k11}-F_{t1})\\ x_8\\ \frac{1}{m_1}(F_{k21}+F_{c21}-F_{k11}-F_{t1})\\ x_{10}\\ \frac{1}{m_1}(F_{k21}+F_{c21}-F_{k11}-F_{t1})\\ x_{12}\\ \frac{1}{m_1}(F_{k21}+F_{c21}-F_{k11}-F_{t1})\\ x_{14}\\ \frac{1}{m_1}(F_{k21}+F_{c21}-F_{k11}-F_{t1})\\ x_{16}\\ m^{-1}\left(F_{t1}+F_{t1}+\sum_{j=1}^{7}F_{k1j}\right)\\ x_{18}\\ \frac{1}{J_x}\left(\sum_{j=5}^{7}l_jF_{k1j}-\sum_{j=1}^{4}l_jF_{k1j}+l_7F_{t7}-l_1F_{t1}\right)\end{bmatrix}. \quad (12)$$

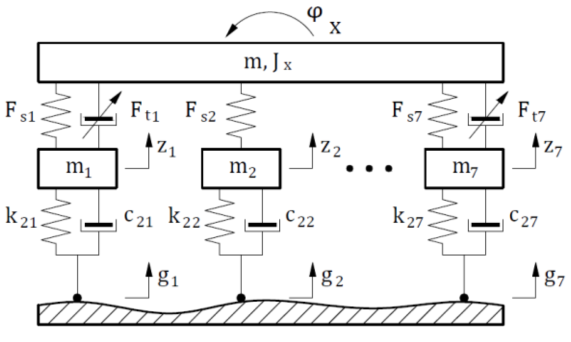

Fig. 3. Simplified model of the 2S1 suspension system where: F_{t1}, F_{t7} – forces generated by magnetorheological dampers; F_{s1} ... F_{s7} – forces generated by logarithmic spiral springs; k_{21} ... k_{27} and c_{21} ... c_{27} – stiffness and damping coefficients of road wheels; m, J_x – sprung mass and its moment of inertia; φ_x – angle of vehicle hull's rotational motion around pitch axis; z_1 ... z_7 – vertical displacements of unsprung masses; $g_1...g_7$ – external excitation signals of road profile functions

Above formula describes nonlinear multidimensional state-space system. Suspension deflections in axes of magnetorheological dampers were set as the measured output signals. The output matrix was adopted as:

$$\begin{array}{lc} H = & \begin{bmatrix} 1 & \cdots & 0 & \cdots & -1 & \cdots & +l_1 & 0 \\ 0 & \cdots & 1 & \cdots & -1 & \cdots & -l_7 & 0 \end{bmatrix}. \\ Col. & \begin{matrix} 1 & & 13 & & 15 & & 17 & 18 \end{matrix} \end{array} \tag{13}$$

Finally, the output equation has the form:

$$y = Hx \tag{14}$$

where: y is 2-dimensional vector of observable state variables and x is 18-dimensional state vector.

3. THE SKY-HOOK CONTROL STRATEGY

The sky-hook control has been proposed by Karnopp et al. (1974). In ideal case a viscous damper is connected with sprung mass and abstract sky which is fixed in stationary coordinate system. Such configuration reduces the vertical vibration of the sprung mass, which directly translates into increase of ride comfort. However, this configuration is not physically realizable. Application of an element, between sprung and unsprung masses, with controllable damping characteristic is a method to realize sky-hook control strategy. For purposes of this article the continuous sky-hook control strategy was applied in half-car model of the 2S1 tracked vehicle suspension system. The force generated by abstract viscous damper connecting the centre of gravity of the vehicle hull with inertial frame is defined as follows (Machoczek and Mężyk, 2015):

$$F_{sky} = \zeta_{sky} b_{cr} \dot{z}. \tag{15}$$

Parameter ζ_{sky} is a non-dimensionless quantity which in the case of critical damping is equal 1. Critical damping coefficient b_{cr} for the adopted model of the 2S1 suspension system has the following form:

$$b_{cr} = 2\sqrt{m\boldsymbol{K}} \tag{16}$$

where: $\boldsymbol{K}$ [N/m] is stiffness of logarithmic spiral springs. This parameter is specified in more details at the end of this chapter. Substitution of (16) to (15) gives force which abstract viscous damper should generate. To adopt the sky-hook control strategy, this force must be equal to the force produced by two magnetorheological dampers

$$\mathrm{F}_{t1} + \mathrm{F}_{t2} = 2\zeta_{sky} \dot{z} \sqrt{m\boldsymbol{K}}. \tag{17}$$

Because vibration control of the 2S1 suspension system is investigated only in vertical direction it was assumed that $\mathrm{F}_{t1} = \mathrm{F}_{t7}$. Hence, these forces are equal:

$$\mathrm{F}_{t1} = \mathrm{F}_{t2} = \zeta_{sky} \dot{z} \sqrt{m\boldsymbol{K}}. \tag{18}$$

This equation can be considered as a control law. To apply this law, it is necessary to introduce inverse models of magnetorheological dampers. The inverse of equations (2) – (3) due to variables i_1 and i_7 leads to:

$$i = \frac{\zeta_{sky} \dot{z} \sqrt{m\boldsymbol{K}} - 2\pi^{-1} f_a arctg(pv) - c_a v}{2\pi^{-1} f_b arctg(pv) + c_b v}. \tag{19}$$

Appropriate substitution of variables v_1 and v_7 to v leads to current intensity signals i_1 and i_7. The flow of electrical currents i_1 and i_7 through the windings of magnetorheological dampers should obtain the desired values of damping forces F_{t1} and F_{t7}. Variables i_1 and i_7 are the input variables of the state space model (12) designated as u_1 and u_7. Vertical velocity z of the sprung mass is state variable x_{16}. Variables v_1 and v_7 are relative velocities between the unsprung masses m_1, m_7 and sprung mass m. Therefore, following equations can be written:

$$v_1 = x_2 - x_{16} + l_1 x_{18}, \tag{20}$$

$$v_7 = x_{14} - x_{16} - l_7 x_{18}. \tag{21}$$

Since the stiffness characteristic of logarithmic spiral springs (1) is non-proportional to the suspension deflection, the stiffness parameter $\boldsymbol{K}$ is computed as a sum of proper slopes of tangent lines to the curve presented in Fig. 2.b. Modelled suspension system consists of seven springs with nonlinear stiffness characteristics so $\boldsymbol{K}$ could be described as:

$$\boldsymbol{K} = \textstyle\sum_{i=1}^{7} k_{1i}. \tag{22}$$

Each k_{1i} where $i = 1 \dots 7$ are slopes of tangent lines to the function (1) calculated in current value of deflections:

$$k_{1i} = \left[\frac{\partial F_S(z_w)}{\partial z_w}\right]_{z_{wi}}. \tag{23}$$

Substitution of the proper values of variables z_{wi}, which are showed in (10) and (11), leads to the stiffness parameter $\boldsymbol{K}$:

$$\boldsymbol{K} = \textstyle\sum_{i=1}^{7} \left[\frac{\partial F_S(z_w)}{\partial z_w}\right]_{z_{wi}}. \tag{24}$$

Finally, the inverse model of magnetorheological damper has the form:

$$i = \frac{\zeta_{sky} \dot{z} \sqrt{m \sum_{i=1}^{7} \left[\frac{\partial F_S(z_w)}{\partial z_w}\right]_{z_{wi}}} - 2\pi^{-1} f_a arctg(pv) - c_a v}{2\pi^{-1} f_b arctg(pv) + c_b v}. \tag{25}$$

Above equation is used to compute electric current intensity signals which control the magnetorheological dampers.

4. THE EXTENDED KALMAN FILTER

R. E. Kalman has presented modern idea of state estimation in 1960 at National Aeronautics and Space Administration (NASA) Ames Research Centre in Mountain View, California. The method of R. E. Kalman was considered as a possible solution to the problem of estimating trajectories of spacecraft which were intended to be used during manned flights to the Moon. In 1961, the research team led by Stanley F. Schmidt has conducted simulation study of navigation system taking into consideration the Kalman's method. Stanley F. Schmidt has introduced modifications in the standard algorithm to obtain possibly the most accurate approximations of the state vector in nonlinear system. The result of his work is the Extended Kalman Filter which is now the most widely used method of state estimation in nonlinear systems.

The Kalman Filter is a minimum mean-squared error estimator of the sate vector (Becerra et al., 2001; Julier and Uhlmann, 2004). It is a result of minimizing expected value of quadratic cost function $J = E[(x - \hat{x}_k)(x - \hat{x}_k)^T]$, where $x \in \mathcal{R}^n$ is a state vector and $\hat{x}_k \in \mathcal{R}^n$ is an estimator of this vector. Minimization of the cost function J leads to:

$$\hat{x}_k = E[x|Y_k]. \tag{26}$$

Y_k is a vector which has the form $[\mathrm{y}(\mathrm{t}_1), \mathrm{y}(\mathrm{t}_2), \dots, \mathrm{y}(\mathrm{t}_k)]$, where $\mathrm{y}(\mathrm{t}_i) \in \mathcal{R}^p$ for all $i \in \{1 \dots k\}$ are vectors of discrete system output. Above formula determines the direction of mean-squared estimation, which considers events related to the estimated parameter.

The process control and observed measurements in the 2S1 suspension system may be distributed due to noises. In the following, it is assumed that the process noise $w(t)$ is additive noise. The random excitations signals adopted as the additive process noise may be caused by air resistance or friction in contact between suspension elements. Their source may also be engine or other machinery of the vehicle equipment. The output vector $y(t)$ is measured by a sensor which is corrupted by an additive measurement noise $v(t)$ also. To apply standard algorithm of the Extended Kalman Filter, the random signals $w(t)$ and $v(t)$ are assumed as stationary random processes. Positive-definite, constant in time, the diagonal matrix $Q \in \mathcal{R}^{n\times n}$ is the covariance matrix of the process noise $w(t) \in \mathcal{R}^{n}$. Matrix $R \in \mathcal{R}^{p\times p}$ is a covariance matrix of measurement noise $v(t) \in \mathcal{R}^{p}$ and is also positive definite, constant in time and diagonal. The expected values $E[w(t)]$ and $E[v(t)]$ are equal to zero. Moreover, random vectors $w(t)$ and $v(t)$ are assumed as Gaussian white noise. Considering mentioned disturbances, the model described by equations (12) and (14) now has the following form (Becerra et al., 2001):

$$\dot{x}(t) = f(x(t), u(t)) + w(t), \tag{27}$$

$$y(t) = h(x(t)) + v(t). \tag{28}$$

And finally, it is assumed that the expected value $E[w(t)v(t)^T]$ is equal to zero matrix, which means that the process noise and measurement noise are not correlated.

Implementation of the Extended Kalman Filter in a digital control unit requires a discrete form of equations (27) and (28). These equations, using the definition of a derivative, assuming a step size Δ and $t = t_k$, take the from:

$$x(t_{k+1}) = f\big(x(t_k), u(t_k)\big)\Delta + w(t_k)\Delta + x(t_k), \tag{29}$$

$$x(t_{k+1}) = h\big(x(t_{k+1}), u(t_k)\big) + v(t_{k+1}). \tag{30}$$

The model (29) describes the so-called discrete-time Gauss-Markov random process. It follows from the fact, that $w(t)$ is additive Gaussian random vector. Whereas, the Markov property stems from the fact that system state at time t_k depends only on the state at the previous time t_{k-1}.

The Extended Kalman Filter is two-phase state estimation algorithm of non-linear dynamic system. The idea of this method is to linearize the non-linear system at a point in state-space whose coordinates specify current value of the estimator and to apply the linearized description to calculate next estimate (Julier and Uhlmann, 2004). The Extended Kalman Filter is first order approximation of the standard Kalman filter because the linearization is based on first order Taylor series expansion. Estimation process, which is determined by (26), has following structure:

$$\hat{x}(t_k|t_{k-1}) = f\big(\hat{x}(t_{k-1}|t_{k-1}), u(t_{k-1})\big)\Delta + \hat{x}(t_{k-1}|t_{k-1}), \tag{31}$$

$$P_{k|k-1} = A_{k-1}P_{k-1|k-1}A_{k-1}^T + Q, \tag{32}$$

$$K_k = P_{k|k-1}H_k^T\left[H_kP_{k|k-1}H_k^T + R\right]^{-1}, \tag{33}$$

$$\hat{x}(t_k|t_k) = \hat{x}(t_k|t_{k-1}) + K_k\left(y(t_k) - h\big(\hat{x}(t_k|t_{k-1})\big)\right), \tag{34}$$

$$P_{k|k} = [I - K_kH_k]P_{k|k-1}[I - K_kH_k]^T + K_kRK_k^T \tag{35}$$

where: $\hat{x}(t_k|t_{k-1})$ and $\hat{x}(t_k|t_k)$ are a priori and a posteriori estimators of the state vector and they are associated with prediction and update phase respectively. $P_{k|k-1}$ and $P_{k|k}$ are error covariance matrices of these estimators. The matrix K_k is called the Kalman gain. A_{k-1} is the matrix of partial derivatives of nonlinear function (27) with respect to vector x. For discrete system, it has form:

$$A_{k-1} = \left[I + \Delta\left[\frac{\partial f}{\partial x}\right]_{(\hat{x}(t_{k-1}|t_{k-1}),u(t_{k-1}))}\right]. \tag{36}$$

Finally, $H_k \in \mathcal{R}^{p\times n}$ is the matrix of partial derivatives of function (28) with respect to vector x. This matrix does not change its form since the output equation is linear:

$$H_k = H. \tag{37}$$

5. SIMULATION RESEARCH

In simulation research, which was carried out in MATLAB, following assumptions have been adopted. It was assumed, that the 2S1 tracked vehicle enters on elevation of height 0.1 [m] with velocity 0.832 [m/s]. In the first stage of study, the passive suspension was examined. In this case, values of electrical currents i_1 and i_7 flowing through the windings of magnetorheological dampers were set to 0 [A]. Values of damping forces of each magnetorheological damper result only from the relative displacements v_1 and v_7. In the next stage of study, the continuous sky-hook control strategy was tested. The control strategy is defined by equation (25).

Furthermore, the presence of disturbances affecting control process and measurement process was introduced. These disturbances were set as white noise. The Extend Kalman Filter was introduced to minimize their impact as the state estimator in passive case and in control case.

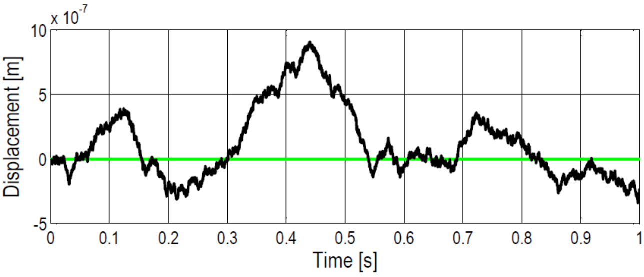

Fig. 4. Estimation of vertical displacement of the centre of the gravity of the vehicle hull and response of the system not affected by white noise

Fig. 4 shows the vertical displacement of the centre of gravity of the 2S1 tracked vehicle in which semi-active suspension is controlled by the continuous sky-hook control strategy. The graph shows the influence of the Extended Kalman Filter in the system affected by process noise and measurement noise. The graph shows also the response of the system in which process noise and measurement noise have not been introduced and the algorithm of Extended Kalman filter has not been used. Initialization of the algorithm requires assumptions about the initial value of a posteriori estimator and the initial value of a posteriori error covariance matrix. The estimator of the state is a random vector whose values are depended on the error covariance matrix. Increase of accuracy estimation results from update this matrix in each discrete step time.

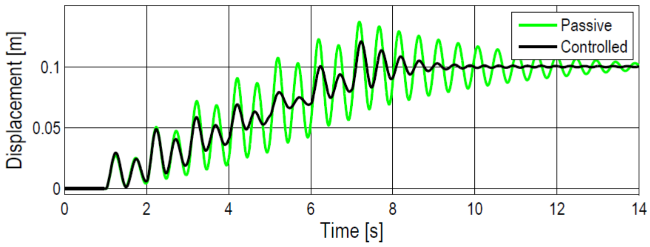

Fig. 5. Vertical displacement of the centre of the gravity of the vehicle hull in passive and controlled systems

The above Fig. 5 shows vertical displacement of the centre of the vehicle hull in passive suspension system and controlled suspension system. Fig. 6 is a comparison of the vertical velocity of the centre of the vehicle hull between passive suspension system and controlled suspension system, in which formulated continuous sky-hook control strategy was applied. Time-domain analysis show the advantage of proposed semi-active suspension system.

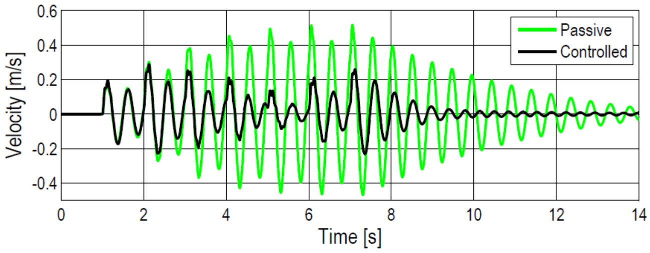

Fig. 6. Vertical velocity of the centre of the gravity of the vehicle hull in passive and controlled systems

In the following stage of the simulation research, two vibration transmissibility characteristics were made. The transmissibility characteristic is the key measure of quality of the vibration control system. Fig. 7 shows logarithmic transmissibility characteristics from the input u to the vertical displacement of the centre of the gravity of the vehicle hull, which is designed as x_{17}. It should be mentioned that the current values flowing through the windings of magnetoheological dampers can vary in range from 0 to 5 [A].

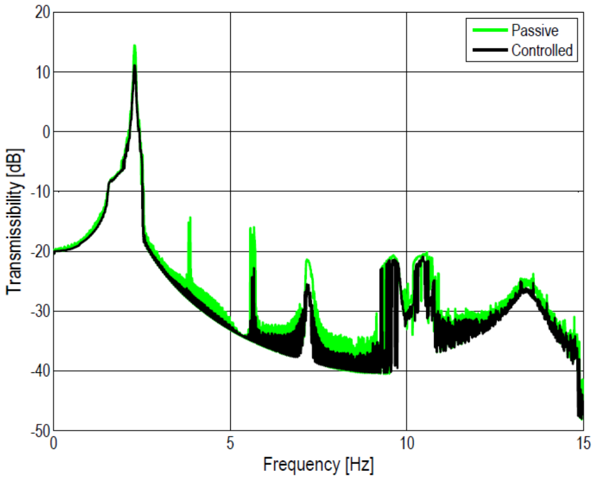

Fig. 7. Logarithmic vibration transmissibility characteristics of the tracked vehicle hull

To compare transmissibility function values in selected frequencies the following characteristic are introduced. The graph shows the result of dividing the value of the dimensionless transmissibility characteristic of passive system by the value of the dimensionless transmissibility characteristic of controlled system, which is finally multiplied by 100 [%].

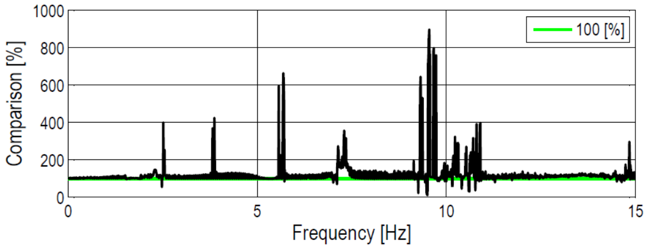

Fig. 8. Comparison of dimensionless transmissibility characteristic values in passive and controlled suspension system

6. CONCLUSION

Estimated state variables provide the possibility to control the 2S1 suspension model through the continuous sky-hook control strategy. On the basis on measurements of substrate profile and two physical variables, which are relative displacements between the damper pistons and the damper rods, eighteen state variables are estimated. The use of the Extended Kalman Filter brings many simplifications. The Extended Kalman Filter does not bring delays which occur in the case of conventional filtration where filters like Butterworth filter, Chebyshev filter etc. are applied. The problem may be implementation of this algorithm in digital control unit.

Time characteristics (Fig. 5, 6) indicate that the continuous sky-hook control strategy takes into account the nonlinearity of spiral springs reduces amplitudes of vertical displacement and vertical velocity of the centre of gravity of the vehicle hull and shortens the time needed to achieve the appropriate level. Comparison of vertical velocities of the vehicle with controlled suspension and with passive suspension leads to achieve the increase of ride comfort. Also, this can have a positive affect the function of gun stabilization system which means the increase in accuracy of conducting fire.

Vibration transmissibility characteristics, which are presented in Fig. 7, show that the continuous sky-hook control strategy is effective. The transmissibility characteristics in natural frequency of the vehicle hull have significantly lower values in case when the continuous sky-hook control strategy is applied. Also, it should be mentioned, that the proposed control strategy, in compare to passive suspension system leads to lower values of displacement amplitudes in range between natural frequencies of the sprung mass and unsprung masses. This fact is confirmed by the Fig. 8. It can be assumed, that there is an increase of ride comfort of the vehicle crew in whole range of frequency of excitation signal. In case of linear suspension model similar result was achieved by Laalej et al. (2012). During work over formulating sky-hook control strategy, the nonlinear characteristic of spiral spring has been considered in this article.

DOI 10.1515/ama-2017-0034

REFERENCES

1. **Bajkowski J. M.** (2012), Design, Analysis and Performance Evaluation of the Linear, Magnetorheological Damper, *Acta Mechanica et Automatica*, 6, 5-9.
2. **Becerra V. M., Roberts P. D., Griffiths G. W.** (2001), Applying the extended Kalman filter to systems described by nonlinear differential-algebraic equations, *Control Engineering Practice*, 9(3), 267-281.
3. **Jamroziak K., Kosobudzki M., Ptak J.** (2013), Assessment of the comfort of passenger transport in special purpose vehicles, *Eksploatacja i Niezawodność*, 15(1), 25-30.
4. **Julier S.J., Uhlmann J.K.** (2004), Unscented filtering and nonlinear estimation, *Proceedings of the IEEE*, 92(3), 401-422.
5. **Jurkiewicz A., Nabagło T., Kowal J., Apostoł M.** (2014), A new suspension system of an autonomous caterpillar platform, *Journal of Theoretical and Applied Mechanics*, 52(4), 857-867.
6. **Karnopp D., Crosby M. J., Harwood R. A.** (1974), Vibration control using semi-active force generators, *Journal of Engineering for Industry*, 96(2), 619-626.
7. **Laalej H., Lang Z. Q., Sapinski B., Martynowicz P.** (2012), MR damper based implementation of nonlinear damping for a pitch plane suspension system, *Smart Materials and Structures*, 21(4), 045006.
8. **Lam A. H. F., Liao W. H.** (2003), Semi-active control of automotive suspension systems with magneto-rheological dampers, *International Journal of Vehicle Design*, 33(1-3), 50-75.
9. **Li H., Goodall R. M.** (1999), Linear and non-linear skyhook damping control laws for active railway suspensions, *Control Engineering Practice*, 7(7), 843-850.
10. **Lindgärde O.** (2002). Kalman filtering in semi-active suspension control, *Proceedings of 15th IFAC World Congress*,1539-1544.
11. **Machoczek T., Mężyk A.** (2015), The multi-wheeled vehicle's suspension control (in Polish), *Przegląd Mechaniczny*, 1, 19-25.
12. **Nabagło T., Jurkiewicz A., Apostoł M., Micek P.** (2014), Simulation of 2S1 tracked vehicle model with modernized suspension system during crossing a single obstacle, *Solid State Phenomena*, Trans Tech Publications, 208, 140-147.
13. **Nabagło T., Jurkiewicz A., Kowal J.** (2015), Semi-active suspension system for 2S1 tracked platform in application of improvement of the vehicle body stability, *Applied Mechanics and Materials*, 759, 77-90.
14. **Rybak P., Borkowski W., Wysocki J., Hryciów Z., Michałowski B**. (2011), Model research of the light tank basing on multi-task combat platform (in Polish), *Szybkobieżne Pojazdy Gąsienicowe*, 2, 39-46.
15. **Sapiński B., Filuś J.** (2003), Analysis of parametric models of MR linear damper, *Journal of Theoretical and Applied Mechanics*, 41(2), 215-240.
16. **Sapiński B., Jastrzębski Ł., Węgrzynowski M.** (2011), Modelling of a self-powered vibration reduction system (in Polish), *Modelowanie Inżynierskie*, 10(41), 353-362.
17. **Simon D., Ahmadian M.** (2001), Vehicle evaluation of the performance of magneto rheological dampers for heavy truck suspensions, *Journal of Vibration and Acoustics*, Transactions of the ASME, 123(3), 365-375.
18. **Snamina J., Podsiadło A., Orkisz P.** (2009), Skyhook vibration control with energy regenerative system, *Mechanics*, 28, 124-130.
19. **Spencer Jr. B. F., Dyke S. J., Sain M. K., Carlson J.** (1997), Phenomenological model for magnetorheological dampers, *Journal of engineering mechanics*, 123(3), 230-238.

The work has been accomplished under the research project No. 15.11.130.429 financed by the grant of Faculty of Mechanical Engineering and Robotics

MAGNETOSTATIC ANALYSIS OF A PINCH MODE MAGNETORHEOLOGICAL VALVE

Janusz GOŁDASZ[*,**], **Bogdan SAPIŃSKI**[***]

[*]Cracow University of Technology, ul. Warszawska 24, 31-155 Kraków, Poland
[**]Technical Center Kraków, BWI Group, ul. Podgórki Tynieckie 2, 30-399 Kraków, Poland
[***]AGH University of Science and Technology, al. Mickiewicza 30, 30-059 Kraków, Poland

janusz.goldasz@bwigroup.com, deep@agh.edu.pl

received 15 May 2017, revised 20 September 2017, accepted 22 September 2017

Abstract: The study deals with the pinch mode of magnetorheological (MR) fluids' operation and its application in MR valves. By applying the principle in MR valves a highly non-uniform magnetic field can be generated in flow channels in such a way to solidify the portion of the material that is the nearest to the flow channel's walls. This is in contrary to well-known MR flow mode valves. The authors investigate a basic pinch mode valve in several fundamental configurations, and then examine their magnetic circuits through magnetostatic finite-element (FE) analysis. Flux density contour maps are revealed and basic performance figures calculated and analysed. The FE analysis results yield confidence in that the performance of MR pinch mode devices can be effectively controlled through electromagnetic means.

Key words: MR Fluid, Pinch Mode, Valve, Magnetostatic Model

1. INTRODUCTION

MR effect is manifested by changes in the material's apparent viscosity when it is exposed to magnetic field of sufficient magnitude (Jolly et al., 1996). The changes are controllable, fast and reversible. The feature has made the material attractive for use in vibration damping applications in particular. By considering the manner in which the material is operated, MR fluid based devices can be classified into four categories: flow-mode (Gołdasz and Sapiński, 2015, Simms et al., 2001, Yao et al., 2002), shear mode (Wereley et al., 2007), squeeze mode (Boelter and Janocha, 1998, Jolly and Carlson, 1996), pinch mode (Goncalves and Carlson, 2009). Hybrid devices utilize more than one operating mode of MR fluids (Yazid et al., 2014).

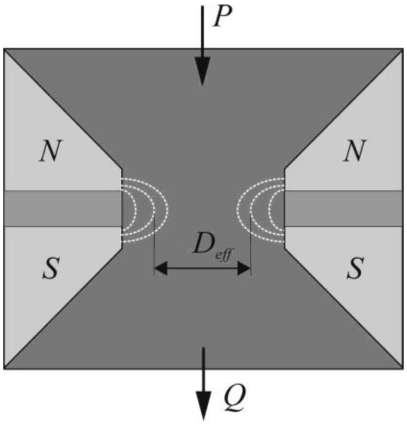

Fig. 1. Pinch mode valve concept (Goncalves and Carlson, 2009)

In this paper the so-called pinch mode is of interest. The recent invention of pinch mode valves as shown in Fig. 1 (Carlson et al., 2007) utilizes flow channels in which MR fluid is energized by a highly non-uniform magnetic field. The pressure at the inlet is P, and by varying the effective diameter Deff the inventors claimed the flow rate through the valve Q can be adjusted. The valve features a non-magnetic spacer that separates the magnetic poles. Hence, the magnetic flux is directed in parallel to the fluid flow direction. According to the inventors the valve can be operated in a manner similar to that of a controllable orifice via field induced yield stress modifications – the material is solidified near the walls of the channel it flows through. Effectively, most of the fluid flow may occur the relatively narrow zone in the middle of the flow channel – see Fig. 2. In the figure the areas with little or no flow are characterized by high yield stresses. However, the pinch mode devices have received the least research attention, and available data are scarce (Carlson et al., 2007, Goncalves and Carlson, 2009).

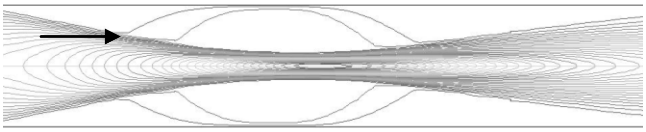

Fig. 2. Simulated MR fluid flow between parallel plates
and with high yield stress zones near channel walls

The purpose of this paper was to examine the steady-state performance of an MR valve that can be operated in pinch mode. The authors highlight several configurations of this valve, then proceed with a FE magnetostatic study of this device's model at various levels of the control coil current. The obtained results are then presented in the form of flux density contour maps and averaged flux density vs. current characteristics, respectively.

2. MR VALVE

The pinch mode valve is illustrated in Fig. 3. In the figure the numeric symbols indicate the key components of the valve. The valve is axi-symmetric. The core (1) houses the coil (2), the flow channel (3) and the non-magnetic spacer (4). The current in the coil induces the magnetic flux in the core assembly that passes the core, and is then directed into the flow channel. With this spacer-core-fluid arrangement the material is likely to solidify at areas near the flow gap walls. Contrary to flow mode valve, in pinch mode valves the flux passes the flow gap in the direction parallel to the fluid flow.

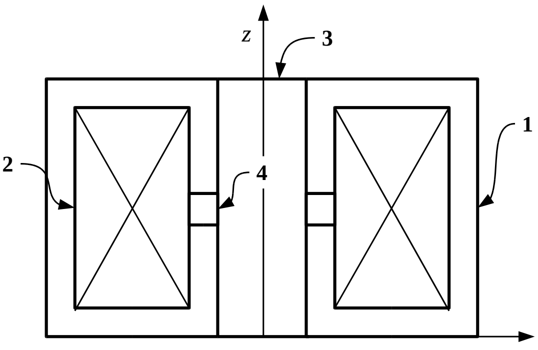

Fig. 3. Pinch mode valve schematic layout: 1 – core, 2 – coil, 3 – flow channel, 4 – non-magnetic spacer

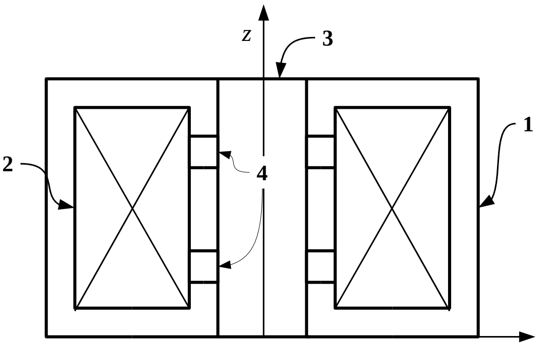

Fig. 4. Pinch mode serial valve schematic layout: 1 – core, 2 – coil, 3 – flow channel, 4 – non-magnetic spacers

In detail, the illustrated control valve height is 20 mm, and its outer diameter is 21 mm. The flow gap outer diameter is 4 mm. The non-magnetic spacer length is 2 mm. The control coil window size is 4x14 mm (width x height), and it incorporates N=150 turns of 0.51 mm dia. copper wire. The core material is low carbon steel alloy of the SAE 1010 grade, and the MR fluid's material characteristics are that of 26% Fe vol. Following Carlson et al. (2007), the core assembly may contain one coil or more control coils in series or parallel. Utilizing multiple spacers in the flow gap simply increases the activation area, and the effective output range. Such exemplary configuration is shown in Fig. 4.

The configuration revealed in Fig. 3. incorporates three 2 mm long spacers to influence the magnetic field distribution in the flow gap. Again, the length of the spacing sections is 2 mm each. The coil and the core assemblies are identical with the design of Fig. 3. Several other configurations of such MR valve were highlighted by Carlson et al. (2009) and the reader should refer to their patent application for further details.

3. MAGNETOSTATIC ANALYSIS

In this section the valve's geometry is subject to an FE analysis of the magnetic circuit of the valve. The analysis is extended to the configurations of MR valve incorporating multiple serial coils and/or multiple spacers.

First, the valve's geometry highlighted in Fig. 3 was basis for the axi-symmetric 2D (two-dimensional) model developed in FEMM ver. 4.2. The obtained results were shown in Figs. 4 through 10. Specifically, the flux density variation in the control gap area directly above the non-magnetic spacer is revealed in Fig. 5. In this figure '0' denotes the gap's centreline, and '2' refers to the inner diameter of the flow channel. The results were computed for the coil ampere turns (NI) range from 150 AT to 750 AT. For example, the figure shows that the flux density varies from appr. 0.68 T to 0.82 T for the highest excitation input of 750 AT. Moreover, the simulations show that the normal component of the flux density vector is nearly 0, and the observed contribution is due to the tangential component only. Next, by averaging the flux density distribution in the region above the spacer the flux density vs. coil ampere turns characteristics in Fig. 6 could be obtained. It is then apparent that using the above configuration of Fig. 3 the control gap's flux density can be effectively manipulated by varying the control coil's current input level. Finally, flux density maps in Fig. 7 reveal that the highest magnetic flux concentration in the flow channel is directly in the area above the spacer.

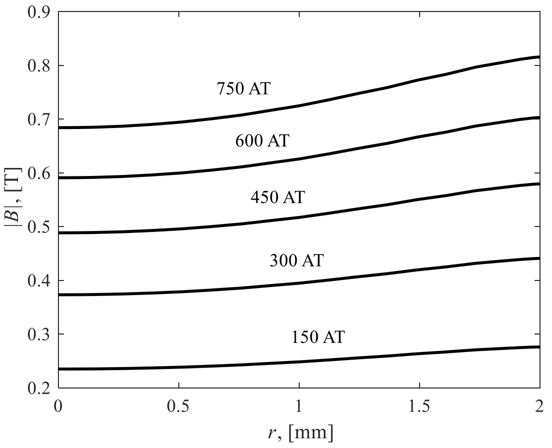

Fig. 5. Flux density variation in the flow channel

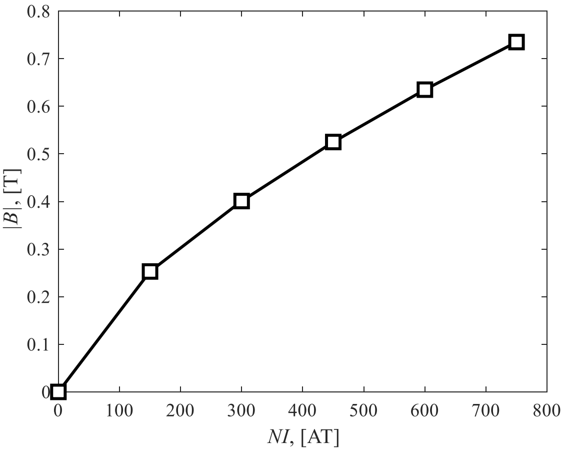

Fig. 6. Averaged flux density variation vs. coil ampere turns

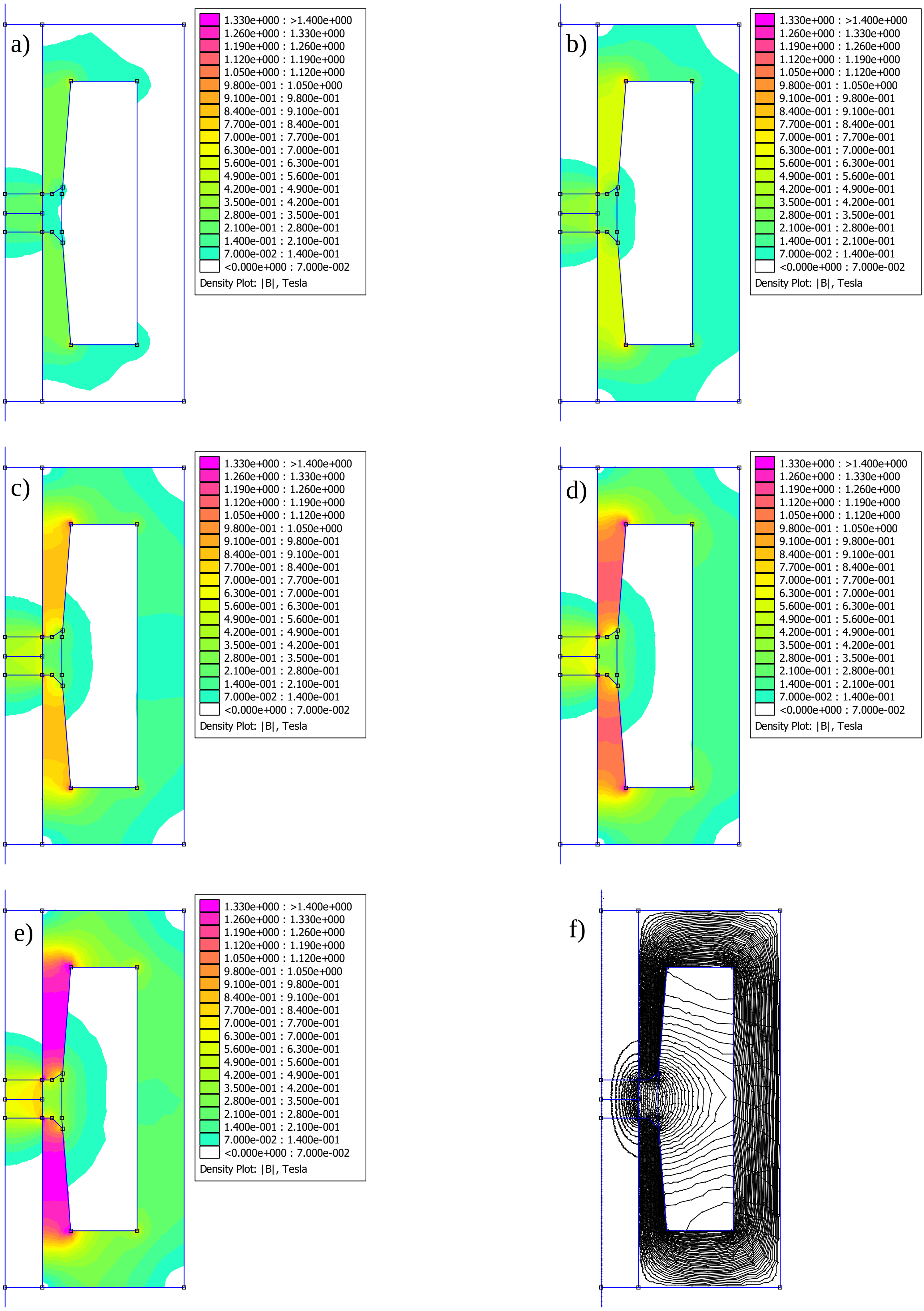

Fig. 7. Flux density contour maps and flux line distribution in single gap pinch mode, a) 150 AT, b) 300 AT, c) 450 AT, d) 600 AT, e) 750 AT, f) flux lines at 750 AT

For comparison, by analyzing the serial configuration the authors arrived at the numerical results highlighted in Fig. 8 through 10. Again, Fig. 8 illustrates flux lines distribution in the assembly, and Fig. 9 shows the averaged flux density B in the control gap vs. coil ampere turns. Specifically, the figure reveals a significantly lower effective output range for the serial configuration as the flux is required to pass through 3 air gaps. However, the activated area is 3 times larger than that of Fig. 3. Finally, Fig. 9 reveals averaged flux density vs. coil current calculated for a serial control gap configuration in which multiple coils were connected in series. The configuration that is illustrated in Fig. 10 features 3 coils of 50 wire turns each. The effective flux density output of this valve is almost identical to that of Fig. 9 for the same ampere turns level (750 AT total).

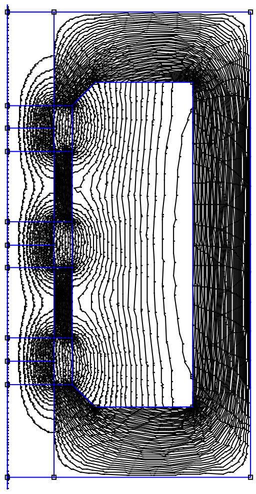

Fig. 8. Flux lines at 750 AT in multiple pinch mode gaps

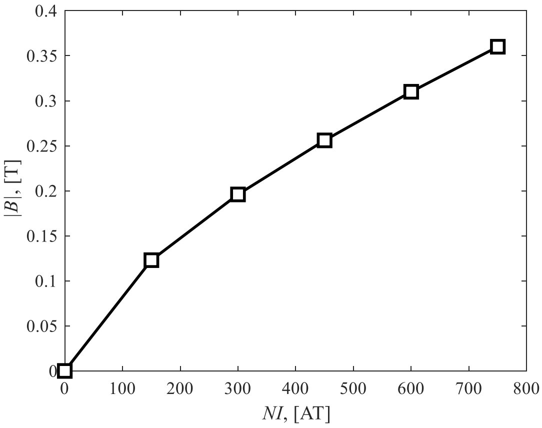

Fig. 9. Flux density vs. coil ampere turns in multiple pinch gap valve

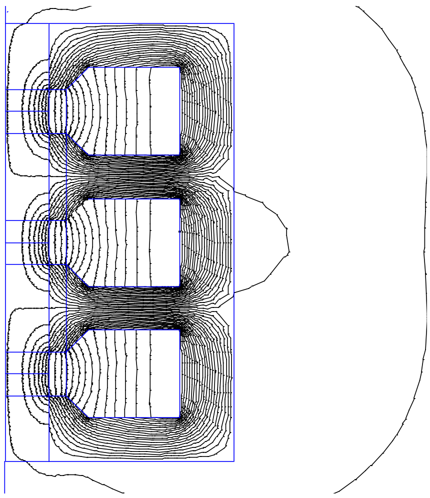

Fig. 10. Flux density map; 750 AT total in serial coil configuration

Moreover, as shown in the case of the serial coil and serial control gap configurations (see Figs. 8 and 10), respectively, the results revealed that the effective flux density is severely degraded, however, the energized surface area is significantly higher when compared against the design concept illustrated in Fig. 3.

4. SUMMARY

The so-called pinch-mode particular is the least examined of all operating modes of MR fluids. The amount of information available to researchers on this subject is limited, and hence the interest in such study. Goncalves and Carlson (2007) compared their valve to a controllable orifice in which the 'orifice' function was performed by the fluid solidified near the flow channel's walls rather than across the flow gap. Therefore, the authors commence their analysis by developing a magnetostatic model of a pinch mode valve with one control gap and one coil assembly, and then extend it to the analysis of a valve with serial flow gaps and serial coils. The results have shown that the output of this valve can be effectively controlled through modifications of the coil current level in the assembly. It is not known yet to what magnitude the computed performance of this valve will influence the smart fluid's rheology, and the resulting pressure vs. flow characteristics.

REFERENCES

1. **Boelter R., Janocha H.** (1998). Performance of long-stroke and low-stroke MR fluid dampers, *5th Annual International Symposium on Smart Structures and Materials, International Society for Optics and Photonics*, 303-313.
2. **Carlson J. D., Goncalves F., Catanzarite D., Dobbs D.** (2007), *Controllable magnetorheological fluid valve, devices, and methods*, U.S. Patent Application No. 11/844, 548.
3. **Gołdasz N., Sapiński B.** (2015), *Insight into Magnetorheological Shock Absorbers*, Springer, Heidelberg.
4. **Goncalves F. D., Carlson J. D.** (2009), An alternate operation mode for MR fluids—magnetic gradient pinch, *Journal of Physics, Conference Series*, 149, 012050.
5. **Jolly M. R., Bender J. W., Carlson J. D.** (1999), Properties and applications of commercial magnetorheological fluids, *Journal of Intelligent Material Systems and Structures*, 10(1), 5-13.
6. **Jolly M. R., Carlson J. D.** (1996), Controllable squeeze film damping using magnetorheological fluids, *Proceedings of the 5th International Conference on New Actuators*, Bremen, 333–336**.**
7. **Simms N. D., Stanway R., Johnson A. R., Mellor P.** (2001), Design, testing, and model validation of an MR squeeze-flow vibration damper, *SPIE's 8th Annual International Symposium on Smart Structures and Materials. International Society for Optics and Photonics*, 111-120.
8. **Wereley N.M., Cho J.U., Choi Y.-T., Choi S.B.** (2007), *Magnetorheological dampers in shear mode*, Smart Materials and Structures, 17(1), 015022
9. **Yao G. Z., Yap F. F., Chen G., Li W., Yeo S. H.** (2002), *MR damper and its application for semi-active control of vehicle suspension system*, Mechatronics, 12(7), 963-973.
10. **Yazid I. I. M., Mazlan S. A., Kikuchi T., Zamzuri H., Imaduddin F.** (2014), *Design of magnetorheological damper with a combination of shear and squeeze modes*, Materials and Design (1980-2015), 54, 87-95.

This work was accomplished within the scope of the programme No. E3/627/2016/DS at Cracow University of Technology.

INFLUENCE OF TERFENOL-D POWDER VOLUME FRACTION IN EPOXY MATIRX COMPOSITES ON THEIR MAGNETOMECHANICAL PROPERIES

Rafał MECH[*], **Jerzy KALETA**[*]

[*]Faculty of Mechanical Engineering, Department of Mechanics, Materials Science and Engineerings, Wrocław University of Technology,
Wybrzeze Wyspiańskiego 27, 50-370 Wrocław, Poland

rafal.mech@pwr.edu.pl, jerzy.kaleta@pwr.edu.pl

received 5 May 2015, revised 22 September 2017, accepted 25 September 2017

Abstract: In this paper the investigations of magnetostriction as well as DC magnetic properties for composites doped with Terfenol-D particles are presented. All investigations were performed for the materials with 35%, 46% and 70% volume fraction of the Terfenol-D particles surrounded by epoxy matrix. Moreover, the bulk Terfenol-D alloy was tested. The obtained results show that the magnetization of the composite materials increases with increasing the volume fraction of Terfenol-D particles. Similar dependence as for magnetization was observed for the magnetostriction measurements. Although the magnetostriction of composite material is smaller than for solid Terfenol-D it is still tens of times bigger than in case of traditional magnetostrictive materials. Obtained results gives opportunity to use these materials for variety applications such as actuators and sensors.

Key words: Magnetostriction, Magnetic Properties, Smart Materials, Active Materials

1. INTRODUCTION

Giant Magnetostrictive Materials (GMM) can convert magnetic energy into mechanical energy (they act as an actuator) or mechanical energy into magnetic energy (sensor) (Engdhal, 2000) with a very high efficiency, which allow them to be widely used in aeronautic, automotive, shipborne and civil engineering constructions as well as in medical sciences, extractive industry, acoustic equipment.

One of the materials which belongs to the Giant Magnetostrictive Materials (GMM) is Terfenol-D (Schwartz, 2002). Due to its unique properties Terfenol-D is widely used in various applications (e.g.: dampers, actuators, harvesters (Arnold, 2007, Daia et al., 2011, Li et al., 2010, Moss et al., 2012, Zhang et al., 2009)). Unfortunately, despite that Terfenol-D has many advantages, the bulk material has also an important drawbacks, such as low tensile strength and the occurrence of eddy currents as a result of work in AC magnetic field at high frequencies (Jia et al., 2009). In order to eliminate such drawbacks researchers work on composites containing the Terfenol-D particles (Kaleta et al., 2011, Dong et al., 2010, Dong et al., 2011, Lu and Li, 2010, Diquet et al., 2009). This involves necessity to examine properties of these new types of composite materials.

In this paper we present the investigation on magnetostriction and DC magnetic properties, for Terfenol-D based composites. The main goal of performed investigations was to determine the role of Terfenol-D particles addition on magnetic properties of the produced materials. Additionally the results obtained for the composites were compared with the bulk Terfenol-D.

2. MATERIAL

In this study, the magnetostrictive composites (also referred to as GMMc) were used. Samples were made by combining the epoxy resin and the GMM material (Terfenol-D) powder. At first, the epoxy resin Epolam 2015 (from Axons Technologies company) was mixed with the curing agent. Next, the appropriate amount of Terfenol-D powder with particle size of about 5-300µm (Gansu Tianxing Rare Earth Functional Materials Co., Ltd.) was added. The particles size distribution, and the shape and size of the particles are shown in Fig. 1.

a)

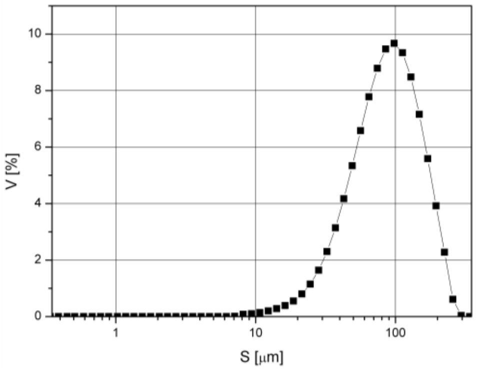

b)

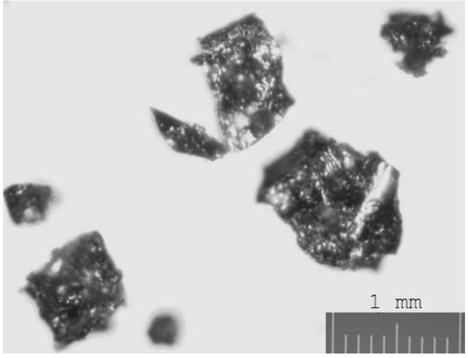

Fig. 1. Terfenol-D powder: a) grain-size analysis, b) the shape and size of the particles

The manufacturing procedure consisted in intensive mixing of all the ingredients until their complete homogenization. The mixture was then vacuum vented, poured into the dedicated cylindrical containers and subjected to initial polarization, which prevent sedimentation process. After that, the material was once again vented in the vacuum chamber to eliminate the air introduced during the mixing stage. The out-gassed samples were put in between the two strong neodymium magnets (which would lead to their final polarization) until the epoxy resin was completely cured. The scheme of a complete preparation process is shown in Fig. 2. The manufacturing procedure was described in greater detail in (Kaleta et al., 2011).

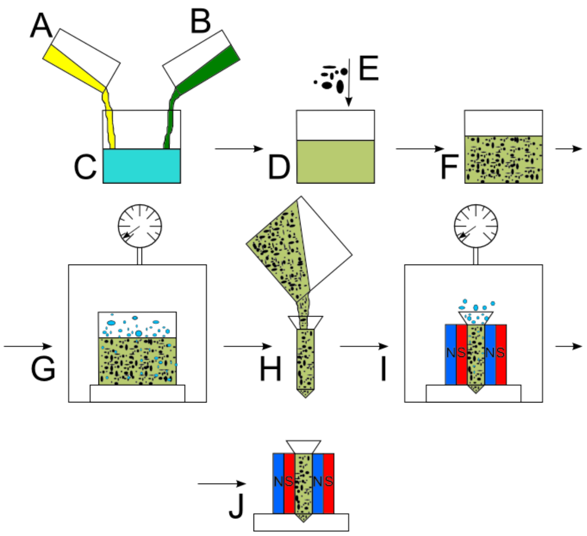

Fig. 2. Scheme of the consecutive processes in the manufacturing of the magnetostrictive composite

The specimens with three 35%, 46% and 70% volume fraction of Terfenol-D powder were obtained. In short prepared composites were described as composite 35%, composite 46% and composite 70%. The strong magnetic field (0,5T) was used to rotate the particles in such a way that their internal domain structure was parallel to the field lines. As a result of such particle alignment, the magnetic field (H) which, acting parallel to the sample axis, activates the composite, will cause the particles to rotate. In this way the resulting magnetostriction should be stronger than in the case of randomly dispersed particles.

3. MICROSTRUCTURE

The goal of investigations was to determine the properties of the produced composite materials and to determine potential differences in relation to the bulk Terfenol-D.

At first observations of a cross-sectional area of the produced composite samples were carried out. These studies were carried out on a scanning electron microscope S-3400N HITACHI. Fig. 3 presents the surface morphology of the composite samples.

More detailed analysis of images with high magnification shows that there is no discontinuity between the applied polymer matrix and Terfenol-D particles. This is mainly due to the low viscosity and relatively low shrinkage of epoxy resin, making it possible to good wetting each of the particles of a magnetostrictive material.

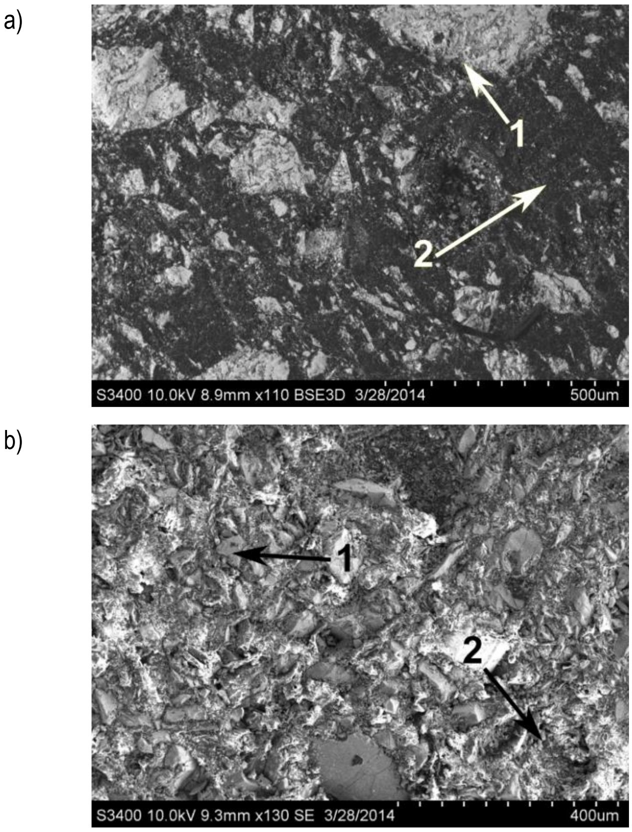

Fig. 3. Image of the composite sample surface made on scanning electron microscope, a) composite 46% with magnification 110x b) composite 70% with magnification 130x, 1 – particles of Terfenol-D powder, 2 – epoxy resin

Moreover, studies on the determination of the crystallographic phases of the samples were performed. These studies were carried out in the powder X-ray diffractometer Rigaku Ultima IV.

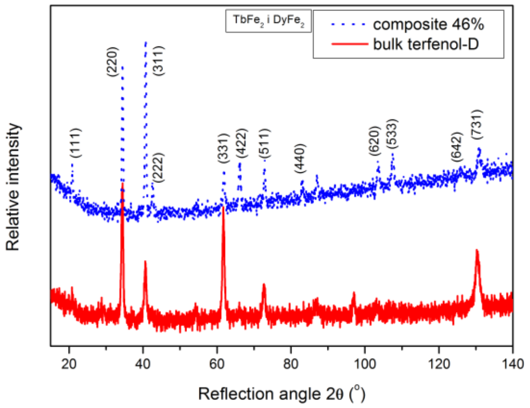

Fig. 4. X-ray diffractograms obtained for the example composite sample (46%) and bulk Terfenol-D

Obtained results shown in Fig. 4, where the X-ray diffractograms of one of prepared composite sample (composite 46%) and bulk Terfenol-D were compared. This measurements allow for the verification of the crystallographic structure of the composite material. The obtained results showed that the methodology of composite material production did not affect in any way on the crystallographic structure of the Terfenol-D particles used during the manufacture of the samples.

4. MAGNETOMECHANICAL PROPERTIES

The tests of magnetomechanical properties were carried out at room temperature, for the specific and constant value of the initial stress which was applied by the MTS testing machine. The machine kept the constant load on each specimen, during the experiment. The magnetic field strength (H) was limited by the magnetic circuit, it was 0 ÷ 175kA/m. These measurements were conducted with use of the Hall probe (placed inside the coil), for both positive and negative H values to check, if the magnetostriction of prepared composite does not depend on the sign of magnetic field. The sample displacement (Δλ) was measured using the innovative method of Fibre Bragg Grating (FBG) sensors. In this way the influence of the electromagnetic field on the results was eliminated. What is more this is a very precise method of measurements , due to the fact that resolution of the sensor is 2 ppms. The FBG method is described in more detail in (Błażejewski et al., 2011). The strain sensors were placed directly on the specimens. Additionally, during the tests the temperature inside the coil was measured and kept on constant level. All parameters were saved using automatic measurement system.

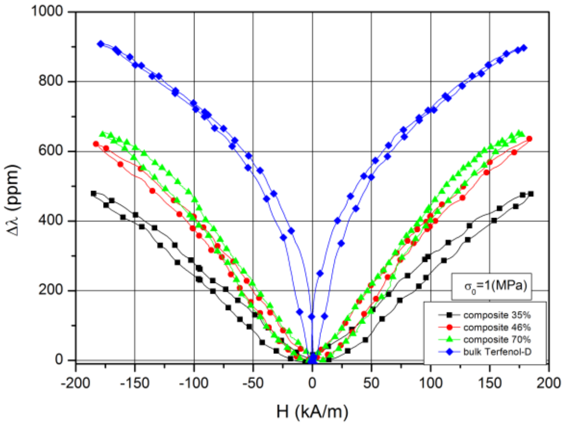

Fig. 5. Magnetostriction Δλ for the composite material and the monolithic Terfenol-D, at pre-stress σ_0=1MPa

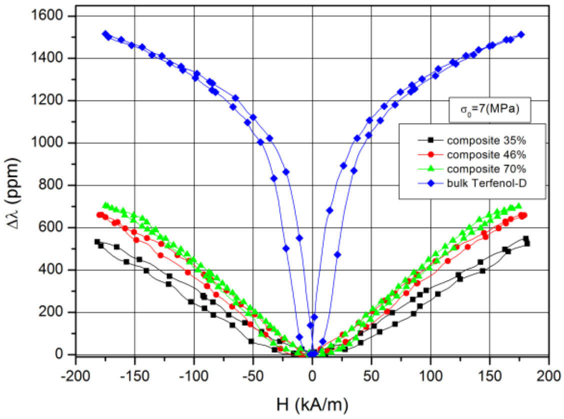

Fig. 6. Magnetostriction Δλ for the composite material and the monolithic Terfenol-D, at pre-stress σ_0=7MPa

The results obtained from the magnetostriction tests performed for the composites and bulk Terfenol-D materials, with pre-stress of σ_0=1MPa are shown in Fig. 5. The pre-stress σ_0 is specified as an initial compressive load subjected to the sample during the experiment. It is visible that the maximum value of magnetostriction measured at magnetic field of 175kA/m for the composite material consisting 35% volume fraction of Terfenol-D particles and bulk Terfenol-D alloy is equal to 495ppm and 910ppm, respectively. For the composites with higher volume fraction of Terfenol-D particles the magnetostriction values are higher than for the composite 35%, but it was still lower than for the bulk material. However, the highest value of magnetostriction was obtained for the composite with highest volume fraction of GMM particles (composite 70%).

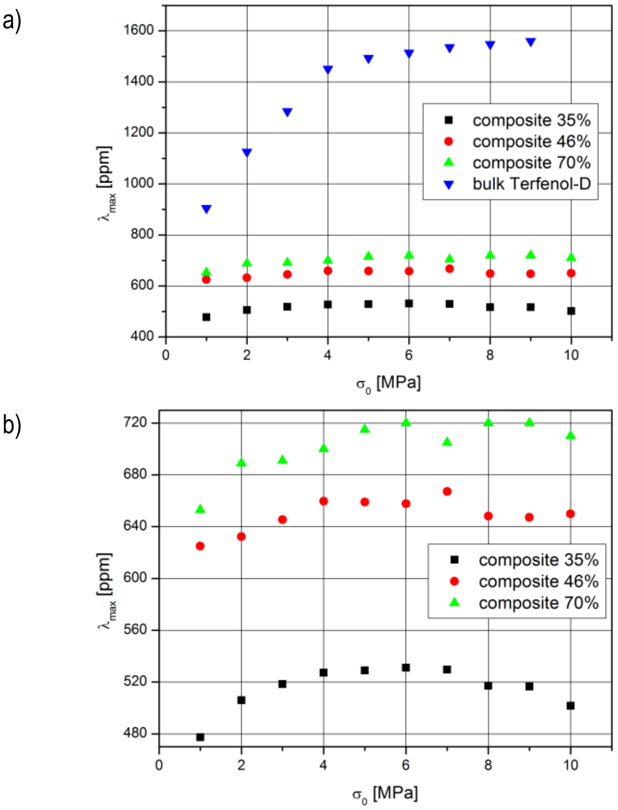

Fig. 7. Influence of the prestress σ_0 on the magnetostriction λ_{max}, for a) the composite material and bulk Terfenol-D, and b) for composites materials

In order to determine the magnetomechanical properties of the composites, the magnetostriction values $\Delta\lambda_{max}$ were compared, i.e. the values obtained for the maximum magnetic field strength H=175kA/m. A comparison of the results for the composite materials and for the bulk Terfenol-D, at 1MPa of initial stress, is shown in Fig. 5. It is clearly visible that the magnetostriction of composite materials is lower than the magnetostriction of the bulk material. The curves in Fig. 6 presents the comparison of the results obtained for the composite materials and bulk Terfenol-D for the higher value of the pre-stress (7MPa).

Comparing this graph (Fig. 6) with the previous one (Fig. 5) it can be noticed that for the higher pre-stress values the difference in magnetostriction between the composite materials and the bulk Terfenol-D is increasing.

The influence of the change in the pre-stress applied on the composites and the bulk Terfenol-D material, for the whole pre-stress range, is shown in Fig. 7. It is visible that for composite material the magnetostriction values tend to increase for the pre-stress up to 6MPa. For the higher values of pre-stress the magnetostriction decrease. There is a similar tendency in the case of the monolithic Terfenol-D, but the point in which the decrease in Δλ appears is shifted towards higher values. The magnetostriction values attained for the composite are distinctly lower compared to the monolithic material. It might be caused by the mutual interactions between the Terfenol-D powder and the composite matrix.

5. MAGNETIC PROPERTIES

Magnetic measurements were performed by using a VersaLab unit (Quantum Design) with Vibrating Sample Magnetometer option.

To determine the temperature and DC magnetic field magnetization (M) dependence for the composites and bulk Terfenol-D materials the M(T,H) characteristics were recorded. These investigations were taken in the temperature range from 50K to 400K and magnetic field range up to 3T. The exemplary hysteresis loops for the investigated alloys measured at room temperature are shown in Fig. 8.

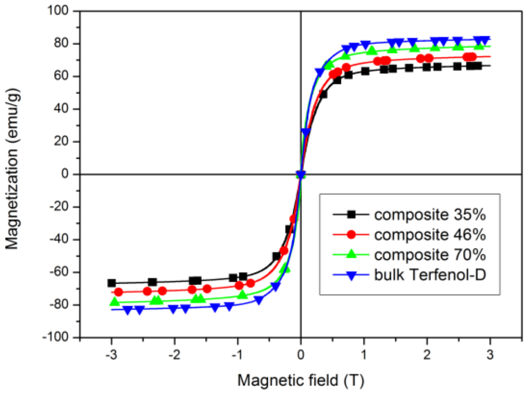

Fig. 8. Room temperature magnetization versus magnetic field for the composites and bulk Terfenol-D material

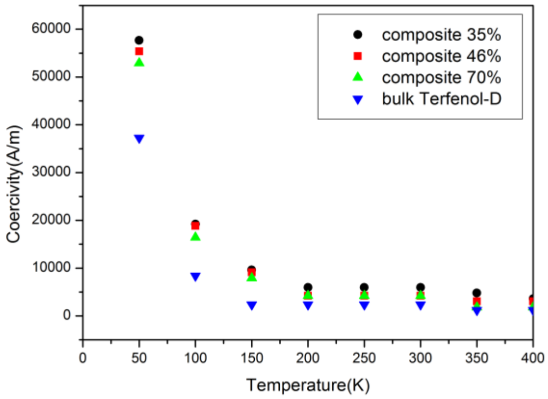

Fig. 9. Coercivity of composite material and solid Terfenol-D as the function of temperature

Changes of coercivity H_c versus temperature are presented in Fig. 9. The H_c value was taken from the magnetization measurements. It is clear that with increasing the measurements temperature decreases value of coercivity. These characteristics are very similar for all tested materials, and are related to the fact that, the magnetic interaction between particles at low temperatures are reduced, and thus the more energy must be provided to rotate the magnetic domains inside of the material. The result of such a characteristic is the appearance of coercive field for measurements of materials at low temperatures. With increasing temperature (greater than 200K) for all examined materials the coercive fields values were reduced.

6. CONCLUSIONS

The obtained results show that the magnetization of the composite materials increases with increasing the volume fraction of Terfenol-D particles. The decrease of magnetization with decreasing the volume fraction of Terfenol-D particles in composites is due to the larger distance between the magnetic particles in a polymer resin, and thus decrease in magnetic interactions between them.

Although the magnetostriction of composite material is smaller than for solid Terfenol-D it is still tens of times bigger than in case of traditional magnetostrictive materials such as: iron, nickel, cobalt for which magnetostriction values are respectively 40, 50 and 55ppms. Obtained results gives opportunity to use these materials for variety applications such as actuators and sensors. Furthermore in the near future it is possible that these materials will be used also in devices for energy harvesting applications.

REFERENCES

1. **Arnold D.P.** (2007), Review of microscale magnetic power generation, *IEEE Transactions on Magnetics*, 43, 3940-3951.
2. **Błażejewski W., Gąsior P., Kaleta J.** (2011), Application of Optical Fibre Sensors to Measuring the Mechanical Properties of Composite Materials and Structures, *Advances in Composite Materials - Ecodesign and Analysis*, InTech., 221-246.
3. **Daia X., Wena Y., Li P., Yanga J., Li M.** (2011), Energy harvesting from mechanical vibrations using multiple magnetostrictive/piezoelectric composite transducers. *Sensors and Actuators A: Physical*, 166, 94-101.
4. **Diguet G., Beaugnon E., Cavaille J.Y.** (2009), From dipolar interactions of a random distribution of ferromagnetic particles to magnetostriction, *Journal of Magnetism and Magnetic Materials*, 321, 396-401.
5. **Dong X., Qi M., Guan X., Ou J.** (2010), Microstructure analysis of magnetostrictive composites. *Polymer Testing*, 29, 369-374.
6. **Dong X., Qi M., Guan X., Ou J.** (2011), Fabrication of $Tb_{0;3}Dy_{0;7}Fe_2$/epoxy composites: Enhanced uniform magnetostrictive and mechanical properties using a dry process, *Journal of Magnetism and Magnetic Materials*, 323, 351-355.
7. **Engdhal G.** (2000), *Handbook of Giant Magnetostrictive Materials*, Academic Press.
8. **Jia A., Zhang T., Meng H., Jiang C.** (2009), Magnetostriction and eddy current loss of bonded giant magnetostrictive particle composites, *Acta Metallurgica Sinica*, 45(12),1473-1478.
9. **Kaleta J., Lewandowski D., Mech R., Zając P.** (2011), Metal, ceramic and polymeric composites for various uses., ed. by John Cuppoletti. Rijeka, InTech, cop., 475-504.
10. **Li P., Wen Y., Liu P., Li X., Jia C.** (2010), A magnetoelectric energy harvester and management circuit for wireless sensor network. *Sensors and Actuators A: Physical*, 157, 100-106.
11. **Lu X.Y., Li H.** (2010), Magnetic properties of Terfenol-D film on a compliant substrate, *Journal of Magnetism and Magnetic Materials*, 322, 2113-2116.
12. **Moss S.D., McLeod J.E., Powlesland I.G., Galea S.C.** (2012), A bi-axial magnetoelectric vibration energy harvester, *Sensors and Actuators A: Physical*, 175, 165-168.
13. **Schwartz M.** (2002), *Encyclopedia of Smart Materials*, John Wiley & Sons.
14. **Zhang C.L., Yang J.S., Chen W.Q.** (2009), Harvesting magnetic energy using extensional vibration of laminated magnetoelectric plates, *Applied Physics Letters*, 95:1, id. 013511 (3 pages).

The work has been accomplished under the grant No. 0401/0029/17

DE GRUYTER
OPEN

DOI 10.1515/ama-2017-0037

DETECTION DAMAGE IN BEARING SYSTEM OF JET ENGINE USING THE VIBROACOUSTIC METHOD

Mariusz ŻOKOWSKI[*], **Paweł MAJEWSKI**[*], **Jarosław SPYCHAŁA**[*]

[*]Division for Aeroengines, Air Force Institute of Technology, ks. Bolesława 6, 01-494 Warsaw, Poland

zokowm@itwl.pl, majewp@itwl.pl, spychj@itwl.pl

received 10 October 2016, revised 25 September 2017, accepted 26 September 2017

Abstract: The article discusses typical, operational systems for monitoring vibrations of jet engines, which constitute the propulsion of combat aircraft of the Armed Forces of the Republic of Poland. After that, the paper presents the stage of installing vibration measuring sensors in the direct area of one of the jet engine bearings, which is a support system for its rotor. The article discusses results of carried out analyses of data gathered during tests of the engine in the conditions a jet engine test bed. Results of detecting damages to the bearing, using sensors built in the direct area will be presented.

Key words: Jet Engine, Damage Of Bearings, Vibroacoustic Method, Envelope Method

1. INTRODUCTION

Using vibroacoustic processes for diagnosing mechanical devices systems from many known reasons, with the basic one being the fact that, as a residual process, which accompanies the functioning of the machines, they are a good carrier of information about their technical condition. They reflect the most significant phenomena undergoing in the machines (e.g. impacts, deformations, stresses), on which their proper functioning depends (Bloke, Mitchel, 1972). Moreover, they are characterized by ease of measurement, high speed of transmitting information and a complex time, amplitude and frequency structure, which ensures their high utility in the form of possibility to assess the condition of the whole machine, as well as its elements. Whereas, for devices of simple construction, it is quite simple to distinguish between symptoms associated with proper (correct) functioning and the growing damage symptoms. In the case of more complex devices, with a jet engine being such, the issue is no longer so unambiguous (Cempel, 1989; Randall, 2011). Complex structure and disruption, e.g. from combustion processes, required adaptation of known measures of vibroacoustic signals or even the development of new ones. Because some of the jet engines operated by the Polish Armed Forces has only simple systems for monitoring their vibrations, which control the change of rotor imbalance and some do not have it at all, an important issue is the one of having reliable algorithms, possible to apply with the aim of an expanded and reliable evaluation of their technical condition, using additional control-measurement instruments. The article discusses effects of such works, associated with the installation of additional sensors in the direct area of the tested jet engine bearing and the detection of its damage (Report of the Division for Aeroengines of Air Force Institute of Technology, 2011).

2. TYPICAL OPERATIONAL JET ENGINE VIBRATIONS MONITORING SYSTEMS

Typical diagnostic systems used in the operation of combat aircraft jet engines, use the measurement of the body vibration at one point. For example, the AŁ-21F3 engine, propulsion of the Su-22 aircraft, has one sensor of the MB-27-1Г type, fixed on the front body of the compressor (Engine 88. Technical description and operating manual,1995). It is intended to process the linear speed of vibrations acting in horizontal radial direction on the electrical signals proportional to the movement speed of the magnet in the coil. It cooperates with a block of discreet commands BDK-89, which generates information for the vibration level indicator in the cabin's pilot. Signalling of an increased vibration level is activated, in the case of reaching, in the band 50÷200 [Hz], a vibration speed equal to 88 [mm/s] in the engine rotational speed range of 54%÷80% and after reaching a vibration speed equal to 55 [mm/s] in the engine rotational speed range over 80%. Information about exceeding is also forwarded to the on-board recorded, as a single command. Moreover, information about the current vibration level is forwarded, via the engine monitoring connection, to the control panel of its parameters, during the on-ground test PNK-89 and is used to evaluate the vibration level at individual, stable ranges of the rotational speed.

A similar approach was used in the case of the RD-33 engine, which was the propulsion of the MiG-29. The vibration control system uses a sensor of the same type, the MB-27-1Г (Engine 89. Technical description,1998), installed on the body of the front supports of the high pressure compressor. It cooperates with a block of discreet commands BDK-88, which generates information for the vibration level indicator in the cabin's pilot, through illuminating a red signalling plate "Decrease rotations of the left (right)", displaying a signal "Vibrations of the left (right)" on the monitor of the "Screen", and a voice information "Vibrations of the left (right), decrease rotations of the left (right) engine". Signalling of an increased vibration level is activated, in the case of reaching a vibration speed higher than 30 [mm/s], in the band of rotational frequency changes, for a period of time longer than 3[s]. Information about the current vibration speed value and exceeding the value, as a single command, is also given to the on-board recorder. Moreover, information about the current vibration level is forwarded, via the engine monitoring connection, to the control panel of its parameters, during the on-ground test PNK-88 and is used to evaluate the vibration level at individual, stable ranges of the rotational speed.

In the case of a jet engine form the TW3-117 family, which is the propulsion of the Mi-17 and Mi-24 helicopters, also one MB-03 sensor was used, fixed to the front body of the compressor (Helicopter Mi-24D. Technical description. Avionics, 1981). It is a supplementing element of the vibration control system IW-500Je (Fig. 4). At a vibration speed level equal to 45 [mm/s], it illuminates a yellow signalling plate in the pilot's cabin, saying "Left (right) engine increased vibrations". After reaching a vibration level of 60 [mm/s], red signal plate will illuminate, which says "Turn off left (right) engine". It also generates the above binary signals for the on-board recorder. A controlled range of frequencies covers the interval 190÷340 [Hz], with the cut-off frequencies: lower - 90 [Hz], upper - 680 [Hz], and the irregularity of the amplitude characteristic ≤15%. Sensitivity threshold ≤5 [mm/s].

A more complex engine vibration monitoring system was used in the Tu-154M aircraft with engines of the type D-30KU-154. It has two vibration measurement systems (Russian IW-50 (Engine D-30KU-154. Technical description and operating manual, 1992) and an additional AVM-219 made by Vibrolot). For each of the engines, the IW-50 system has two sensors: first one, installed in the area of the front support vertical peripheral direction, the second one in the area of the rear support vertical radial direction. The AVM-219 also has two sensors: the first one, installed in the front support area horizontal radial direction, however, shifted by

180 degrees in relation to the IW-50 sensor; the second one, in the rear support area horizontal radial direction. The recorder, for each of the engines, saves data on the values of vibrations, measured with three of the four available sensors (with the exception of vibrations measured with the sensor of the IW-50 system, installed in the front support area) and one binary signal, which informs about increased engine vibrations. The pilot's cabin has two control panels installed (one for each of the two, above mentioned systems), which allow to monitor the vibrations measured by each of the four sensors and a light signalling system, which informs about exceeding the vibrations for each of the engines separately. A vibration level of 55 [mm/s] causes the yellow signalling plate "Вибрация велика" to illuminate, while a level of 65 [mm/s], the red signalling plate "Опасная вибрация". Additionally, the AVM-219 system's control panel has a switch, which allows to control the value „$2\times n_2$ – second harmonic of the rotational speed WWC", whose value is not recorded by the on-board recorder of the aircraft, but is only controlled during an on-ground test.

The discussed above, sample operational vibration measurement systems, as mentioned before, only deliver quantitative information and not qualitative, i.e., they inform about the change of an average vibration speed value in a band, covering a scope of changes of the engine's rotational frequency, rarely, its second multiplexing, without giving a reason of the changes. They are closed systems, with a limited measuring range, without the possibility of the user interfering in order to obtain additional diagnostic information. They also have a small number of sensors. That is why this study is an example of the possibility to diagnose, using sensors in new locations and applying new methodologies.

3. GENERAL CHARACTERISTICS OF THE OBJECT AND CARRIED OUT WORKS

The object of the test is the bearing (Żokowski at al., 2009), constituting a structural element of the middle support of the engine rotor, which is the main load of the bearing, as well as of the other two (Fig. 1.). The rotor is a seven-speed axial compressor and a single-speed, horizontal arm reaction turbine, couple with a splined coupling. The compressor with bearings is on the front trunnion in a ball bearing, with a separated inner ring (front bearing) and on the rear trunnion (middle bearing) in the roller bearing. The front shaft end is supported in the middle bearing of the power transmission, through a splined coupling and in the back end, in the roller bearing (rear bearing).

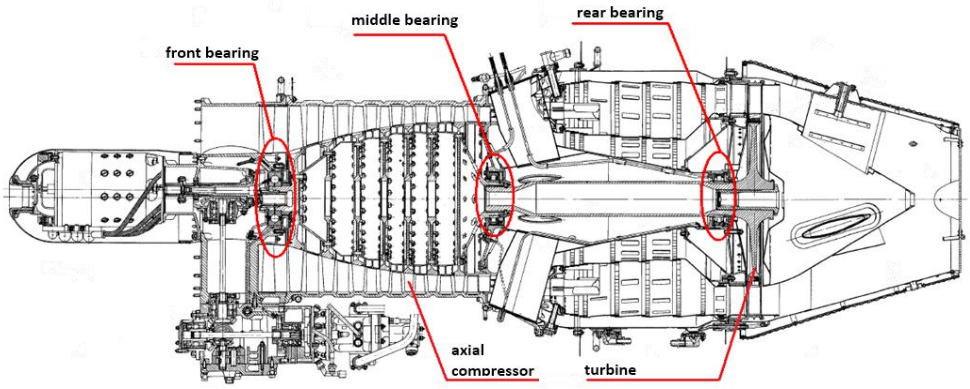

Fig. 1. Cross-section of the engine with marked bearings

As a result of structural, maintenance and operational factors, the operation would lead to damages of the middle bearing, detected by the personnel during maintenance service works. Moreover, the engine did not have a vibration measurement system.

That is why, the below studies confirm the possibility to detect damages of the bearing, through analysing the vibroacoustic signal (Dwojak, Rzepiela, 2003). That is why, inside the engine, on appropriate support, directly on the tested bearing, two single-axis piezoelectric vibration transmitters of the type 2248M1, made by Endevco (Fig. 2) were built, with one on the horizontal axis (point A marked PKY) and the second on the vertical axis (point B marked PZY).

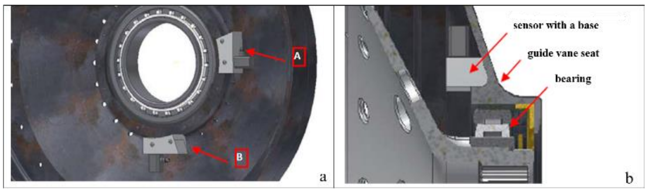

Fig. 2. Cross-section of the engine with marked bearings

Then, during the test of the engine in the engine test bed, with an operational bearing, followed by an implemented damage, the saved vibroacoustic signals were registered and analysed at a frequency of 25 [kHz]. The tested bearing was a used bearing, which came from an engine with the expired service life resource and the damage implemented (Żokowski et al., 2015), was in the form of the damage to one rolling element (Fig. 3a) and the inner race (Fig. 3b).

The envelope signal narrowband analysis method was used to analyse the signal (Report of the Division for Aeroengines of Air Force Institute of Technology, 2011; Muthukumarasamy and Ganeriwala, 2009). The results were juxtaposed in the form of a power spectrum of the determined envelopes: f_{BPFO} - defect of the outer race, f_{BPFI} - defect of the inner race, f_{BSF} - defect of the rolling element, f_{FTF} - defect of the rolling cage, for bearing parameters according to Tab. 1) and average power values of the an envelope, respectively, in the Y and Z axes, marked and P_{env_PKY} and P_{env_PKZ}.

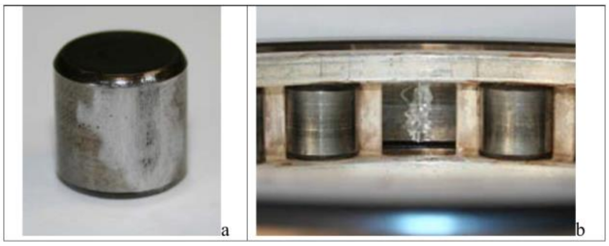

Fig. 3. Bearing damage form: a - rolling element, b - internal race

Tab. 1. View and parameters of the tested bearing

Parameter name	Value
Number of rolling elements	22
Rolling element diameter	10
Pitch diameter	105
Contact angle	0

4. TEST RESULTS

Measurements of the signals generated by an operational bearing were taken during a cold start-up of the engine (without feeding and igniting fuel). Then, at rotor frequency of 32.7 [Hz], the determined values of the bearing characteristic frequencies and their average power (Report of the Division for Aeroengines of Air Force Institute of Technology, 2011) were listed in Tab. 2 (with the center frequency of 6400 [Hz] and band of 600 [Hz]. The envelope power spectrum for axes Y and Z is presented in Fig. 4 and 5 (Report of the Division for Aeroengines of Air Force Institute of Technology, 2011).

Tab. 2. Bearing parameters at rotor speed of 32.7 [Hz]

Frequency designation	f [Hz]	P_{env_PKY} $[(m/s^2)^2]$	P_{env_PKZ} $[(m/s^2)^2]$
f_{BPFO}	325.65	0.0242	0.0377
f_{BPFI}	394.21	0.0186	0.0352
f_{FTF}	14.8	0.0343	0.0486
f_{BSF}	170.23	0.0162	0.029
$0.5{*}f_{BSF}$	8511	0.0242	0.03

Measurements of the signals generated by a damaged bearing were taken during a cold start-up of the engine (without feeding and igniting fuel) and during a hot test. For the cold start-up, at rotor frequency of 33.1 [Hz], the determined values of the bearing characteristic frequencies and their average power (Report of the Division for Aeroengines of Air Force Institute of Technology, 2011) were listed in Tab. 3 (with the center frequency of 6400 [Hz] and band of 600 [Hz]. The envelope power spectrum for axes Y and Z is presented in Fig. 6 and 7 (Report of the Division for Aeroengines of Air Force Institute of Technology, 2011). For the hot test, at rotor frequency of 120.1 [Hz], the determined values of the bearing characteristic frequencies and their average power (Report of the Division for Aeroengines of Air Force Institute of Technology, 2011) were listed in Tab. 4 (with the center frequency of 6400 [Hz] and band of 1550 [Hz]. The envelope power spectrum for axes Y and Z is presented in Fig. 7 and Fig. 8 (Report of the Division for Aeroengines of Air Force Institute of Technology, 2011).

Tab. 3. Bearing parameters at rotor speed of 32.7 [Hz]

Frequency designation	f [Hz]	P_{env_PKY} $[(m/s^2)^2]$	P_{env_PKZ} $[(m/s^2)^2]$
f_{BPFO}	329.91	0.0673	0.0751
f_{BPFI}	399.36	0.0306	0.0357
f_{FTF}	15.0	0.143	0.201
f_{BSF}	17245	0.0335	0.051
$0.5{*}f_{BSF}$	8623	0.0421	0.188

Tab. 4. Bearing parameters at rotor speed of 120.1 [Hz]

Frequency designation	f [Hz]	P_{env_PKY} $[(m/s^2)^2]$	P_{env_PKZ} $[(m/s^2)^2]$
f_{BPFO}	1194.64	3.3	1.4
f_{BPFI}	1447.35	0.5	1.2
f_{FTF}	54.35	2.5	4.5
f_{BSF}	624.9	1.5	3.9
$0.5{*}f_{BSF}$	312.5	2.7	4.8

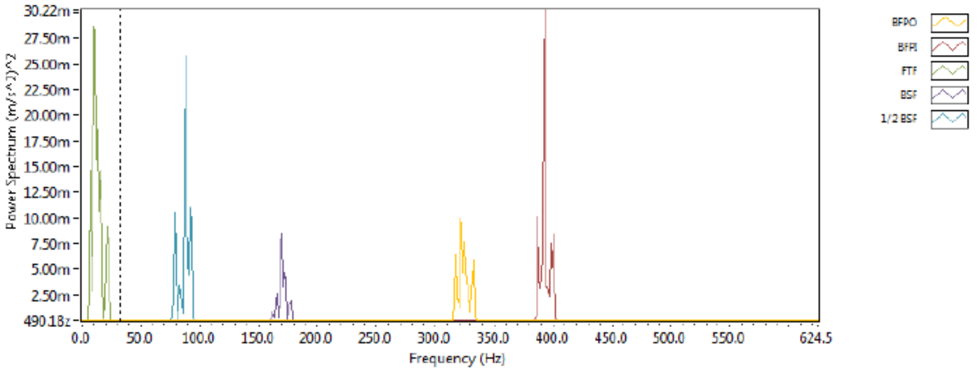

Fig. 4. Power spectrum determined with the envelope narrowband analysis method - point A

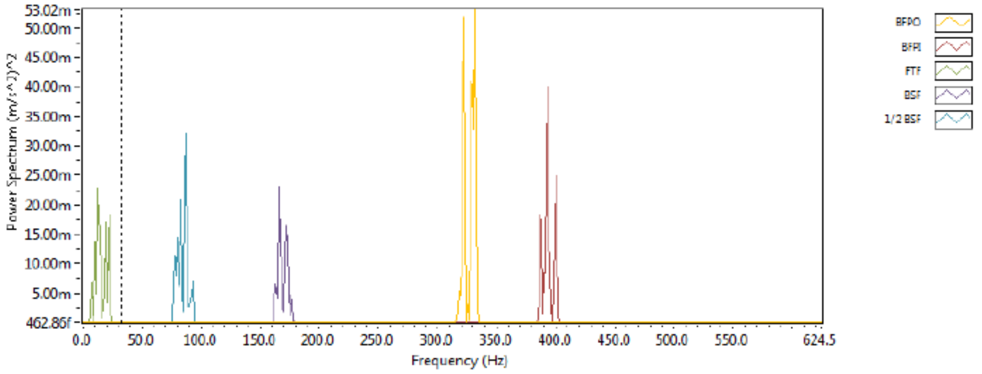

Fig. 5. Power spectrum determined with the envelope narrowband analysis method - point B

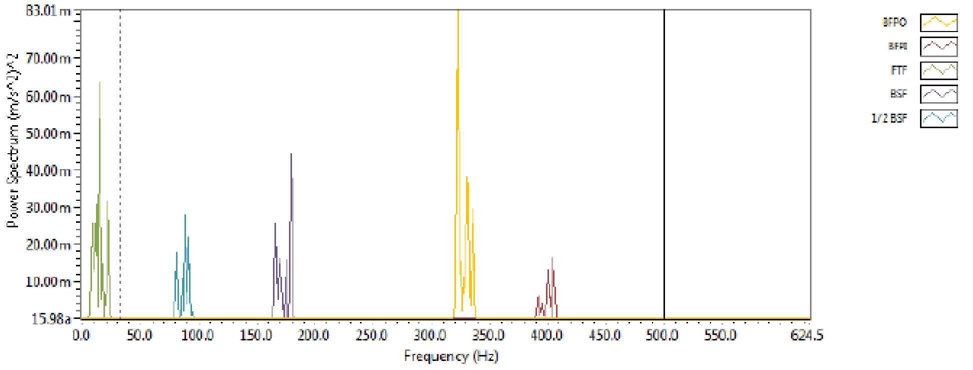

Fig. 6. Power spectrum determined with the envelope narrowband analysis method - point A

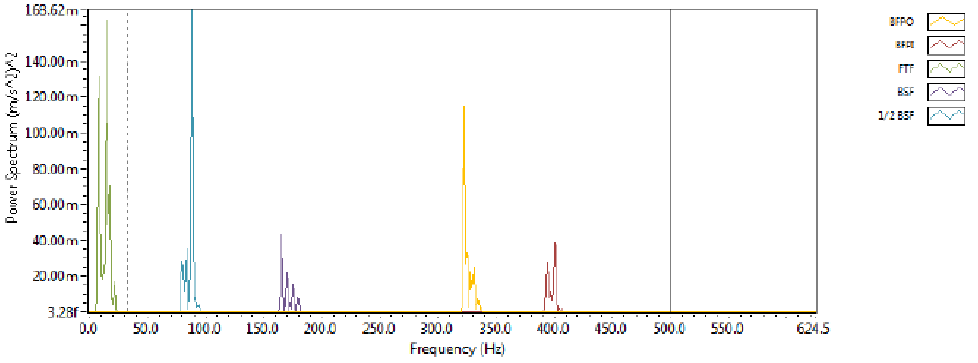

Fig. 7. Power spectrum determined with the envelope narrowband analysis method - point B

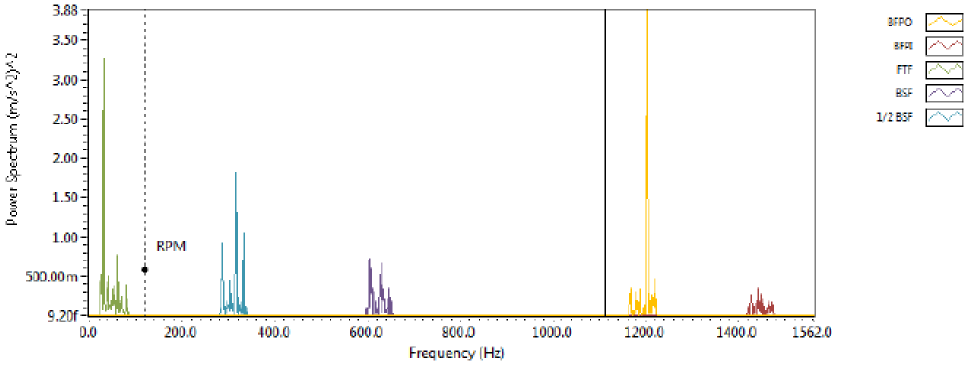

Fig. 8. Power spectrum determined with the envelope narrowband analysis method - point A

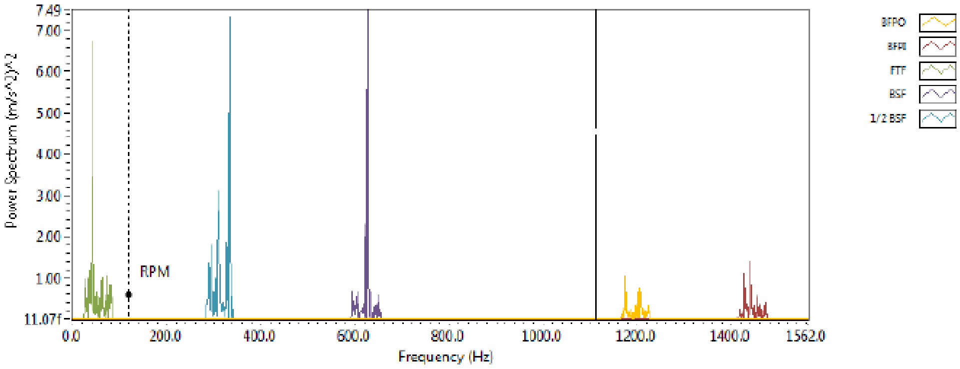

Fig. 9. Power spectrum determined with the envelope narrowband analysis method - point B

5. CONCLUSIONS

The tested bearing was a used bearing, which came from an engine with the expired service life resource, thus already having operational wears/damages of the particular elements of its structure. That is probably why, in the bearing envelope spectrum, already in its initial state, observed are all computation frequencies of the studied bearing. However, when comparing the levels of the determined average powers of the signal of the bearing, treated as operational (Fig. 10, 11 - red colour) in relation to the damaged one (Fig. 10, 11 - blue colour), there is a visible increase of the frequencies f_{BPFO}, f_{BSF} and $0{,}5 \cdot f_{BSF}$ as directly associated with the damage of the internal race and the rolling element. There was also a significant increase of the power of frequency f_{FTF}, which is theoretically associated with the defect of the rolling cage.

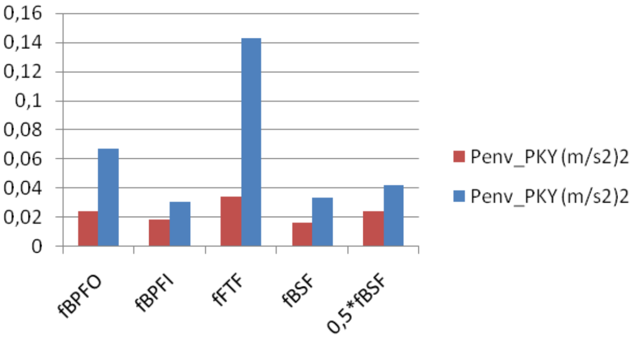

Fig. 10. Average characteristics frequency powers of bearing at point A

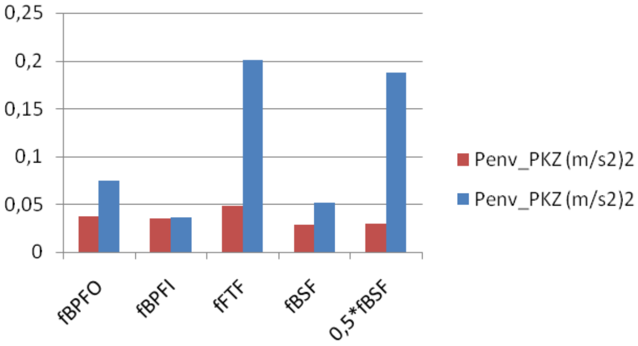

Fig. 11. Average characteristics frequency powers of bearing at point B

Generally, it was confirmed, that with jet engines, it was possible to analyse the bearing technical condition with the envelope vibroacoustic signal narrowband analysis. Whereas, when comparing the signal powers determined at cold start-up (rotor is rotated by a generator-starter and no fuel combustion processes occur – Tab. 3) and during a test of the engine (correct engine operation, at a small gas range, with present combustion processes – Tab. 4), there is visible even a one-hundred-fold difference in value. That in mind, during the trend analysis, we need to pay attention to the engine's operation range.

REFERENCES

1. **Bloke M., Mitchel W.**, (1972), *Vibration and acoustic measurement handbook*, New York, Spartan Books, Chapter 22.
2. **Cempel C.** (1989*), Vibroacoustics used*, PWN, Warsaw, (in Polish).

3. **Dwojak J., Rzepiela M.**, (2003), *Diagnostics and maintenance of rolling bearings*, Guidance, Technical Diagnostics, Warsaw, (in Polish).
4. **Muthukumarasamy A., Ganeriwala S.**, (2009), *Diagnosis of Rolling Element Bearing Faults using Envelope analysis*, SpectraQuest Tech Note.
5. **Randall R.**, (2011), *Vibration-based Condition Monitoring. Industrial, Aerospace and automotive applications*, Willey and Sons, Ltd, Publication.
6. **Żokowski M.**, **Spychała J.**, **Majewski P.** (2015), The Use of the Vibroacoustic Method for Monitoring the Technical Condition of Aero Engines with Extended Time between Overhauls, *Solid State Phenomena*, 220, 283-288.
7. **Żokowski M.**, **Spychała J.**, **Szczekala M.**, (2009), Diagnosis of the jet-propelled engine by vibration analysis, *Transport Problems*, 4(3), Part 2, 75-81.
8. Engine 88. Technical description and operating manual (1995) (in Polish).
9. Engine 89. Technical description (1988) (in Polish).
10. Engine D-30KU-154. Technical description and operating manual, (1992) (in Polish).
11. Helicopter Mi-24D. Technical description. Avionics. Poznan (1981) (in Polish).
12. Report of the Division for Aeroengines of Air Force Institute of Technology (2011), execution of the development project no. OR00010209, concluded between the Minister of Education and Higher Education and the Director of the Air Force Institute of Technology (in Polish).

DE GRUYTER
OPEN

DOI 10.1515/ama-2017-0038 *acta mechanica et automatica, vol.11 no.3 (2017)*

DETERMINATION OF A VIBRATING BOWL FEEDER DYNAMIC MODEL AND MECHANICAL PARAMETERS

Martin STURM[*], **Lubomir PESIK**[**]

[*]Faculty of Mechanical Engineering, University of Applied Sciences Zittau/Görlitz, Theodor-Körner-Alleé 16, Zittau, Germany
[**]Faculty of Mechanical Engineering, Technical University of Liberec, Studentská 2, 46117 Liberec, Czech Republic

m.sturm@hszg.de, lubomir.pesik@tul.cz

received 13 October 2016, revised 26 September 2017, accepted 27 September 2017

Abstract: Vibrating conveyors also named bowl feeders are a common equipment for conveying goods into production systems. These systems are used for the supplying of a certain number of goods to an individual designed interface and simultaneously arranging a correct orientation of the goods conveyed by the same time. This type of conveyor is used in various industries, such as for example automotive industry, electronic industry and medical industry. The target of this article is to determine a dynamic model and mechanical parameters by means of testing, and a numerical simulation of a ready-to-operate conveyor under standard working conditions.

Key words: Vibrating Conveyor, Bowl Feeder, Resonance Frequencies, Dynamic Model, Mechanical Parameters

1. INTRODUCTION

The bowl feeder that was used for determination of the dynamic model and mechanical parameters for future testing and numerical simulations was originally built to forward parts for the electronic industry and is shown in Fig. 1.

Fig. 1 Bowl feeder for testing

The technical specification of the bowl feeder was as follows in Tab. 1 and in Fig. 2:

Tab. 1. Parameters of the bowl feeder

A	**B**	**C**	**D**
700 mm	450 mm	400 mm	300 mm
F	**G**	**H**	**K**
535 mm	485 mm	190 mm	48 mm
L	**Total mass**	**Capacity**	**Moving mass**
130 mm	123 kg	12 kg	33 kg

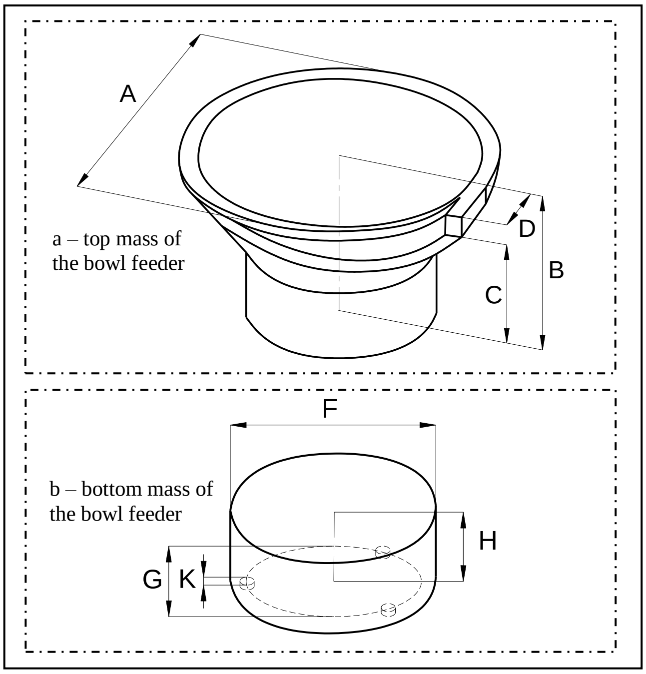

Fig. 2. Parameters of the bowl feeder (http://www.sortimat.com/de/mediadb/Zufuhr/Downloads/sortimat_ZFTdt_techdata_WF.pdf)

The spring material of the bowl feeder is "Durostone", similar to the present available quality UPM S16 fibre-reinforced plastic. Each of the three springs (flat spring packages) is installed under 15° to a vertical boundary line. The excitation device is composed by three electromagnetic vibration exciters. Each of them is placed close to the spring (Fig. 3).

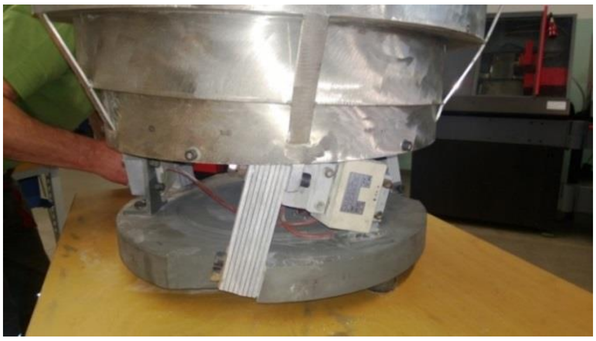

Fig. 3. Springs package with excitation device

2. DETERMINATION OF THE BOWL FEEDER DYNAMIC MODEL

The assembly of the bowl feeder includes two principal parts, a conveying element with a conical form and a supporting cylindrical element (Griemert and Römisch, 2015; Sebulke 2017). The first was indexed by character N and the other by character S. Both parts are connected by springs and they are uniformly distributed around their rotational axes y_N and y_S. In our case, there were used three flat springs packages. Each package was declined by angle β_{NS} to the axis plane, it had its stiffness and the total values of all springs packages were defined as k_{NS}. The total damping coefficient was described by value b_{NS} (Lanets etal., 2016).

The conveying element was defined by its mass $\mathrm{m_N}$ and by its moment of inertia J_{Ny} around rotational axis y. The supporting element had mass m_S, the moment of inertia J_{Sy}, and it was placed on rubber springs with total stiffness k_{SRx} and k_{SRy}, and with total damping coefficients b_{SRx} and b_{SRy}. The whole system was fixed with a rigid connection to the frame (Nendel, 2008; Risch, 2008; Decker, 2014).

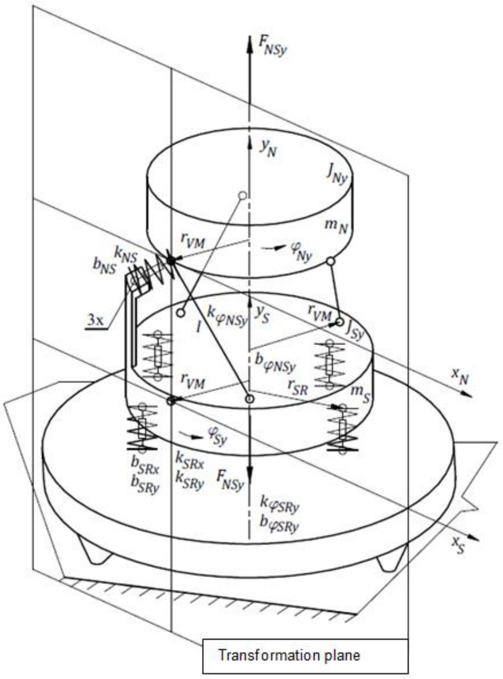

Fig. 5. Mechanical model of the bowl feeder with transformation plane (own source)

In the dynamic model of the system, each flat springs package is replaced by a rod and a spring with a perpendicular effect. All three rods create a joint mechanism between two parts of the bowl feeder (Harris, 2005; Buja, 2007; Mata 2016).

The movement of the bowl feeder system can be described with help of four coordinates, two translations y_N, y_S and two rotations φ_{Ny}, φ_{Sy}. The relative movements of both parts are defined:

$$y_{NS} = y_N - y_S \tag{1}$$

and

$$\varphi_{NSy} = \varphi_{Ny} - \varphi_{Sy} \, . \tag{2}$$

In these intentions four differential equations describing the movement of the bowl feeder system can be written:

$$m_N \ddot{y}_N + F_{bNSy} + F_{kNSy} + F_{VM} \cos\beta_{NS} = F_{NSy} \, , \tag{3}$$

$$J_{Ny} \ddot{\varphi}_{Ny} + M_{bNSy} + M_{kNSy} - r_{VM} F_{VM} \sin\beta_{NS} = 0 \, , \tag{4}$$

$$\begin{aligned} &m_S \ddot{y}_S + b_{SRy} \dot{y}_S - F_{bNSy} + k_{SRy} y_S - F_{kNSy} - \\ &-F_{VM} \cos\beta_{NS} = -F_{NSy} \end{aligned} \tag{5}$$

and

$$\begin{aligned} &J_{Sy} \ddot{\varphi}_{Sy} + b_{\varphi SRy} \dot{\varphi}_{Sy} - M_{bNSy} + k_{\varphi SRy} \varphi_{Sy} - M_{kNSy} + \\ &+ r_{VM} F_{VM} \sin\beta_{NS} = 0 \, , \end{aligned} \tag{6}$$

where force F_{VM} is a connection force between the conveying part and the supporting part which is transferred by the joint mechanism of both parts. Force F_{NSy} is the exciting force between the conveying part and supporting part.

For an example, the following parameters for the characters have been chosen:

$m_N = 90 \, Kg$	$F_{NS} = 2310 N$
$m_S = 33 Kg$	$J_N = 3{,}9 \, Kgm^2$
$\beta = 15°$	$J_S = 1{,}1 \, Kgm^2$
$k_{NS} = 5698007 \, \frac{N}{m}$	$b_{NS} = 880 \, \frac{Kg}{s}$

The other dynamic forces are calculated as follows:

$$F_{bNSy} = b_{NS} \dot{y}_{NS} \, , \tag{7}$$

$$F_{kNSy} = k_{NS} y_{NS} \, , \tag{8}$$

$$M_{bNSy} = F_{bNSx} r_{VM} = b_{NS} r_{VM}^2 \dot{\varphi}_{NSy} \, , \tag{9}$$

and

$$M_{kNSy} = F_{kNSx} r_{VM} = k_{NS} r_{VM}^2 \varphi_{NSy} \, , \tag{10}$$

where:

$$F_{bNSx} = b_{NS} \dot{x}_{NS} \, , \tag{11}$$

and

$$F_{kNSx} = k_{NS} x_{NS} \, . \tag{12}$$

Torsional damping coefficient $b_{\varphi SRy}$ and torsional stiffness $k_{\varphi SRy}$ are:

$$b_{\varphi SRy} = b_{SRx} r_{SR}^2 \tag{13}$$

and

$$k_{\varphi SRy} = k_{SRx} r_{SR}^2 \, . \tag{14}$$

The relation between relative coordinates y_{NS} and φ_{NSy} is done by joint mechanism:

$$y_{NS} = \varphi_{NSy} r_{VM} \tan \beta_{NS} \ \ . \tag{15}$$

In order to make a simplification of the calculation of equations (3) to (6), it is possible to write the balance of forces in the transformation plane (Fig. 6) as follows (Pešík, 2012):

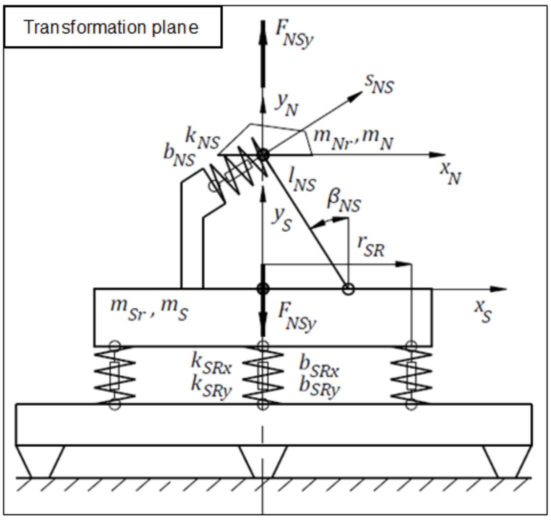

Fig. 6. Dynamic model in the transformation plane (own source)

$$x_{Nr} = r_{VM} \varphi_{Ny} \, , \tag{16}$$

$$x_{Sr} = r_{VM} \varphi_{Sy}, \tag{17}$$

$$x_{NSr} = r_{VM} \varphi_{NSy}, \tag{18}$$

$$y_{Nr} = y_N, \tag{19}$$

$$y_{Sr} = y_S \, , \tag{20}$$

$$y_{NSr} = y_{NS} \tag{21}$$

$$J_{Ny} = m_{Nr} r_{VM}^2 \, . \tag{22}$$

$$J_{Sy} = m_{Sr} r_{VM}^2 \, . \tag{23}$$

By introduction of coordinate s_{NSr} the number of unknown functions decreases to three:

$$x_{NSr} = s_{NSr} \cos \beta_{NS} \tag{24}$$

and

$$y_{NSr} = s_{NSr} \sin \beta_{NS}. \tag{25}$$

After the adjustment of the equations (3) to (6), it is possible to write in the matrix form (Decker, 2014):

$$\bar{M}\ddot{\bar{q}} + \bar{B}\dot{\bar{q}} + \bar{K}\bar{q} = \bar{Q} \, . \tag{26}$$

where are mass matrix:

$$\bar{M} = \begin{vmatrix} m_N \sin^2\beta_{NS} + m_{Nr}\cos^2\beta_{NS} & m_{Nr}\cos\beta_{NS} & m_N \sin\beta_{NS} \\ m_{Nr}\cos\beta_{NS} & m_{Sr} + m_{Nr} & 0 \\ m_N \sin\beta_{NS} & 0 & m_S + m_N \end{vmatrix}, \tag{27}$$

damping matrix:

$$\bar{B} = \begin{vmatrix} b_{NS} & 0 & 0 \\ 0 & b_{SRr}\frac{r_{SR}^2}{r_{VM}^2} & 0 \\ 0 & 0 & b_{SRy} \end{vmatrix}, \tag{28}$$

stiffness matrix:

$$\bar{K} = \begin{vmatrix} k_{NS} & 0 & 0 \\ 0 & k_{SRr}\frac{r_{SR}^2}{r_{VM}^2} & 0 \\ 0 & 0 & k_{SRy} \end{vmatrix}, \tag{29}$$

coordinates vector:

$$\bar{q} = \begin{vmatrix} s_{NSr} \\ x_{SR} \\ y_{SR} \end{vmatrix} \tag{30}$$

and exciting vector:

$$\bar{Q} = \begin{vmatrix} F_{NSy} sin\beta_{NS} \\ 0 \\ 0 \end{vmatrix}. \tag{31}$$

From the matrix equation (26) it is to calculate time vector function $\bar{\mathrm{q}}$. The parameters of the bowl feeder system are either known or can be measured. The mass parameters of the conveying and supporting parts are defined in the production documentation. The stiffness and damping parameters are a bit difficult to measure and some differences can be expected between the parameters measured in a static or a dynamic way.

3. EXPERIMENTAL DETERMINATION OF DYNAMIC PARAMETERS

Many dynamic parameters can be taken from the technical documentation of the bowl feeder (Tab. 1), the others are calculated or very often measured during the correct excited oscillation.

The primary task of the bowl feeder is the generation of micro throws, and by doing this, the conveyance of goods. Therefore the excitation of bowl feeder free oscillating was realized by a rubber coated hammer in the tangential direction and the oscillation was observed in the vertical direction. For this test, the sensor was mounted vertically under the spiral path of the bowl.

The base for the experimental determination of the dynamic parameters is the measurement of free oscillation kinematic values. The results of this step are time and frequency functions of acceleration (Fig. 7 and Fig. 8).

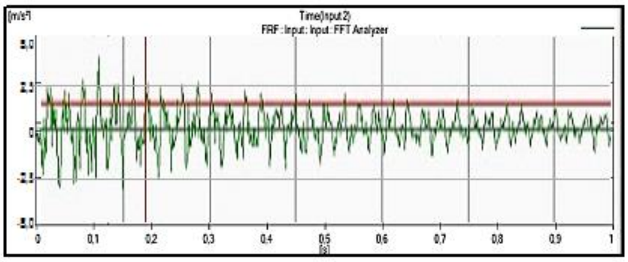

Fig. 7. Time function of acceleration in vertical direction by free oscillation (Machine laboratory, HSZG)

DOI 10.1515/ama-2017-0038

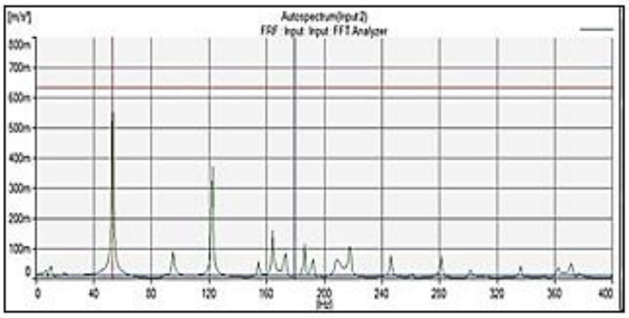

Fig. 8. Frequency function of acceleration in vertical direction by free oscillation (Machine laboratory, HSZG)

As mayor natural frequency, 50 Hz is identified in Fig. 8. The excitation frequency of the operating bowl feeder is 50 Hz as well. That shows, the bowl feeder is operation on resonance.

The data supplying necessary information on amplitudes decrease and frequencies. From the time function of acceleration it is possible to find the damping parameters of the bowl feeder system, and the frequency function gives information about its natural frequencies.

In the followed case of the bowl feeder, there is to determine relative weak damping and three principal natural frequencies which correspond to three coordinates of vector function $\bar{q}$.

The identification of the dynamic parameters is simpler by a reduction of the system, for example - the system with only one degree of freedom. There is considered the stiffness of the rubber springs of the infinitive value. In reality, the supporting part is fixed to the frame and then the equation (26) in case of the free oscillation is reduced to form:

$$\left(m_N \sin^2 \beta_{NS} + \frac{J_{Ny}}{r_{VM}^2} \cdot \cos^2 \beta_{NS}\right) \ddot{s}_{NS} + b_{NS} \dot{s}_{NS} + \\ + k_{NS} s_{NS} = 0 \,. \qquad (32)$$

From the equation (32), values of damping coefficient b_{NS} and stiffness k_{NS} are determined with help of comparing measured and calculated time function $\ddot{s}_{NS}$ (Lanets et al., 2016).

The simplified system is excited and brought in free oscillating. Measured acceleration $\ddot{s}_{NS}$ of coordinate s_{NS} is shown in Fig. 9 as the time function.

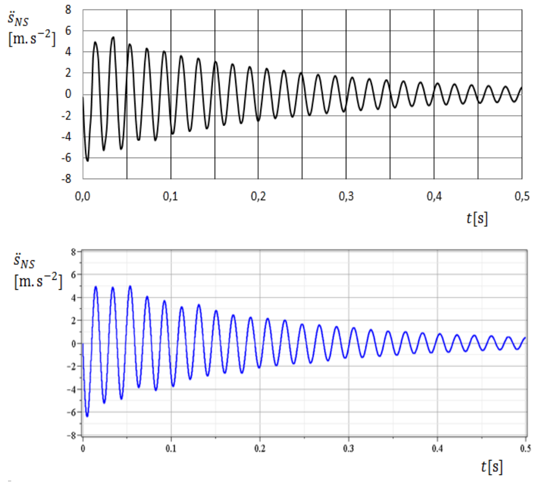

Fig. 9. Time function of acceleration measured (black function) and calculated (blue function) on the simplified system (authors result)

The values of parameters b_{NS} and k_{NS} are chosen so that the measured and calculated time function may show the same or similar curve.

After obtaining of the parameters b_{NS} and k_{NS}, the system of the bowl feeder can be returned in the more general configuration as is illustrated in the Fig. 6 and the method is repeated for the parameters b_{SRx}, b_{SRy}, k_{SRx} and k_{SRy}.

4. SUMMARY

The paper deals with the determination of dynamic parameters of a bowl feeder conducted with a comparison method of simulation and testing results.

The behaviour of the bowl feeder dynamic system is simulated by free oscillation. The results of this simulation are kinematic functions of the bowl feeder oscillation, above all the acceleration time function with data about natural frequencies and the damping of the system. It is advantageous to simplify the dynamic system and thus the kinematic functions, as well, to determine its parameters and advance step by step as far as the full system of the bowl feeder. The same time functions are measured by testing of the bowl feeder in the corresponding configuration of the system. By identical behaviour of simulated and measured functions the dynamic parameters are defined in equations of motion.

REFERENCES

1. **Buja H.O.** (2007), *Practice Handbook Ram- and Vibrationtechnique* (in German*)*, Bauwerk Verlag Berlin.
2. **Decker K.H.** (2014), *Machine elements – Function, Design and calculaion (in German),* Carl Hanser Verlag GmbH & Co. KG.
3. **Dresig, H., Holzweißig F.** (2008), *Machine Dynamics 8 (in German)*, Auflage, Springer Verlag, Berlin
4. **Griemert, R., Römisch, P.** (2015): *Conveying Technology (in German),* Springer Fachmedien Wiesbaden.
5. **Harris C.M.** (2005), *Shock and Vibration Handbook*, 5th edition, McGraw-Hill, New York.
6. **Lanets O.S., Kachmar R. Ya., Borovets V.M.** (2016), Jusitification of parameters of the vibratory hopper feeder with an electromagnetic drive, *Industrial Process Automation in Engineering Instrumentation*, 50, 54-76.
7. **Mata A.S.** (2016*): Fundamentals of Machine Theory and Mechanisms-Kinematic Analysis of Mechanisms,* Springer International Publishing.
8. **Nendel K.** (2008), *Two-Dimensional Motion Form of Virbartory Converyors* (in German), http://www.vibrationsfoerdertechnik.de/Download/2D Bewegungsformen_WGTL_Tagungsband08.pdf.
9. **Pešík M.** (2012), Kinematics of Objects in Vibratory Conveors, *ACC Journal, 1st edition*, Liberec: Technical University of Liberec, http://acc-ern.tul.cz/cs/journal/item/root/acc-journal-xviii-12012.
10. **Risch T.** (2008*), 2D-Vibration Forms of Vibratory Conveors* (in German), http://www.vibrationsfoerder-technik.de/Download/2D-Bewegungsformen_WGTL_Poster08.pdf.
11. **Sebulke, J.** (2017): *Handbook of Mechanical Engineering (in German)*, Springer Vieweg, Wiesbaden.
12. **Sortimat Technology GmbH & Co.**, *Conveyor Technique* (in German), http://www.sortimat.com/de/mediadb/Zufuhr/Downloads /sortimat_ZFTdt_techdata_WF.pdf (05.02.2017).

ABSTRACTS

Bogdan Korobko, Ievgen Vasyliev
The Test Method for Rheological Behavior of Mortar for Building Work

This paper offers a test method for rheological behavior of mortars with different mobility and different composition, which are used for execution of construction work. This method is based on investigation of the interaction between the valve ball and the mortar under study and allows quick defining of experimental variables for any composition of building mortars. Certain rheological behavior will permit to calculate the design parameters of machines for specific conditions of work performance – mixing (pre-operation), pressure generation, pumping to the work site, workpiece surfacing.

Cezary Kownacki Leszek Ambroziak
Flexible Structure Control Scheme of a UAVs Formation to Improve The Formation Stability During Maneuvers

One of the issues related to formation flights, which requires to be still discussed, is the stability of formation flight in turns, where the aerodynamic conditions can be substantially different for outer vehicles due to varying bank angles. Therefore, this paper pro-poses a decentralized control algorithm based on a leader as the reference point for followers, i.e. other UAVs and two flocking behaviors responsible for local position control, i.e. cohesion and repulsion. But opposite to other research in this area, the structure of the formation becomes flexible (structure is being reshaped and bent according to actual turn radius of the leader. During turns the structure is bent basing on concentred circles with different radiuses corresponding to relative locations of vehicles in the structure. Simultaneously, UAVs' airspeeds must be modified according to the length of turn radius to achieve the stability of the structure. The effectiveness of the algorithm is verified by the results of simulated flights of five UAVs.

Bogdan Sapiński
Laboratory Testing of Velocity Sensing in an MR Damper With Power Generation

The study summarises the results of experimental examination of velocity sensing capability in a prototype of a magnetorheological damper with power generation (MRD). The device has two main components: an electromagnetic power generator and an MR damper. The study outlines the structure of the device with the main focus on the generator part, and provides results of tests performed under the idle run. The discussion of demonstrates the potentials of MRD action as a velocity-sign sensor and presents key issues which need to be addressed to enable its real life applications.

Jerzy Narojczyk, Dmitrij Morozow
Modification of TiN coatings by Ion Implantation

The high-speed steel HS 6-5-2 cutting inserts coated with TiN were subjected to ion implantation with both silicon (dose 2x1017Si+/cm2) and silicon with nitrogen ions (dose (1+1)x1017(Si+ + N+)/cm2) on the subsurface layer of the rake face. Microhardness was examined before and after ion implantation. The composition and structural properties of the subsurface layer were examined by Glow Discharge Optical Emission Spectroscopy (GD-OES). The turning tests of 40H construction steel with the use of the cutting inserts implanted and non-implanted were performed. During the tests the two components of the net cutting force (the main cutting force Fc and feed force Ff) as well as the wear parameters VB on the major flankalong with the surface roughness (Ra) were measured. The implanted inserts exhibited higher durability compared to non-implanted ones.

Andrzej Waindok, Bronisław Tomczuk
Reluctance Network Model of a Permanent Magnet Tubular Motor

The reluctance network model of a permanent magnet tubular motor (PMTM) has been presented in the paper. The reluctance values of the magnetic circuit have been calculated with using analytical expressions. The air gap reluctance has been determined with using both analytical expressions and the finite element method (FEM). Using the calculation model, the flux values coupled with the windings have been obtained and used in the calculations of force value. The calculated results have been compared with numerical and measured ones.

Marek Wojciechowski
Minimal Kinematic Boundary Conditions for Computational Homogenization of the Permeability Coefficient

In the paper, computational homogenization approach is used for recognizing the macroscopic permeability from the microscopic representative volume element (RVE). Flow of water, at both macro and micro level, is assumed to be ruled by Darcy law. A special averaging constraint is used for numerical flow analysis in RVE, which allows to apply macroscopic pressure gradient without the necessity to use directly Dirichlet or Neumann boundary conditions. This approach allows arbitrarily shaped representative volumes and eliminates undesirable boundary effects. Generated effective permeability takes into account the structuring effects, what is an advantage over other homogenization methods, like self-consistent one.

Dmytro Fedorynenko, Serhii Sapon, Sergiy Boyko, Anastasiia Urlina
Increasing of Energy Efficiency of Spindles with Fluid Bearings

Promising ways of energy efficiency gain of spindles with fluid flow bearings are offered. New design of journal hybrid flow bearing which contains spherical bearing pockets and adjustable valves with relay control system is offered to improve energy efficiency of spindle units of machine tools. To reduce power losses of fluid bearings at high speed special lubrication based on water with integrated system of corrosion protection is offered. Results of theoretical research of energy consumption of grinding machine tool with a new design of spindle hybrid bearings are presented. Power losses of the spindle unit with both new design and base design of journal bearings are assessed. Effectiveness of new design of spindle hybrid bearings at high operating speeds is shown.

Marek Płaczek, Andrzej Wróbel, Andrzej Buchacz
Structural Tests of Freight Wagons on the Basis of Signals Generated By Piezoelectric Macro Fiber Composites

Paper presents a report of a research work that concerns possibilities of freight wagons modernization using new composite materials. The main aim of presented work was to verify the possibility of inference from the dynamic response of the wagon about the changes in its technical condition. During the presented works tests on real objects were carried out using Macro Fiber Composite (MFC) piezoelectric transducers glued to the freight wagon's frame. The dynamical response of the wagon was measured while the object was driving. On the next stage the measured signal was generated on a laboratory stand using electrodynamic modal shaker and vibrations of the laboratory model were measured. Measured signals were juxtaposed on charts and analysed. The aim of this work was to verify if it is possible to detect the change in the system using measurements of vibrations that are being generated during exploitation of the freight wagon.

Olena Mikulich, Vasyl' Shvabjuk, Heorgij Sulym
Dynamic Stress Concentration at the Boundary of an Incision at the Plate Under the Action of Weak Shock Waves

This paper proposes the novel technique for analysis of dynamic stress state of multi-connected infinite plates under the action of weak shock waves. For solution of the problem it uses the integral and discrete Fourier transforms. Calculation of transformed dynamic stresses at the incisions of plates is held using the boundary-integral equation method and the theory of complex variable functions. The numerical implementation of the developed algorithm is based on the method of mechanical quadratures and collocation technique. For calculation of originals of the dynamic stresses it uses modified discrete Fourier transform. The algorithm is effective in the analysis of the dynamic stress state of defective plates.

Andrzej Jurkiewicz, Janusz Kowal, Kamil Zając
Sky-Hook Control and Kalman Filtering in Nonlinear Model of Tracked Vehicle Suspension System

The essence of the undertaken topic is application of the continuous sky-hook control strategy and the Extended Kalman Filter as the state observer in the 2S1 tracked vehicle suspension system. The half-car model of this suspension system consists of seven logarithmic spiral springs and two magnetorheological dampers which has been described by the Bingham model. The applied continuous sky-hook control strategy considers nonlinear stiffness characteristic of the logarithmic spiral springs. The control is determined on estimates generated by the Extended Kalman Filter. Improve of ride comfort is verified by comparing simulation results, under the same driving conditions, of controlled and passive vehicle suspension systems.

Janusz Gołdasz, Bogdan Sapiński
Magnetostatic Analysis of a Pinch Mode Magnetorheological Valve

The study deals with the pinch mode of magnetorheological (MR) fluids' operation and its application in MR valves. By applying the principle in MR valves a highly non-uniform magnetic field can be generated in flow channels in such a way to solidify the portion of the material that is the nearest to the flow channel's walls. This is in contrary to well-known MR flow mode valves. The authors investigate a basic pinch mode valve in several fundamental configurations, and then examine their magnetic circuits through magnetostatic finite-element (FE) analysis. Flux density contour maps are revealed and basic performance figures calculated and analysed. The FE analysis results yield confidence in that the performance of MR pinch mode devices can be effectively controlled through electromagnetic means.

Rafał Mech, Jerzy Kaleta
Influence of Terfenol-D Powder Volume Fraction in Epoxy Matirx Composites on their Magnetomechanical Properies

In this paper the investigations of magnetostriction as well as DC magnetic properties for composites doped with Terfenol-D particles are presented. All investigations were performed for the materials with 35%, 46% and 70% volume fraction of the Terfenol-D particles surrounded by epoxy matrix. Moreover, the bulk Terfenol-D alloy was tested. The obtained results show that the magnetization of the composite materials ncreases with increasing the volume fraction of Terfenol-D particles. Similar dependence as for magnetization was observed for the magnetostriction measurements. Although the magnetostriction of composite material is smaller than for solid Terfenol-D it is still tens of times bigger than in case of traditional magnetostrictive materials. Obtained results gives opportunity to use these materials for variety applications such as actuators and sensors.

Mariusz Żokowski, Paweł Majewski, Jarosław Spychała
Detection Damage in Bearing System of Jet Engine Using the Vibroacoustic Method

The article discusses typical, operational systems for monitoring vibrations of jet engines, which constitute the propulsion of combat aircraft of the Armed Forces of the Republic of Poland. After that, the paper presents the stage of installing vibration measuring sensors in the direct area of one of the jet engine bearings, which is a support system for its rotor. The article discusses results of carried out analyses of data gathered during tests of the engine in the conditions a jet engine test bed. Results of detecting damages to the bearing, using sensors built in the direct area will be presented.

Martin Sturm, Lubomir Pesik
Determination of a Vibrating Bowl Feeder Dynamic Model and Mechanical Parameters

Vibrating conveyors also named bowl feeders are a common equipment for conveying goods into production systems. These systems are used for the supplying of a certain number of goods to an individual designed interface and simultaneously arranging a correct orientation of the goods conveyed by the same time. This type of conveyor is used in various industries, such as for example automotive industry, electronic industry and medical industry. The target of this article is to determine a dynamic model and mechanical parameters by means of testing, and a numerical simulation of a ready-to-operate conveyor under standard working conditions.